# High Performance Integrated Beam-Steering Techniques for Millimeter-Wave Systems

by

Ahmed Shehata Mohamed Abdellatif

A thesis
presented to the University of Waterloo
in fulfillment of the
thesis requirement for the degree of
Doctor of Philosophy
in
Electrical and Computer Engineering

Waterloo, Ontario, Canada, 2015

I hereby declare that I am the sole author of this thesis. This is a true copy of the thesis, including any required final revisions, as accepted by my examiners.

I understand that my thesis may be made electronically available to the public.

## Abstract

Recently, the research and development of low cost and highly efficient millimeter-wave (mmWave) systems with beam-steering capabilities have significantly advanced to address the ever-increasing demand for future wireless ultra-broadband applications. These applications include, but are not limited to, automotive anti-collision surveillance radar, smart navigation systems, improved wireless tracking, satellite communication, imaging, 5G wireless communication, and 60GHz multi-gigabit wireless personal and local area network (WPAN/WLAN). In general, beam-steering capability significantly relaxes the overall system power budget and minimizes the interference. In communication applications, it enhances the link robustness through multi-path mitigation and increases the channel and the aggregated channel throughput by exploiting the spatial dimension. In imaging/radar systems, beam-steering is essential for achieving the required resolution (angle-of-arrival). In this work, I have proven many beam-steering advantages in this work through the development of a ray-tracing based wireless channel model, which has been used to extract the antenna system requirements and to quantitatively illustrate the usefulness of the presented beam-steerable systems.

Despite the advantages it provides, the realization of this electronic beam-steerable mmWave antenna system is quite challenging. In general, the mmWave components' design, integration, fabrication and testing processes are far more complex than their lower frequency counterparts. This can be attributed to the significant losses and parasitics experienced at mmWave frequencies, as well as the lack of reliable design models. Systems with fully integrated (on-chip) antennas and passives have been widely studied and presented at mmWave range; however, the performance (low antenna gain, high phase noise, etc), the cost (die size is huge), and thermal problems are still major issues for these systems. Hybrid integration tackles these problems by combining a compact and low power consumption die (or multiple dies) with high performance off-chip passives (antenna, feed network, passive phase shifters, resonators, etc); however, this integration is costly. In addition, there is a challenge associated with the implementation of high performance components at mmWave range. This is mainly due to the use of advanced/non-standard types of fabrication technologies and complex integration/packaging techniques.

Investigation, optimization, development of a highly efficient and yet very low cost mmWave beam-steering solution calls for a multi-disciplinary approach which involves EM theory, optimization techniques, microwave circuits, wireless communications, Silicon micro-fabrication, layout design, parasitics modeling/extraction and MEMS technology.

The proposed study introduces a high performance beam-steering mmWave antenna system along with its integration with the active components with special consideration to the fabrication cost. The new high resistivity Silicon (HRS) dielectric waveguide (DWG) based platform, which has recently been developed at CIARS (Centre for Intelligent Antenna and Radio Systems), is extended and used for wireless mmWave systems with beam-steering antennas. Electronic beam-steering can be implemented through beam-switching configurations (simple, fast but coarse) or phase array configurations (complex but high performance for large arrays).

A novel low cost, highly efficient and compact switched-beam antenna is proposed for the automotive radar application. The design optimization along with the fabrication and measurement details have been discussed. For phased array applications, various HRS DWG-based antenna designs have been proposed and discussed in this study. Among them is the novel pixelated antenna which represents a new systematic procedure for designing a compact and low cost dielectric antenna for mmWave/sub-THz applications. I have developed a method using Genetic Algorithm to optimize the shape of the antenna in a compact space for any given specifications.

The other important component is the phase shifter. Low-cost, compact and easily integrated phase shifters with low insertion loss and low power consumption are highly desirable for a wide range of applications. In addition, minimal insertion loss variations for the full range of phase shift over a wide frequency band is a critical requirement. I have carefully studied the effects of phase shifters non-idealities, taking into consideration the phased array system level requirements and presented two novel HRS DWG-based phase shifters. Among the proposed phase shifters is a structure that changes the phase of the propagating mode by varying the propagation constant using a high dielectric constant (40-170) slab of Barium Lanthanide Tetratitanates. This leads to a compact phase shifter design. The additional advantage of this phase shifter is that it focuses the fields in a lossless air gap (new low loss guiding structure). Different types of the proposed phase shifter have been developed and successfully tested including electrically controlled ones.

Finally, I present new techniques for low cost and efficient integration for the proposed high quality mmWave passives with active components.

**Acknowledgements**

I would like to express my deepest appreciation and thanks to my supervisor Prof. Safieddin Safavi-Naeini for his constant support and valuable advices throughout my graduate studies at Waterloo. I would also like to thank all my committee members, Prof. Amir Mortazawi, Prof. Rafaat Mansour, Prof. Simarjeet Saini, and Prof. Mostafa Yavuz.

The experience I have gained in the CIARS centre at the University of Waterloo is priceless. I would like to thank all CIARS members and especially Dr. Suren Gigoyan for his valuable advices and guidance. Also I want to thank A. Nashed, M. Mohajer, A. Taeb, G. Rafi, A. Zandieh, N. Ranjkesh and Chris Schroeder.

I would like to express my gratitude to Prof. S. Boumaiza and to my friends A. Abdel-Aziz, A. Abdelbary and A. Bayoumy for their continuous advices and fruitful discussions. I would like to thank S. Klaus and M. Elkhouly from IHP-Microelectronics. I would also like to thank Nathan Nelson - Fitzpatrick from the qncfab at the University of Waterloo as well as Stephanie Bozic from the nanofab at the University of Alberta for their valuable advices in clean-room.

I would like also to thank all my Peraso colleagues for their continuous support, especially the Analog group and in particular M. Tazlauanu, A. El-Gabaly, A. Tomkins, M. Fakharzadeh, N. Smith, and E. Juntunen.

Last but not least, I would like to thank my parents and my wife. Without your support over the past five years, this could not be possible.

## Dedication

This is dedicated to my wife Shireen for her continuous support and encouragement throughout my PhD and to my beautiful daughter Sarah.

# Table of Contents

**List of Tables** **xv**

**List of Figures** **xvii**

**1 Introduction** **1**

1.1 Thesis Objectives . . . . . 2

1.2 Motivation: Why beam-steering is needed for mmWave applications? . . . 3

1.3 How mmWave beam-steering has been implemented? . . . . . 4

1.3.1 Beam-Switching . . . . . 4

1.3.2 Phased Arrays . . . . . 6

1.4 State of the Art for mmWave Planar Antenna Technologies . . . . . 7

1.4.1 LTCC Technology . . . . . 11

1.4.2 Organic Multi-Layer Substrate Technology . . . . . 11

1.4.3 Thin Film Technology . . . . . 12

1.5 Current Options for mmWave Antenna Feed Circuits . . . . . 15

1.6 Existing mmWave Phase Shifters . . . . . 18

1.7 Thesis Organization . . . . . 18

**2 Beam-steering System Requirements** **19**

2.1 Example 1: 60GHz Wireless Communication System Link Robustness . . . 19

2.1.1 Model . . . . . 20

2.1.2 Simulation Results . . . . . 24
2.1.3 Example 1: Summary . . . . . 29
2.2 Example 2: Automotive Radar (77GHz/79GHz) . . . . . 31
2.2.1 Antenna Requirements . . . . . 31
2.2.2 Example 2: Summary . . . . . 33

**3 Novel HRS DWG-based Antennas 35**
3.1 Dielectric Waveguide . . . . . 35
3.1.1 Dielectric Slab Waveguide . . . . . 40
3.1.2 Rectangular Dielectric Waveguide . . . . . 41
3.2 Novel DWG-based Multi-Beam Grating Antenna . . . . . 45
3.2.1 First Configuration: Twelve Beams Annular Grating Antenna . . . 45
3.2.2 Second Configuration: Five Beams Annular Grating Antenna . . . . 49
3.2.3 Fabrication . . . . . 51
3.2.4 Measurement Results . . . . . 54
3.3 Novel DWG-based Pixelated Antenna . . . . . 58
3.3.1 Example 1: Pixelated antenna optimized for maximum gain . . . . 60
3.3.2 Example 2: Pixelated antenna with multiple optimization objectives 65
3.3.3 Comparison with Tapered Rod (Reference Antenna) . . . . . 69
3.4 New DWG-based Travelling Wave Antenna . . . . . 72

**4 Novel HRS DWG-based Phase Shifters 77**
4.1 Phase Shifter Loss Variation Requirement . . . . . 78
4.2 Wiggling Dielectric Waveguide Delay Line/Phase Shifter (WDWG) . . . . 80
4.2.1 Simplified Model . . . . . 82
4.2.2 Gap size . . . . . 84
4.2.3 Example 1: Seven blocks 77GHz phase shifter . . . . . 84
4.2.4 Phase Shifter Implementation . . . . . 90

4.3 Novel BLT Phase Shifter . . . . . 94
4.3.1 Design . . . . . 95
4.3.2 Fabrication Process . . . . . 98
4.3.3 Measurements Results . . . . . 100
4.3.4 Electrically Controlled Version . . . . . 109

**5 HRS DWG Integration with Active Components 115**
5.1 Flip-chip on DWG Packaging Approach . . . . . 115
5.2 WG to DWG/DIG Transition (Step 1) . . . . . 117
5.2.1 Test Structure: Back-to-Back WG to DIG to WG transition . . . . 118
5.3 CPW to DIG Transition (Step 2) . . . . . 122
5.3.1 Test Structure: Back-to-Back CPW to DIG to CPW transition . . . 123
5.3.2 Test Structure: CPW-fed Dielectric Side Grating Antenna . . . . . 127
5.4 WG to DIG to CPW Transitions (Steps 1 and 2) . . . . . 130
5.4.1 Test Structure: Back-to-Back transition . . . . . 130
5.5 WG to DIG to CPW to Flip-chip Transitions (Steps 1, 2 and 3) . . . . . 132
5.5.1 Test Structure: DIG integrated LNA flip-chip with WR10 interface 135

**6 Conclusion and Future Plan 139**
6.1 Summary of Results . . . . . 139
6.2 Future Work . . . . . 141
6.2.1 MEMS-based BLT phase shifter . . . . . 141
6.2.2 MEMS-based switched-beam antenna . . . . . 141
6.2.3 DIG integrated flip-chip . . . . . 142

**References 143**

# List of Tables


2.1 Measured Reflection Coefficient for different materials at 60 GHz. V and H refer to the horn antenna vertical and horizontal polarizations. . . . . 23

2.2 Coverage in a 5×5 ($m^2$) room. . . . . 30

3.1 Different designs at 60 GHz. . . . . 61

3.2 Cost Function at 77 GHz. . . . . 65

4.1 Optimized Configurations. . . . . 88

4.2 Configurations simulated performance normalized to Config. 1 at 77GHz. . 89

4.3 Summary of Measurements at $100GHz$. . . . . 104

4.4 Performance Comparison of Available Phase Shifters. . . . . 113

# List of Figures


1.1 Block diagram for a wireless transceiver. . . . . 3
1.2 Link distance calculation showing the benefit of arrays at 60 GHz [17]. . . 4
1.3 Five beams Rotman lens based compact design at 24GHz [53]. . . . . 5
1.4 Five beams pattern from [53]. . . . . 5
1.5 Picture of 60 GHz Rotman Lens [74]. . . . . 6
1.6 Three beams pattern [74]. . . . . 6
1.7 A two-element mmWave phased array system with passive beam-forming [55]. 7
1.8 Example for on-chip antenna at 35 GHz (a) The dimensions of the H-slot aperture. (b) Die micrograph of the H-shape slot with DR and CPW probe [64]. . . . . 8
1.9 Example for on-chip antenna at 77 GHz [34]. . . . . 8
1.10 Example for on-chip antenna array at 110 GHz [71]. . . . . 9
1.11 3D model of an on-chip THz antenna (710GHz) [10]. . . . . 9
1.12 Top view of the proposed THz antenna [10]. . . . . 10
1.13 Cross-section A-A indicating different layers thicknesses [10]. . . . . 10
1.14 Simulated $S_{11}$ in dB [10]. . . . . 10
1.15 LTCC AiP example 1: Stack-up cross section [46]. . . . . 11
1.16 LTCC AiP example 1: Picture [46]. . . . . 11
1.17 LTCC AiP example 2: Picture [19]. . . . . 12
1.18 Organic AiP example 1: Stack-up cross section [47]. . . . . 12
1.19 Organic AiP example 1: Picture [47]. . . . . 13

1.20 Thin Film AiP example 1: Picture, HFSS model and measurement setup [80]. 13
1.21 Thin Film AiP example 2: Exploded view of the antenna [43]. . . . . 14
1.22 Thin Film AiP example 2: 3D view of the proposed AiP [43]. . . . . 14
1.23 Thin Film AiP example 3: Stack-up [16]. . . . . 14
1.24 Thin Film AiP example 3: Picture and measured/simulated results in free space (FS) and the IPD/PCB package [16]. . . . . 15
1.25 Insulated image guide [66]. . . . . 16
1.26 Exploded view of SIIG [66]. . . . . 16
1.27 Measured insertion and return loss for the short and long SIIG sections fabricated of HR silicon. Losses arising from the two transitions are included. Core dimensions: 510 $\mu m\times$ 380 $\mu m$ ($w \times h$), insulation film thickness: 75 $\mu m$ [66]. . . . . 17
1.28 3D view of a non-radiating dielectric waveguide [88]. . . . . 17
1.29 Cross section of a non-radiating dielectric waveguide [88]. . . . . 17
1.30 (Left) Schematical drawing of 360° seven-stage phase shifter and its (right) phase resolution[73]. . . . . 18

2.1 NLOS scenario. . . . . 20
2.2 LOS scenario. . . . . 20
2.3 Diagram shows (a) normal polarized, and (b) parallel polarized plane waves incident at oblique angles [13]. . . . . 22
2.4 Calculated Reflection Coefficient vs the angle of incidence for different materials at 60GHz. . . . . 23
2.5 Picture of the setup used for measuring the Reflection Coefficient. . . . . 24
2.6 Block diagram of the setup used for measuring the Reflection Coefficient. . 24
2.7 Simplified ray-tracing model used for LOS scenario. . . . . 25
2.8 Flat fading for a single element/antenna radio. . . . . 25
2.9 The effect of changing the height (L). . . . . 26
2.10 AOA for the interferer signal versus distance. . . . . 27
2.11 Beam-width for N-element arrays versus the steering Angle. . . . . 27

2.12 SNR versus distance for an array of four elements. This has been simulated at $L = 1m$. . . . . 28
2.13 SNR versus distance for different antenna arrays simulated at $R = -10dB$ and $L = 1m$. . . . . 28
2.14 Simplified ray-tracing model used for NLOS scenario. . . . . 29
2.15 SNR (NLOS case) versus distance for different antenna arrays simulated at $R = -10dB$ and $L = 1m$. . . . . 29
2.16 SNR (NLOS case) versus distance for different antenna arrays simulated at $R = -7dB$ and $L = 1m$. . . . . 30
2.17 Conventional 4×4 phased array patch antenna [1]. . . . . 31
2.18 Proposed 4×4 phased array patch antenna [1]. . . . . 31
2.19 The range is the maximum distance at which the car/obstacle can be detected by the radar. . . . . 33
2.20 The Field-Of-View defines the maximum range of angles that can be detected by the radar. . . . . 33
2.21 Array factor for eight elements antenna array with a 0.65 $\lambda$ spacing showing the center beam and the $\pm 40^o$ beams. . . . . 34
2.22 A schematic for the proposed radar antenna. . . . . 34

3.1 Skin depth variations with frequency for different conductors. . . . . 36
3.2 surface roughness effect at mmWave. . . . . 36
3.3 Measured surface roughness of CPW metallization on HRS substrate. . . . 38
3.4 Measured S-parameters for 1mm CPW line on HRS substrate. . . . . 38
3.5 Picture of the fabricated test structure. . . . . 39
3.6 Grounded dielectric slab [67]. . . . . 40
3.7 Graphical method [67]. . . . . 41
3.8 2D model in HFSS. . . . . 41
3.9 HFSS eigen solution. . . . . 41
3.10 Gaphical method. . . . . 41

3.11 The geometry of a rectangular dielectric waveguide in Marcatili's method and the distribution of $H_x$ for the $E^y_{12}$mode[58]. . . . . 42
3.12 Silicon image waveguide . . . . . 42
3.13 Measurement Setup. . . . . 43
3.14 Measured $S_{21}$ and $S_{11}$ magnitudes variations with frequency. . . . . 44
3.15 Proposed twelve-beams dielectric grating antenna . . . . . 46
3.16 Effect of $\epsilon_r$ on the beam direction. . . . . 47
3.17 Changing the grating period (d) slightly changes the gain and has no effect on beam angle . . . . . 48
3.18 Changing grating thickness for a fixed period of 2.4mm . . . . . 49
3.19 Shows the radiation pattern for $\phi = 0°$ excitation . . . . . 50
3.20 Polar plot for the gain (dB) for different ports vs $\phi(\theta_B = 60°)$ . . . . . 51
3.21 shows the uniform Multi-Beam Dielectric Grating Antenna (MB DGA): configuration 2. . . . . 52
3.22 Polar plot for the five-beams gain (dB) for different ports vs $\phi(\theta_B = 60°)$ . 53
3.23 Process flow: Each step is illustrated in the process list . . . . . 54
3.24 The 3D model developed by Coventor tool. . . . . 54
3.25 Fabricated MB DGA. . . . . 55
3.26 $S_{11}$ measurement setup. . . . . 55
3.27 Radiation pattern measurement setup. . . . . 56
3.28 Measured and simulated radiation (gain) patterns. . . . . 57
3.29 Measured and simulated $|S_{11}|$. . . . . 57
3.30 The general schematic of a pixelated antenna. . . . . 59
3.31 Flow chart of the proposed antenna design method. . . . . 62
3.32 Convergence plot for Example 1. . . . . 63
3.33 3D model of the optimal design of Example 1. . . . . 63
3.34 E field distribution of Example 1. . . . . 64
3.35 Gain pattern of Example 1. . . . . 64

3.36 3D model of the optimized antenna. . . . . 66
3.37 Fabricated pixelated antenna sample. . . . . 66
3.38 $S_{11}$ in dB (simulated and measured). . . . . 67
3.39 E-plane normalized gain (simulated and measured) at 77 GHz. . . . . 67
3.40 Simulated pattern (solid line) after including non-idealities in test fixture. The dotted line shows measured results. . . . . 68
3.41 Picture of the tapered antenna mounted on the test fixture used for measurements. . . . . 69
3.42 Picture of the tapered antenna mounted on the test fixture used for measurements. . . . . 70
3.43 Radiation pattern at 77GHz for the reference antenna. . . . . 70
3.44 Gain comparison between the three examples. . . . . 71
3.45 Picture of the dielectric side grating antenna [89]. . . . . 73
3.46 Maximum gain and reflection coefficient of rectangular profile over the operating frequency range [89]. . . . . 73
3.47 3D model of the proposed CPW-fed side grating antenna. . . . . 74
3.48 The gain frequency response of the proposed antenna. . . . . 75
3.49 Gain pattern of the proposed antenna at 62.5GHz. . . . . 75
3.50 E-plane gain pattern for different frequencies. . . . . 76
3.51 A fabricated sample of the proposed CPW-fed side grating antenna. . . . . 76

4.1 The array factor for an eight element non-uniform (linear tapering is used) excited linear antenna array for different phase shifter performances. . . . . 78
4.2 The antenna array model used for calculating the array factor. . . . . 79
4.3 The effect of phase shifter insertion loss variation on the side lobe level of eight elements array. . . . . 80
4.4 A schematic of an eight element transmitter phased array. . . . . 81
4.5 Diagram of the proposed phase shifter . . . . . 81
4.6 Shows three free blocks version of the phase shifter. . . . . 82

4.7 Shows field modulation while changing the sliding parts. . . . . 82
4.8 Shows the phase shift for both full field simulations and model. . . . . 83
4.9 Shows the macro-modeling structure. . . . . 84
4.10 Shows the magnitude of S parameters for both full field simulation and cascaded macro-models. . . . . 85
4.11 Transitional gap. . . . . 86
4.12 Shows different displacements assignment. . . . . 86
4.13 Shows the insertion loss vs different phase shifts. . . . . 87
4.14 $S_{21}$ magnitude variations with frequency for 150° phase shift setup. . . . . 88
4.15 $S_{21}$ phase frequency dependence for 150° phase shift setup. . . . . 89
4.16 E-field distribution for the designed test structures. . . . . 90
4.17 Single print through wafer silicon etching process for the wiggling dielectric waveguide fabrication. . . . . 91
4.18 a) Three fabricated samples, (b) Measurement setup for the sample with the Configuration 3. . . . . 91
4.19 $S_{21}$ phase variations with frequency for the three test structures. . . . . 92
4.20 $S_{21}$ magnitude variations with frequency for the three test structures. . . . 92
4.21 WDWG based Switched Line Phase Shifter. . . . . 93
4.22 3D model of a test structure for the proposed phase shifter. . . . . 94
4.23 3D model of a test structure for the new BLT-loaded HRS DIG phase shifter. 95
4.24 Cross section in the DIG shows the E field magnitude distribution at 100GHz. 96
4.25 HFSS model of the whole test structure. . . . . 97
4.26 E field distribution at 100GHz. . . . . 98
4.27 Simulated $S_{21}$ and $S_{11}$ magnitudes versus frequency. . . . . 99
4.28 E Field distribution at 100GHz longitudinal cut at air gap=5$\mu m$. . . . . 99
4.29 E Field distribution at 100GHz longitudinal cut at air gap=25$\mu m$. . . . . 100
4.30 Phase shift variation versus air gap at 100GHz for the studied samples. . . 100
4.31 Optical lithography Fabrication Process for the proposed structure. . . . . 101

4.32 Fabricated sample: Picture of the waveguide. . . . . 101
4.33 Fabricated sample: SEM scan of the waveguide. . . . . 101
4.34 Silicon surface roughness profile. . . . . 102
4.35 BLT slab surface roughness profile after polishing. . . . . 102
4.36 The experimental setup. . . . . 103
4.37 Schematic of the micro-positioner setup. . . . . 104
4.38 Measured and simulated magnitudes of $S_{11}$ and $S_{21}$ versus frequency for the DIG in the absence of the BLT slab. . . . . 105
4.39 Measured $S_{21}$ and $S_{11}$ magnitude variation versus frequency for different air gaps. . . . . 105
4.40 Measured phase variation versus frequency for different air gaps. . . . . 106
4.41 Measured $S_{21}$ and $S_{11}$ magnitude variation versus frequency for different air gaps. . . . . 106
4.42 Measured phase variation versus frequency for different air gaps. . . . . 107
4.43 Measured $S_{21}$ and $S_{11}$ magnitude variation versus frequency for different air gaps. . . . . 107
4.44 Measured phase variation versus frequency for different air gaps. . . . . 108
4.45 Phase shift variation simulations (solid line) and measurements (circles) versus air gap at 100GHz for the studied samples. . . . . 108
4.46 3D model for the electrically controlled version of the proposed phase shifter. 109
4.47 Measurement setup. . . . . 110
4.48 Piezoelectric transducer. . . . . 110
4.49 Piezoelectric attachment to the BLT slab. . . . . 110
4.50 Modified test fixture. . . . . 111
4.51 Measured $\|S_{11}\|$ and $\|S_{21}\|$ of the DIG in the absence of the dielectric slab. 111
4.52 $\|S_{11}\|$ and $\|S_{21}\|$ of the test structure for two different states of the piezoelectric transducer. The measurement results are shown in dotted lines while the simulation results are shown in solid ones. . . . . 112

4.53 Measured phase shift of the test structure for two different states of the piezoelectric transducer. The measurement results are shown in dotted lines while the simulation results are shown in solid ones. . . . . 113

5.1 3D model of the proposed flip-chip integration structure. . . . . 116

5.2 3D model for the proposed WG to DIG tapered transition with different profiles; (a)Profile 1: y=$\alpha_1$x, (b)Profile 2: x=$\alpha_2 y^2$ and (c)Profile 3: y=$\alpha_3 x^2$. 117

5.3 Transition insertion loss vs tapering length $L_t$ for different tapering profiles. 118

5.4 V-band back-to-back WG to DIG test structure with linear 6mm tapered transition. . . . . 119

5.5 Simulated S-parameters for a V-band back-to-back WG to DIG test structure with linear 6mm tapered transition. . . . . 120

5.6 Fabricated W-band back-to-back WG to DIG test structure. . . . . 120

5.7 Simulated S-parameters for a W-band back-to-back WG to DIG test structure with linear 6mm tapered transition. . . . . 121

5.8 3D model for the proposed CPW to DIG tapered transition with different profiles; (a)Profile 1: Linear, and (b)Profile 2: Quadratic. . . . . 122

5.9 3D model for the proposed back-to-back CPW to DIG test structure. . . . 123

5.10 Simulated S-parameters for the back-to-back test structure operating at the V-band. . . . . 124

5.11 Simulated and measured S-parameters for the back-to-back test structure optating at the W-band. . . . . 125

5.12 Picture of the fabricated back-to-back test structure optating at the W-band.125

5.13 Two-mask fabrication process. . . . . 126

5.14 On-wafer W-band measurement setup used for testing the back-to-back CPW to DIG transition. . . . . 126

5.15 3D model of the proposed CPW-fed side grating antenna. . . . . 127

5.16 The gain frequency response of the proposed antenna. . . . . 128

5.17 A picture of the proposed CPW-fed side grating antenna. . . . . 128

5.18 Simulated and measured input reflection coefficient of the proposed CPW-fed side grating DIG antenna. . . . . 129

5.19 Picture of the proposed test structure. . . . . 131
5.20 Measured and Simulated S-parameters for the proposed test structure. . . 131
5.21 Diagram showing different pads assignments. . . . . 132
5.22 3D model of the flip-chip die with solder bumps. . . . . 133
5.23 3D model of the flip-chip die with solder bumps. . . . . 133
5.24 CPW to flip-chip transition. . . . . 134
5.25 HFSS model for the DIG integrated flip-chip. . . . . 134
5.26 Dimensions of the proposed test structure. . . . . 135
5.27 Simulated E-field for the DIG integrated flip-chip distribution at 77GHz. . 136
5.28 Simulated S-parameters for the DIG integrated flip-chip. . . . . 136
5.29 Picture of the proposed flip-chip integration structure. . . . . 137

# Chapter 1

# Introduction

Emerging wireless millimeter-wave (mmWave) applications such as 5G wireless communications, automotive radar, 60GHz WiFi, satellite communications and mmWave imaging brought huge interest in the research of mmWave systems. There are many attractive features in mmWave systems including short wavelengths which make the mmWave radio compact. At mmWave range, antennas can be more readily integrated on-chip or in-package. Also, at mmWave, beam-forming, beam-steering and spatial-power combining are feasible in a low cost and a compact form. In addition, wireless mmWave signals experiences high propagation attenuation making it ideal for short links and secure data transfer. The quasi-optical type of mmWave propagation enables spatial diversity which can lead to hundreds of Gbps aggregated bandwidth to the already huge free spectrum at mmWave.

The computer hardware, smart phones and wireless technology industry are pushing to commercialize mmWave enabled wireless systems, and a significant sector of academic research is working towards the same purpose. In order to compete in the market, the mmWave systems need to have a robust performance with a relatively low cost. For example, in a file transfer application, the entire system (including the base band, the radio, the antenna and packaging) should cost no more than other existing solutions currently found in handheld devices ($\sim$ 5\$). It is a challenging task as the mmWave components' design, integration, fabrication and testing processes are more complex than those in the lower frequency systems. This is mainly attributed to the higher losses, complex propagation mechanisms (especially in non line of sight situations), lack of accurate data on propagation characteristics of many common materials at this frequency range, complexity of the measurements and the high cost associated with packaging.

The future of wireless mmWave is determined by efficient and low cost beam-steering. Beam-steering helps not only in the multi-path effects mitigation, but also in enhancing the channel throughput by exploiting the spatial dimension of a wireless link. Similarly, the introduction of beam-steering in the system relaxes the overall power budget which is critical for the power hungry mmWave systems. The motivation for this work is to propose a high performance but low cost beam-steering solution for mmWave applications.

## 1.1 Thesis Objectives

The first objective of this research is to analyze different high level requirements for mmWave beam-steering by providing a simple approach to extract antenna and beam-steering related specifications from the system level specs. This is then applied to different mmWave applications. A simple ray-tracing tool has also been developed to model the mmWave wireless channel for this purpose.

The second objective is to demonstrate the usage of High Resistivity Silicon (HRS) dielectric waveguide (DWG) technology in high performance passive mmWave beam-steering solutions. For this purpose, different aspects of the proposed technology are presented, highlighting the ones that make this technology a perfect candidate, compared to the other existing technologies, for low cost and high performance mmWave applications. Also, this thesis proposes novel HRS DWG-based components for passive beam-steering. These components include novel switched-beam antennas, phased array antenna elements and phase shifters.

The final objective is to develop an efficient but low cost integration solution to interconnect the proposed beam-steering antenna systems with the other active components (in order to construct a complete wireless system). This implies the development of new wide-band, low loss and low cost mmWave transitions.

## 1.2 Motivation: Why beam-steering is needed for mmWave applications?

In any wireless transceiver (as shown in Fig. 1.1), the link signal strength/quality is largely determined by the SNR level at the receiver ADC. Given that the bandwidth is already quite wide (thermal noise is high) and the receiver NF at mmWave is relatively high (ranges from 4dB to 8dB for good designs in V and W bands), the remaining controllable variables are the transmitter output power and the antenna gain. The transmitter output power is usually limited by many factors including non-linearity issues, power consumption, thermal considerations and standard regulations. Therefore, the antenna gain is the most controllable variable in the SNR equation. In [17], a quick link distance calculation is presented at 60GHz (see Fig. 1.2) that shows the benefit of using antenna arrays. This comparison shows that for a receiver with -61dBm sensitivity, we can extend the range from 0.6m to 37m by replacing the single element radio with a 16-element phased array on TX and RX sides.

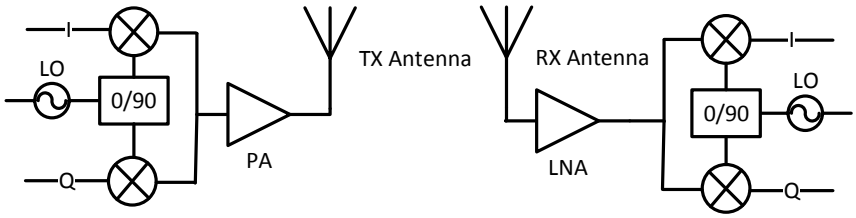


Figure 1.1: Block diagram for a wireless transceiver.

The antenna gain is simply a measure of the directivity (and the efficiency) of the antenna. The narrower the beam that the antenna can achieve, the higher the antenna gain. This can be observed in the approximate directivity formula shown below [23],

$$Directivity \simeq 10log(\frac{32400}{\Theta_{H3dB}\Theta_{V3dB}}) \tag{1.1}$$

Where $\Theta_{H3dB}$ is the antenna Half Power Beam Width (HPBW) in the azimuth plane and $\Theta_{V3dB}$ is the antenna HPBW in the elevation plane in degrees. So by making the antenna more directive the required SNR can be achieved without increasing the output

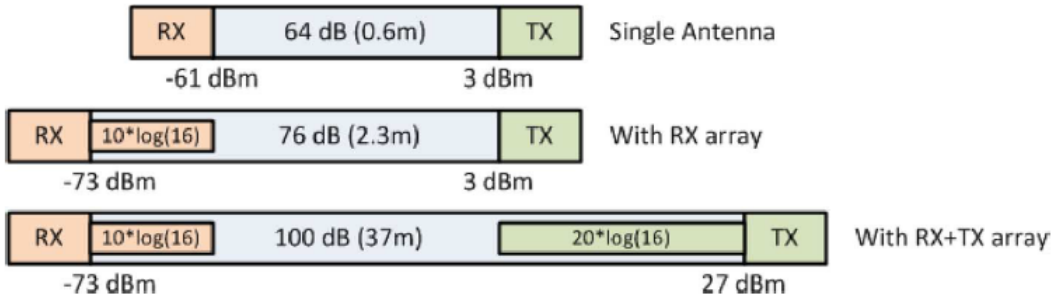


Figure 1.2: Link distance calculation showing the benefit of arrays at 60 GHz [17].

power. The only price you have to pay is narrowing the beam which can be considered as an advantage in terms of data security or in multi-path environment but it requires beam-steering capability. In narrow beam/high gain antennas, beam-steering is highly desired to be able to point the power in the right direction from the transmitter to the receiver since both are generally mobile. For example, mobile mmWave transciever can be a handheld device, or a land mobile satellite communication system. Even fixed backhaul links require beam-steering capability for adjusting the alignment from time to time due to the winds.

## 1.3 How mmWave beam-steering has been implemented?

Beam-steering is focusing the electromagnetic energy in a specific direction; this leads to an improvement in the value of the signal to interference and noise ratio. As early discussed, at mmWave, significant losses and strong multi-path effects make the beam-steering essential for robust and low cost mmWave applications[40]. Electronic beam-steering is mainly implemented using either beam-switching approach or phased arrays. Following is a short summary about each of these two approaches.

### 1.3.1 Beam-Switching

A possible approach to enhance the SNR level is to generate multiple fixed directional beams by using a Butler matrix or Rotman lens[70]. Butler matrix and Rotman lens are generally composed of passive components. This leads to zero DC power consumption, a

huge advantage over active phased-array approaches. The beam-switching technique has the drawback of low spatial resolution due to the discrete beams which do not allow continuous type of beam-steering. Fig. 1.3 shows a recent design for the mmWave Rotman lens feeding antenna system[53]. The switching in the radiation pattern of this design is shown in Fig. 1.4. The beam-switching approach provides fast and low cost beam-steering solution.

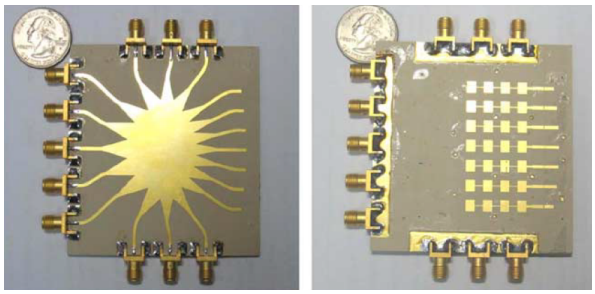

Figure 1.3: Five beams Rotman lens based compact design at 24GHz [53].

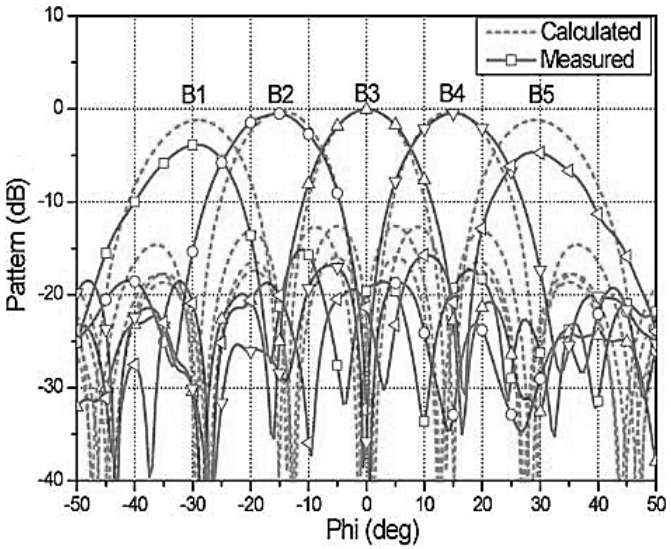


Figure 1.4: Five beams pattern from [53].

In [74], a 3-beam Rotman Lens is presented at 60 GHz. A picture of the proposed structure is shown in Fig. 1.5. The array factor is shown in Fig. 1.6. The array factor has

been calculated based on the measured S-parameters.

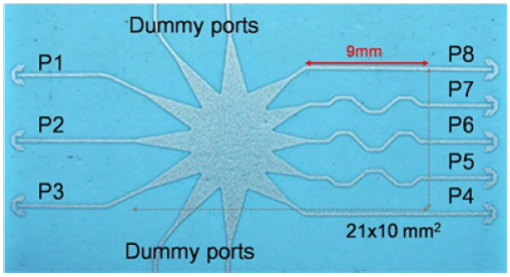


Figure 1.5: Picture of 60 GHz Rotman Lens [74].

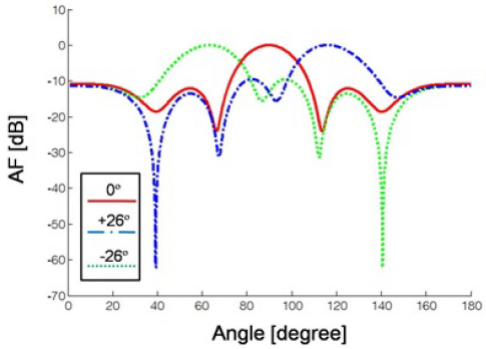


Figure 1.6: Three beams pattern [74].

### 1.3.2 Phased Arrays

In general, phased arrays provide higher resolution and higher gain than beam-switching configurations. However, for smaller arrays or for applications that require fast steering, beam-switched configuration can provide acceptable performance with reasonable cost. Beam-steering through phased arrays is performed by phase-shifting the RF signals of array antennas so that all phase-shifted signals become coherent for a particular radiation direction of interest. In general, phase shifting can be accomplished in the RF path, the IF/LO path, or at the baseband.

The phase shifting in the RF path is preferred because of the lower power consumption and chip size since only one RF transceiver is needed to connect to the RF phase shifting network. This also ensures a lower noise system and eliminates the need for distributing the LO which is very challenging at this frequency range. Fig. 1.7 shows an example design for a mmWave MEMS-based phased array transmitter.

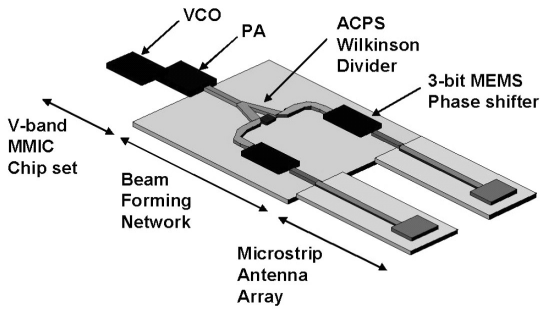


Figure 1.7: A two-element mmWave phased array system with passive beam-forming [55].

## 1.4 State of the Art for mmWave Planar Antenna Technologies

The wavelength reduction to millimeters makes the antenna dimensions very small, allowing wide variety of options for the mmWave antenna technologies. On-Chip antennas are among the different approaches for the realization of mmWave antennas. In [64], a 35 GHz on-chip antenna is presented in a low-resistivity silicon technology. The antenna efficiency is enhanced by using a high-permittivity and low loss rectangular dielectric resonator excited by an H-slot antenna implemented in a Silicon integrated circuit process. A picture of the antenna is shown in Fig. 1.8. A similar concept is shown in [34] for a complete radar transceiver (77 GHz) with two integrated antenna elements is presented. Two resonators are placed on top of the on-chip elements (See Fig. 1.9). In [71], a 16-element wafer-scale phased array transmitter at 110 GHz is presented. A picture of the proposed system is shown in Fig. 1.10. A 100 $\mu m$ quartz superstate layer is used for increasing the antenna's radiation efficiency. The total area is 6.45×5.95 $mm^2$.

In [10], we have proposed a high efficiency on-chip antenna at 710 GHz. The proposed antenna uses IHP SiGe process. We have used the $SiO_2$ layer as a low-loss substrate. The antenna structure has been shielded from the lossy bulk of the chip with ground. The antenna has a simulated gain of 2.25dBi at 710GHz and radiation efficiency of 31%. A 3D model of the proposed antenna is shown in Fig. 1.11. The Top view is shown in Fig. 1.12. A simplified cross section of the antenna is shown in Fig. 1.13. The simulated input matching of the antenna is shown in Fig. 1.14.

On-chip antenna is naturally integrated (Monolithic Integration) to the rest of the cir-

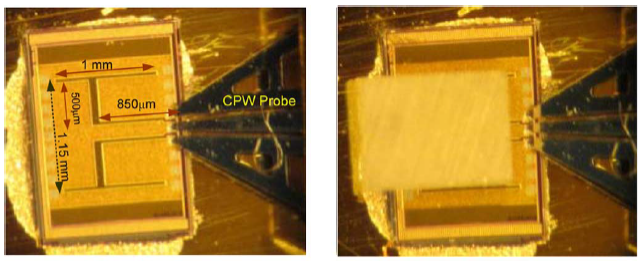


Figure 1.8: Example for on-chip antenna at 35 GHz (a) The dimensions of the H-slot aperture. (b) Die micrograph of the H-shape slot with DR and CPW probe [64].

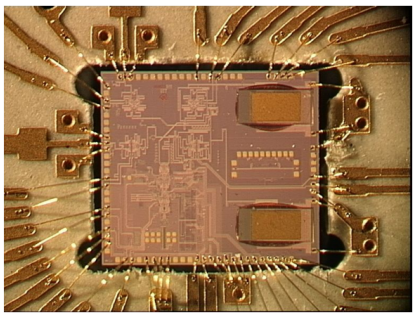

Figure 1.9: Example for on-chip antenna at 77 GHz [34].

cuit. This is a significant advantage over off-chip antenna since the integration options (such as wire-bonding, and flip-chip bonding at mmWave) are quite complex and lossy. On the other hand, the Silicon area used by the on-chip antenna is quite expensive. This makes large on-chip phased array antennas impractical from the commercial point of view. In addition, the efficiency of such structures are usually very low compared to structures which use low loss substrate for the antenna(s). Off-chip antenna solution is the cost effective high performance option for current mmWave applications. This type of solution can be referred to as Antenna in Package (AiP). The idea is simply to use a low loss substrate for the antenna and its feeding network and integrating this structure to the die (Hybrid Integration). Different antenna packaging technologies are competing for the emerging mmWave applications. The most popular ones are organic substrate [47], Low Temperature Co-fired Ceramic (LTCC) [78], and thin-film [43]. Following is a brief review of these technologies.

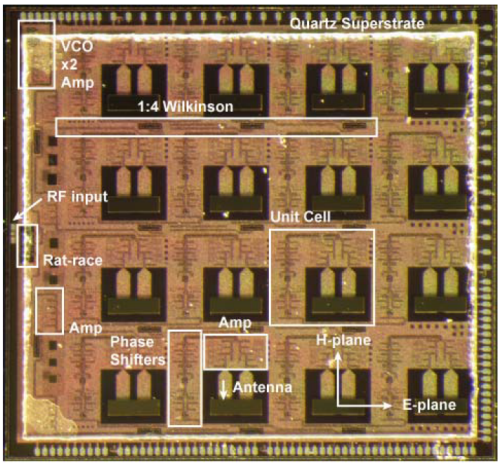


Figure 1.10: Example for on-chip antenna array at 110 GHz [71].

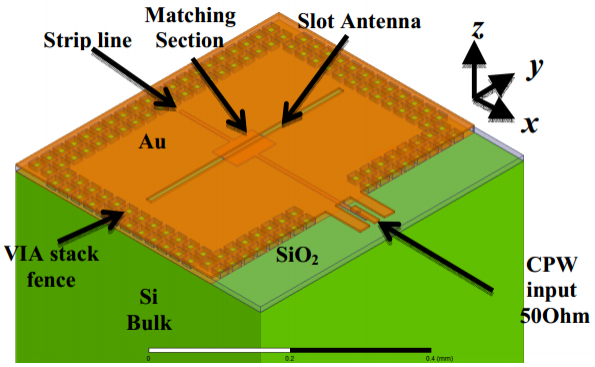


Figure 1.11: 3D model of an on-chip THz antenna (710GHz) [10].

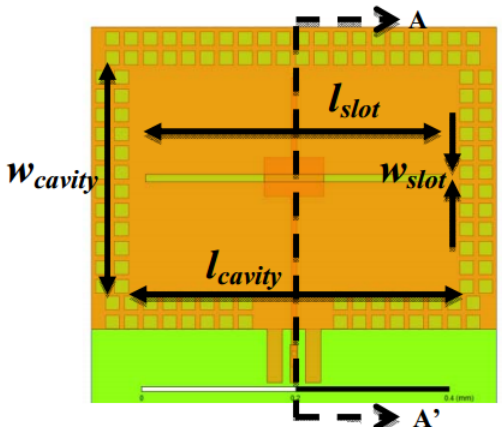


Figure 1.12: Top view of the proposed THz antenna [10].

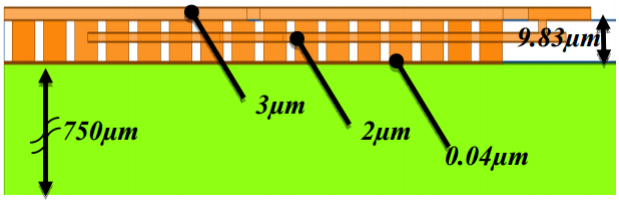


Figure 1.13: Cross-section A-A indicating different layers thicknesses [10].

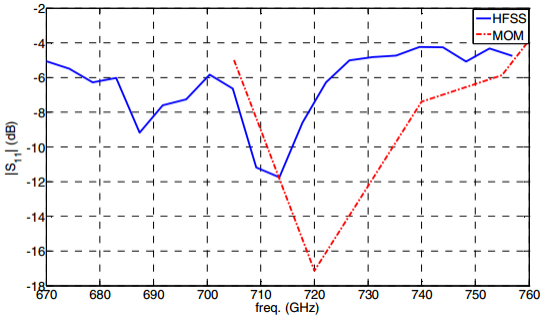


Figure 1.14: Simulated $S_{11}$ in dB [10].

### 1.4.1 LTCC Technology

LTCC technology has been popular in the RF packaging industry for its low-loss dielectrics, reliable multilayer implementation, relaxed VIAs design rules, and ease of integrating embedded passives (including flip-chip inside cavities). In [46], a fully-integrated AiP solution for 60 GHz phased-array system is demonstrated. Sixteen patch antennas are integrated into a $28 \times 28\ mm^2$ Ball Grid Array (BGA) together with a flip-chip attached transceiver MMIC. A cross section of the stack-up is shown in Fig. 1.15, while a picture of the complete solution is shown in Fig. 1.16. Similarly, [19] shows a more dense (32 elements) LTCC 60 GHz phased-array AiP (see Fig. 1.17). LTCC technology has been also used for AiP solutions at the W-band [18], 140 GHz [86] and even at 300 GHz [78]. However, at these higher mmWave frequencies, the demonstrated LTCC structures are only antennas with no active elements integrated.

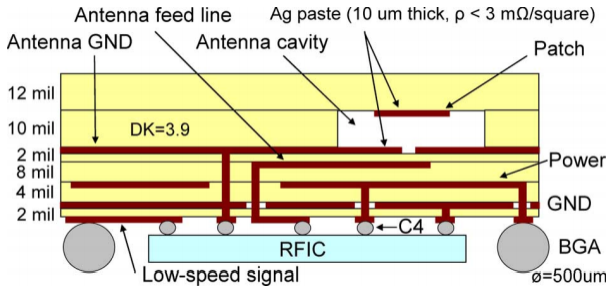


Figure 1.15: LTCC AiP example 1: Stack-up cross section [46].

Figure 1.16: LTCC AiP example 1: Picture [46].

### 1.4.2 Organic Multi-Layer Substrate Technology

AiP solutions using standard organic PCB processes and flip-chip assembly have the lowest fabrication cost and hence the most attractive antenna packaging approach for mass pro-

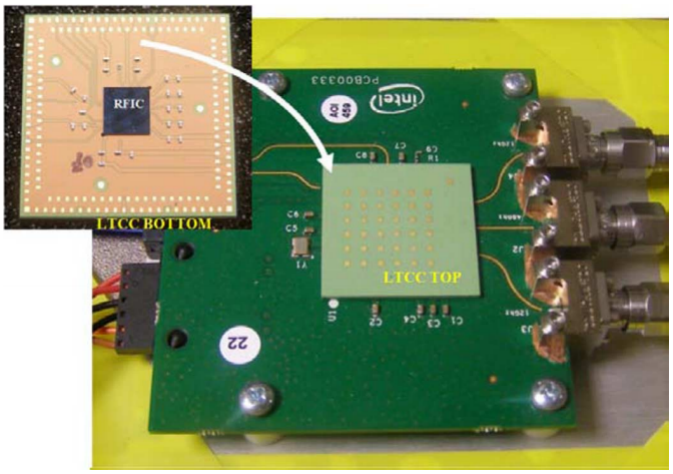


Figure 1.17: LTCC AiP example 2: Picture [19].

duction. However, the PCB tolerances do not scale easily with higher mmWave frequencies making the design task to meet the required performance very challenging. At 60GHz, a 16-element phased array is presented [47]. A cross section of the stack-up is shown in Fig. 1.18, while a picture of the complete solution is shown in Fig. 1.19.

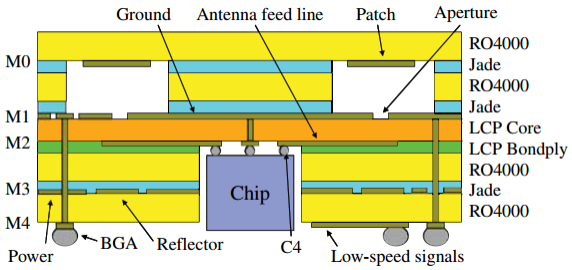


Figure 1.18: Organic AiP example 1: Stack-up cross section [47].

### 1.4.3 Thin Film Technology

Silicon micro-machining is definitely the most matured fabrication process. The tolerances and the yield are order of magnitudes better than normal PCB machining processes thanks to the advances in optical (and electron beam) lithography. This type of technology

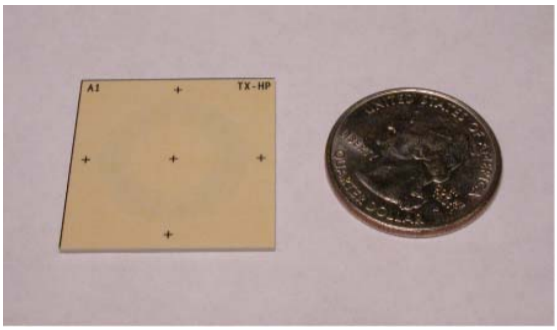

Figure 1.19: Organic AiP example 1: Picture [47].

is originally used for the active components but recently, passives, interposers, and antenna packages started to use similar techniques. High resistivity Silicon technology is commonly used for this type of packages for its high performance. HRS is available in different technologies such as SOI CMOS, Integrated Passive Device (IPD), and 3D integration Si interposer. In [80], a folded-slot antenna fabricated on HRS substrate is presented at 60 GHz (see Fig. 1.20).

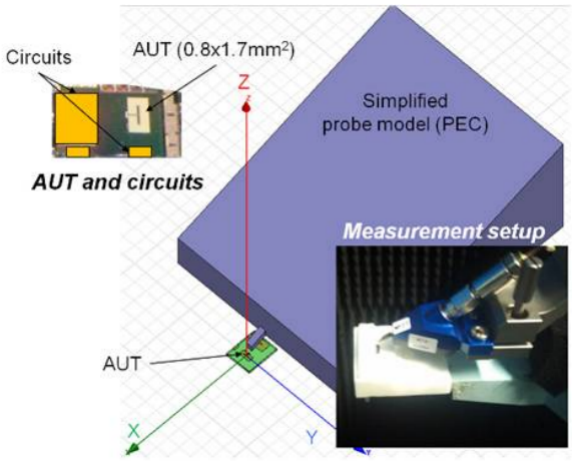


Figure 1.20: Thin Film AiP example 1: Picture, HFSS model and measurement setup [80].

Also, [43] presents a HRS substrate based antenna which operates at the W-band. A cavity inside the structure is formed using two wafers which are then bonded together (wafer scale integration). The antenna layers and the 3D view of the proposed AiP are

shown in Fig. 1.21 and Fig. 1.21, respectively.

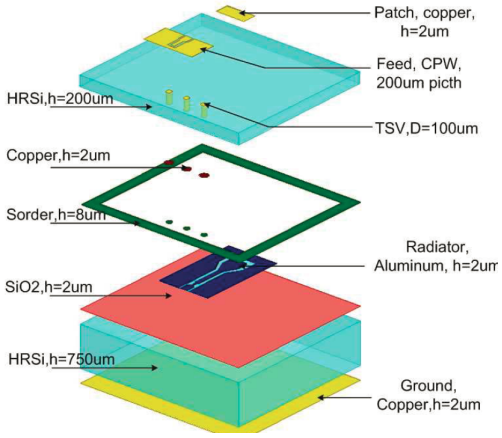


Figure 1.21: Thin Film AiP example 2: Exploded view of the antenna [43].

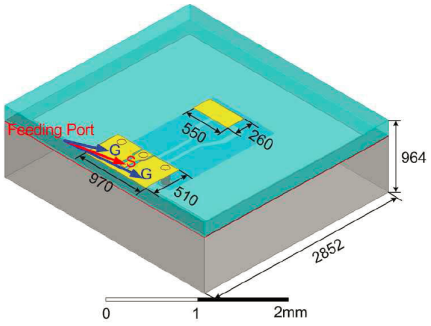


Figure 1.22: Thin Film AiP example 2: 3D view of the proposed AiP [43].

Another variant is the antenna fabricated on Glass substrate. In [16], a 60 GHz integrated antenna is presented. Fig. 1.23 shows the stack-up of the proposed antenna. A picture of the structure along with some measured/simulated data are shown in Fig. 1.24

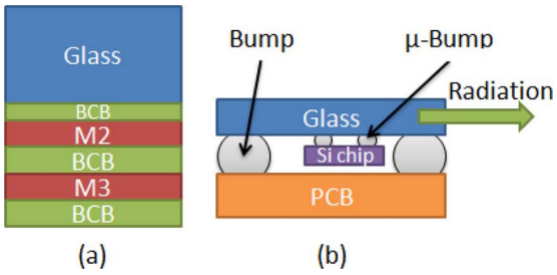


Figure 1.23: Thin Film AiP example 3: Stack-up [16].

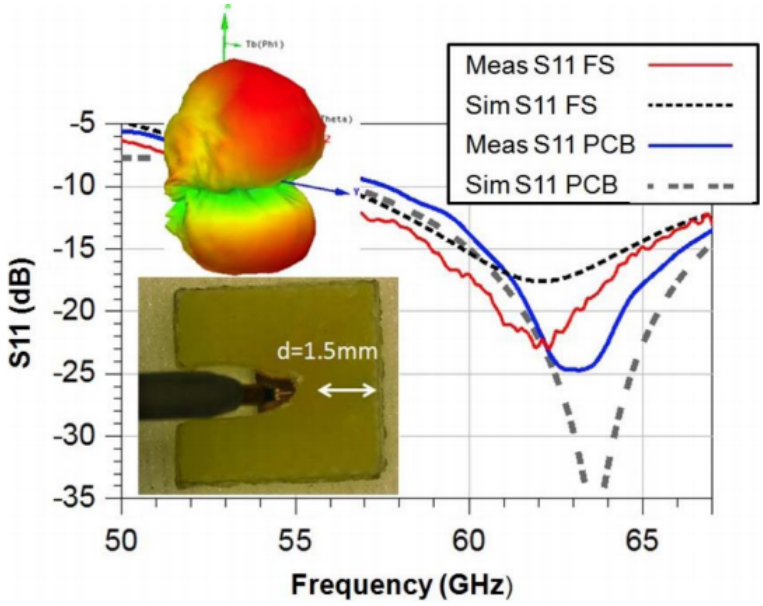


Figure 1.24: Thin Film AiP example 3: Picture and measured/simulated results in free space (FS) and the IPD/PCB package [16].

## 1.5 Current Options for mmWave Antenna Feed Circuits

Beam-steering implies using multiple antennas and hence the feeding network design is not simple. The feeding network is critical as it can deteriorate the whole antenna performance. This makes the choice of the transmission line an important decision in the design process. The most popular transmission lines/guiding structures used at mmWave are the Micro-Strip Line (MSL), the Co-Planar Waveguide (CPW), the Strip Line (SL) and waveguides. Planar waveguide technologies include the Substrate-Integrated-Waveguide (SIW), the Dielectric Waveguide (DWG), and the Dielectric-Image-Waveguide (DIG). All these types of transmission lines/guiding structures can be implemented by the various fabrication technology options presented in Section 1.4 (e.g. LTCC, Multi-layer PCB, and Thin-Film).

CPW, MSL and SL lines are well-established guiding structures for microwave applications. However, at high mmWave frequencies, high conductor losses and manufacturing tolerance problems start to appear and limit their performances. The main reasons are

the decrease in the skin depth, which increases the surface resistivity, and the dimensions shrinking (necessary to suppress unwanted modes and potential radiation). This causes current crowding and even higher losses.

On the other hand, technologies like metallic waveguide, are expensive and bulky. Attempts were made decades ago to develop microwave and mmWave circuits based on DWGs. The simplest and most widespread form of planar dielectric guiding structures is the image guide [51]. In [66], a synthesized version of the standard dielectric image guide, called the substrate integrated image guide (SIIG), is presented. It provides numerous advantages related to fabrication precision, design flexibility, and assembly cost, whereas it still retains the low-loss properties of its conventional counterpart in the mmWave range. This is achieved by artificially lowering the effective dielectric permittivity around a guiding channel through cutting a periodic pattern of air holes in a single high-permittivity substrate. Fig.s 1.25 and 1.26 show the model of the proposed waveguide. It is shown that guide attenuation values as low as 35 dB/m or 0.07 dB/$\lambda_g$ at 94 GHz can be obtained in practice with HRS as a substrate material. The measured insertion loss is shown in Fig. 1.27.

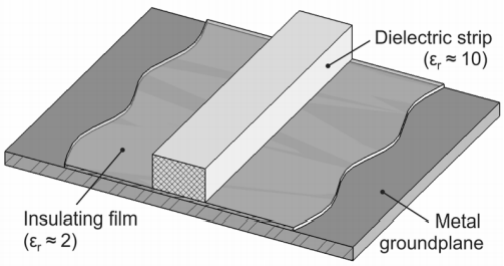


Figure 1.25: Insulated image guide [66].

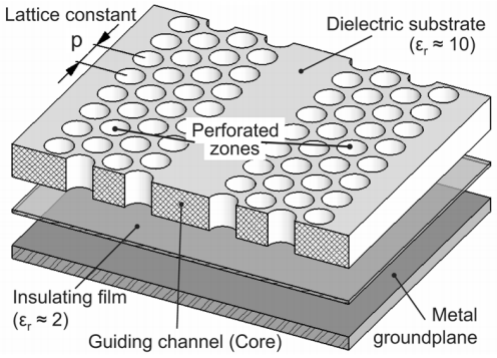


Figure 1.26: Exploded view of SIIG [66].

A non-radiative DWG is proposed [88]. The dielectric strip is sandwiched between two parallel metal plates separated by a distance smaller than half a wavelength. This dielectric guide is particularly applicable in mmWave integrated circuits, since it is not only small in size, but also allows bends and junctions to be incorporated into the circuits with very little radiation and interference. Fig.s 1.28 and 1.29 show the proposed structure schematics.

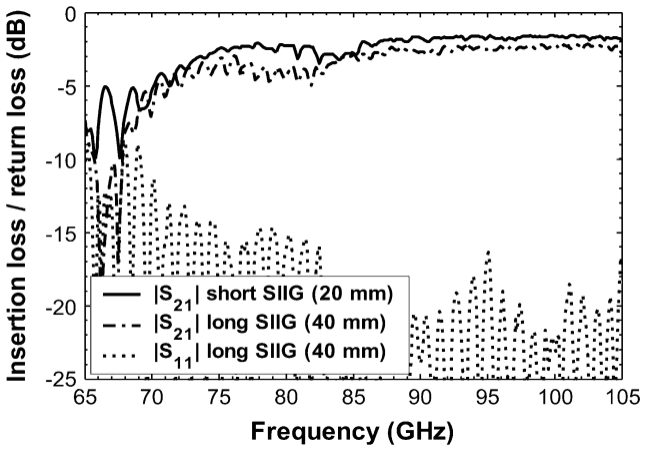


Figure 1.27: Measured insertion and return loss for the short and long SIIG sections fabricated of HR silicon. Losses arising from the two transitions are included. Core dimensions: 510 $\mu m\times$ 380 $\mu m$ ($w \times h$), insulation film thickness: 75 $\mu m$ [66].

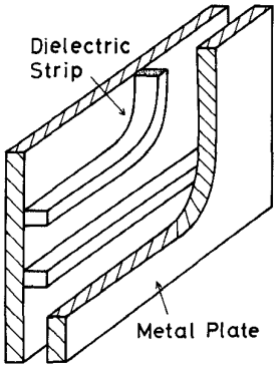


Figure 1.28: 3D view of a non-radiating dielectric waveguide [88].

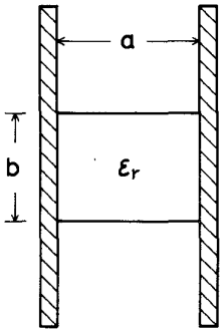


Figure 1.29: Cross section of a non-radiating dielectric waveguide [88].

## 1.6 Existing mmWave Phase Shifters

Typically, the RF phase shifters can be switch-based, ferrite-based, tunable material (like BST or LC), varactor-based, or MEMS-based. The ferrite-based phase shifters are highly linear and can achieve a low loss but their integration is challenging [52]. As for the low cost CMOS switches, they can not easily provide a large tuning range in addition to linearity issues. On the other hand, mmWave MEMS-based phase shifters can carry higher power and achieve lower loss, lower power consumption, and less parasitics. However, they usually have a relatively higher cost. A recent example of the mmWave MEMS-based phase shifter has been reported in [73]. The reported prototype showed an insertion loss better than $-5.1dB$ for a $7 \times 45^\circ$ phase shifter. The design consists of seven stages, each has a free $\lambda/2$ dielectric block which has an up and down state with a phase difference of $45^\circ$ at $75GHz$. Fig. 1.30 describes the structure of this phase shifter.

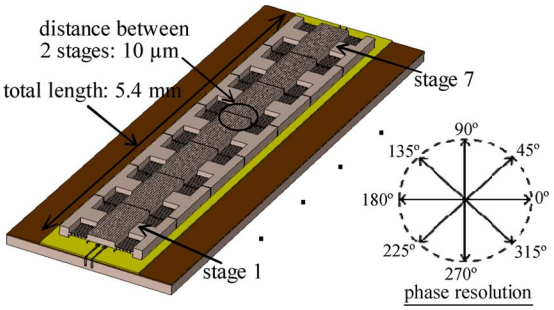


Figure 1.30: (Left) Schematical drawing of 360° seven-stage phase shifter and its (right) phase resolution[73].

## 1.7 Thesis Organization

Chapter 2 discusses the system level modeling of mmWave beam-steering solution and extracting antenna related specifications from general system specifications. Chapter 3 presents our proposed high performance antennas for beam-steering applications. Chapter 4 proposes our novel phase shifters while Chapter 5 discusses our proposed integration/packaging techniques for low cost and high performance mmWave systems. Finally, Chapter 6 summarizes the contributions of this work and discusses the future plan.

# Chapter 2

# Beam-steering System Requirements

Although beam-steering capability is frequently presented as a crucial feature for wireless mmWave systems, rigorous quantitative analysis taking into consideration the system level aspects are rarely reported. In this Chapter, a simple channel model is presented and applied to some practical wireless mmWave systems. Using the proposed model, this Chapter provides some meaningful comparison between single antenna system and beam-steering enabled ones.

## 2.1 Example 1: 60GHz Wireless Communication System Link Robustness

In this example, a 60GHz wireless communication system is considered. The main specifications are set by the Wireless Gigabit Alliance (WiGig) and the IEEE 802.11ad standard. WiGig is mainly used for high data rates (3Gbps) wireless communications within short distances (mainly indoor environment). The indoor environment at 60GHz is a multi-path rich environment. In Line-Of-Sight (LOS) situations, this multi-path effect can result in a severe degradation in the channel performance. This degradation can be categorized (from wireless communication perspective) into two types of fading; flat fading and frequency selective fading [84]. The frequency selective fading is usually dominant when the delay (path difference) is relatively big.

In Non-Line-Of-Sight (NLOS) situations, which are highly probable in the indoor channel due to the high loss of human body (50-60dB) at this frequency range [27], the multi-

path effect can useful in receiving the transmitted data through a reflected path. In summary, the main indoor channel model cases can be categorized as follows for simplicity;

- NLOS Scenario:
  *In this model, the LOS is blocked by an obstacle. This obstacle can be a human body which is very lossy at this frequency range. In this case, the link is established through the rays reflected from the wall as shown in Fig. 2.1.*
- LOS Scenario:
  *In this model, the reflected rays represent undesired interference which can (based on the delay and the strength) result in a severe fading. An example of this scenario is shown in Fig. 2.2.*

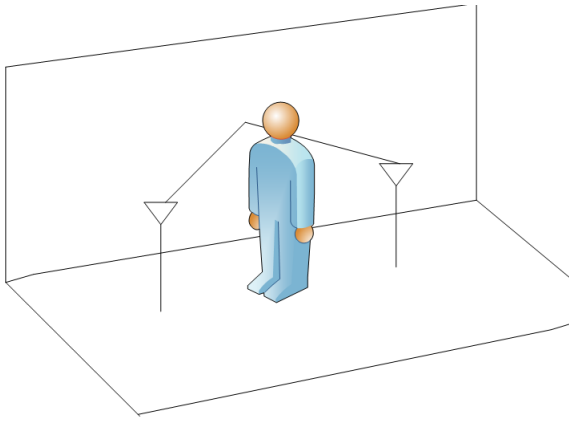

Figure 2.1: NLOS scenario.

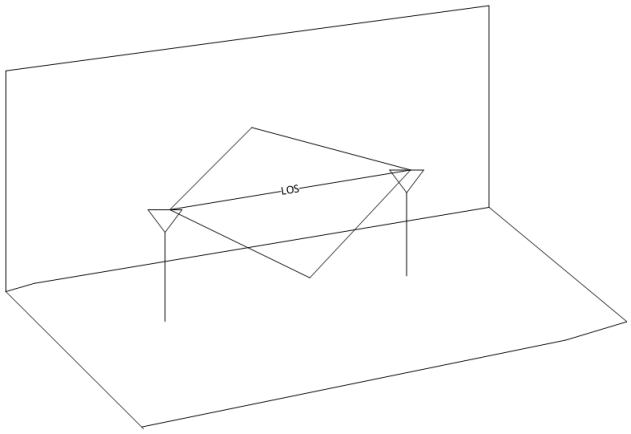


Figure 2.2: LOS scenario.

In the following analysis, a simple comparison is presented to show the importance of having a beam-steering enabled transceiver to enhance the coverage and the link robustness.

### 2.1.1 Model

A simple ray-tracing model has been developed and used to conduct this initial simulation. Although, we have developed a more comprehensive and advanced version of the ray-tracing modeling tool [7], we decided to use a simpler version in this example since the frequency is already too high and the multiple reflections rays are very weak.
**Antenna :** A linearly polarized patch antenna with a gain of 6dB has been used for the

single antenna case. For the array version, the array factor has been used assuming no coupling. The array element gain has been dropped to 5dB (due to the smaller ground). The antenna elements have been assumed to be half wavelength spaced for grating lobes free steering.

**Reflection Coefficient :** The reflection coefficient can be calculated using Snell's law. The formulas are given in Equations 2.1 and 2.2 [13], while the model used for these equations is shown in Fig. 2.3. Fig. 2.4 shows the Reflection coefficient calculated based on some reported material properties at 60GHz. In addition to the reported values, we have conducted simple measurements using standard horn antennas to verify the typical reflection coefficient values at 60GHz for some materials that normally exist in indoor environments.

$$\Gamma_{\parallel} = \frac{E^r_{\parallel}}{E^i_{\parallel}} = \frac{-\sqrt{\frac{\mu_1}{\epsilon_1}}cos\theta_i + \sqrt{\frac{\mu_2}{\epsilon_2}}cos\theta_t}{\sqrt{\frac{\mu_1}{\epsilon_1}}cos\theta_i + \sqrt{\frac{\mu_2}{\epsilon_2}}cos\theta_t} \tag{2.1}$$

$$\Gamma_{\perp} = \frac{E^r_{\perp}}{E^i_{\perp}} = \frac{\sqrt{\frac{\mu_2}{\epsilon_2}}cos\theta_i - \sqrt{\frac{\mu_1}{\epsilon_1}}cos\theta_t}{\sqrt{\frac{\mu_2}{\epsilon_2}}cos\theta_i + \sqrt{\frac{\mu_1}{\epsilon_1}}cos\theta_t} \tag{2.2}$$

A picture of the measurement setup is shown in Fig. 2.5. The setup is essentially two standard horn antennas with one connecting to a 67GHz PSG from Keysight (formerly Agilent) while the other is connected to a V-band waveguide calibrated Power Meter from Keysight (see Fig. 2.6).

Based on several measurements, the extracted Reflection coefficients for some materials in the lab/office environment are summarized in the Table 2.1. The Frii's formula for free space loss has been used (see Equation 2.3). The Oxygen absorption has been ignored due to the small distance. In addition, the materials we have used are thick and lossy enough to ignore the multi-layer internal reflections effect.

$$P_{RX} = P_{TX}G_{TX}G_{RX}(\frac{\lambda}{4\pi r})^2 \tag{2.3}$$

Where $P_{RX}$ is the received power after the antenna, $P_{TX}$ is the transmitted power, $G_{TX}$ is the gain of the transmitter antenna at the direction of the receiver, $G_{RX}$ is the gain of the receiver antenna at the direction of the transmitter (including the polarization

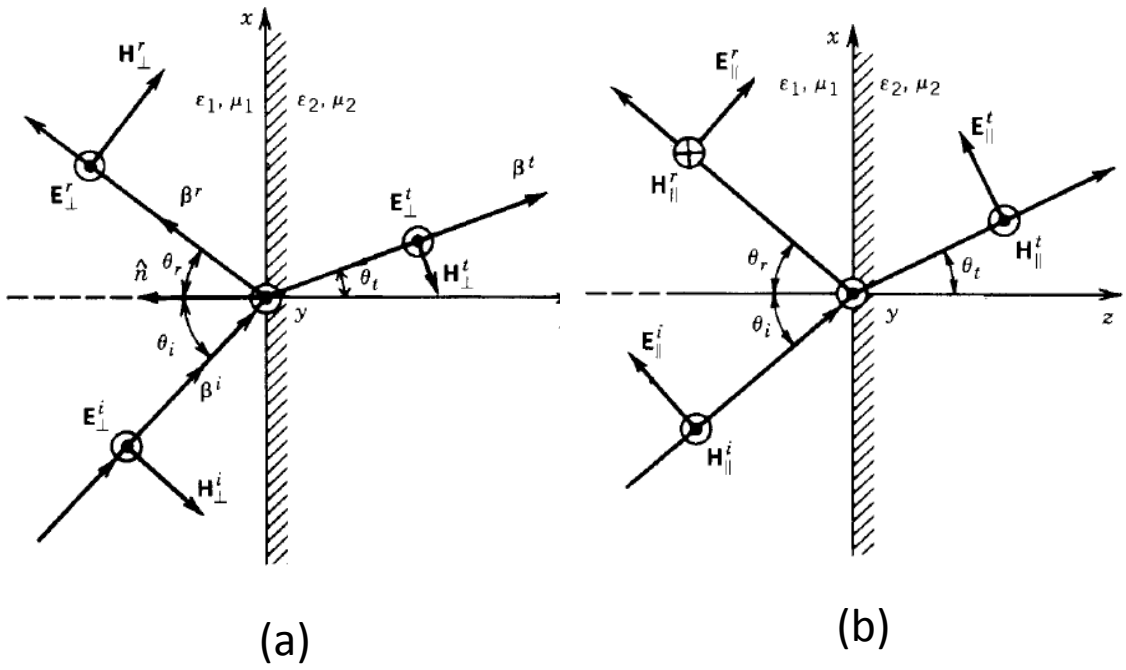


Figure 2.3: Diagram shows (a) normal polarized, and (b) parallel polarized plane waves incident at oblique angles [13].

mismatch), $\lambda$ is the free space wavelength and $r$ is the propagation distance.
**System Parameters :** These numbers are based on the data from a commercial 60GHz transceiver [45].

- RX NF = 6dB
- TX SNR = 45dB
- Pout = 11dBm
- BW = 2.16GHz
- Frequency = 60.48GHz (Channel 2)

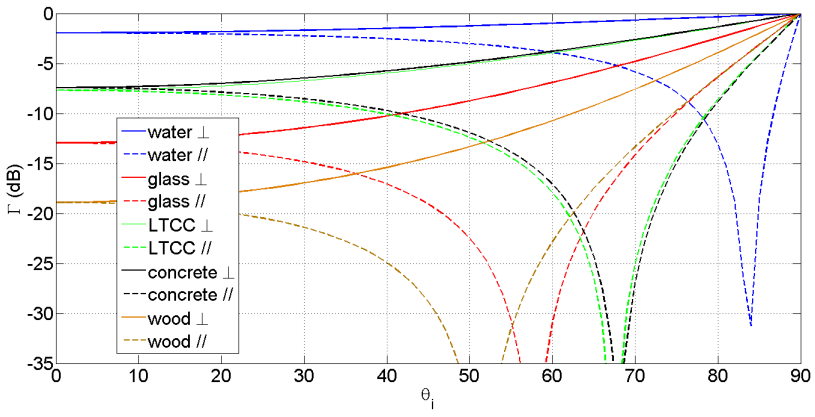


Figure 2.4: Calculated Reflection Coefficient vs the angle of incidence for different materials at 60GHz.

Table 2.1: Measured Reflection Coefficient for different materials at 60 GHz. V and H refer to the horn antenna vertical and horizontal polarizations.

| **Material** | **V** | **H** |
|---|---|---|
| Dry Wall | $R_{\perp}$=-3dB $\theta_i$=44$^o$ | $R_{//}$=-7dB $\theta_i$=45$^o$ |
| Ceramic | $R_{//}$=-10dB $\theta_i$=27$^o$ | $R_{\perp}$=-3.5dB $\theta_i$=27$^o$ |
| Carpet | $R_{//}$=-7.5dB $\theta_i$=21$^o$ | NA |
| Cubical Separator | $R_{\perp}$=-1dB $\theta_i$=34$^o$ | NA |

- Linear Polarization[1]
- Minimum MCS12[2] coverage in 5×5 (m$^2$) room = 90%
- Minimum SNR for MCS12 = 13.5dB

[1]The linear polarization is preferred over the circular polarization since for the NLOS circularly polarized antenna will suffer severe fading [57].

[2]Different modulation schemes and coding rates are represented by a Modulation and Coding Scheme (MCS) index value. MCS12 is a single carrier (not OFDM) $\pi/2$ 16QAM with 3/4 coding rate. It provides 4.62Gbps.

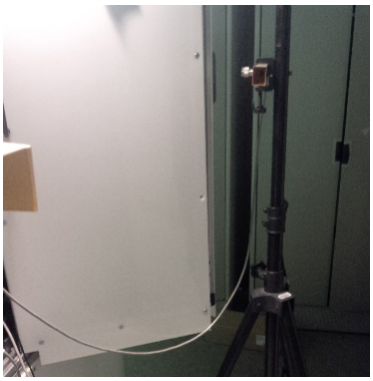

Figure 2.5: Picture of the setup used for measuring the Reflection Coefficient.

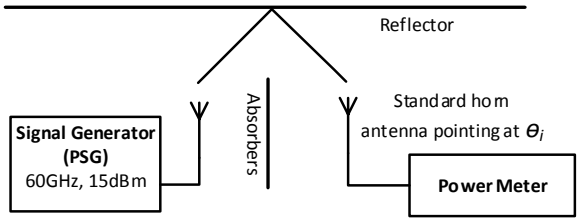


Figure 2.6: Block diagram of the setup used for measuring the Reflection Coefficient.

### 2.1.2 Simulation Results

**LOS Scenario :** A simple model has been used for this problem (see Fig. 2.7). For simplicity, the TX and RX are assumed to have the same height (L) over a flat big surface. Both TX and RX use a single element patch antenna. For the LOS with multi path scenario the single antenna transceiver fails to provide the required coverage. This can be explained by Fig. 2.8 which shows the SNR at the receiver ADC versus the distance between the TX and the RX. For Fig. 2.8, L is arbitrarily set to 0.5 m. Five graphs are shown, each represents a different Reflection coefficient value (R). As the reflection goes stronger, the ripple (flat fading) gets deeper. Based on some reports, R ranges from -5dB to -10dB at 60GHz. This fading limits the coverage for indoor LOS scenarios to less than 50% which is not acceptable in many applications.

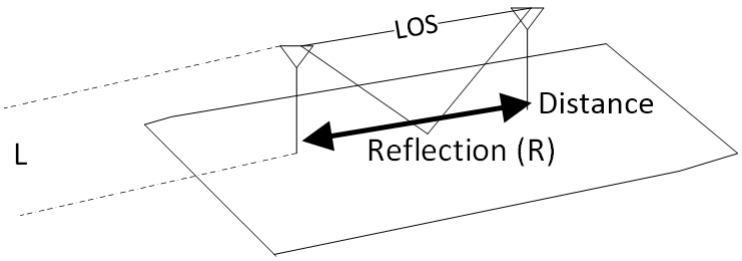


Figure 2.7: Simplified ray-tracing model used for LOS scenario.

Changing L affects the frequency of the ripples. Fig. 2.9 shows the multi-path effect with Reflection coefficient of -10dB on a single element antenna transceiver. The high values of L result in frequency selective fading, which can be compensated using equalization techniques, which we will not cover in this study.

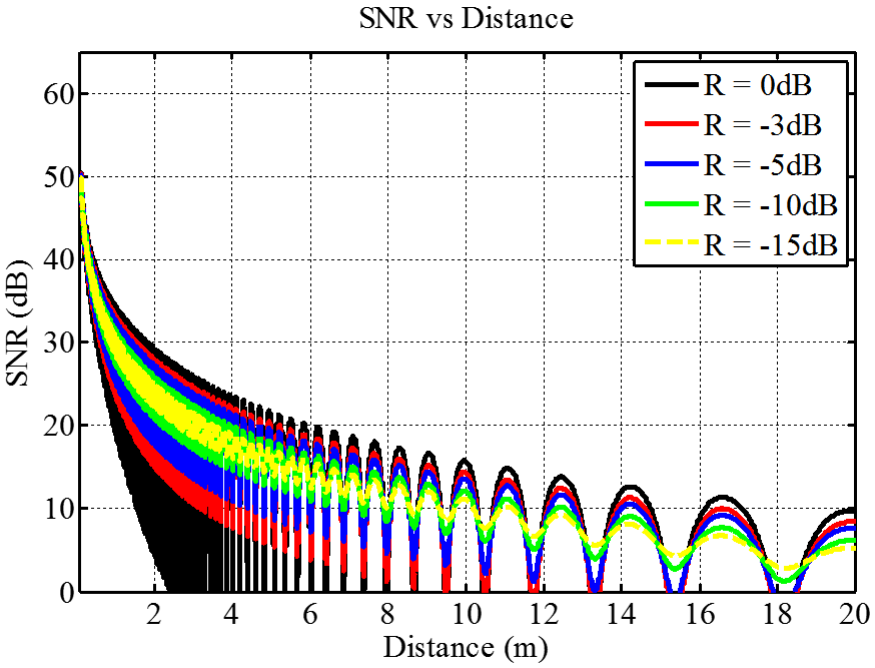


Figure 2.8: Flat fading for a single element/antenna radio.

Intuitively, using beam steering will solve the multi-path problem but we are interested

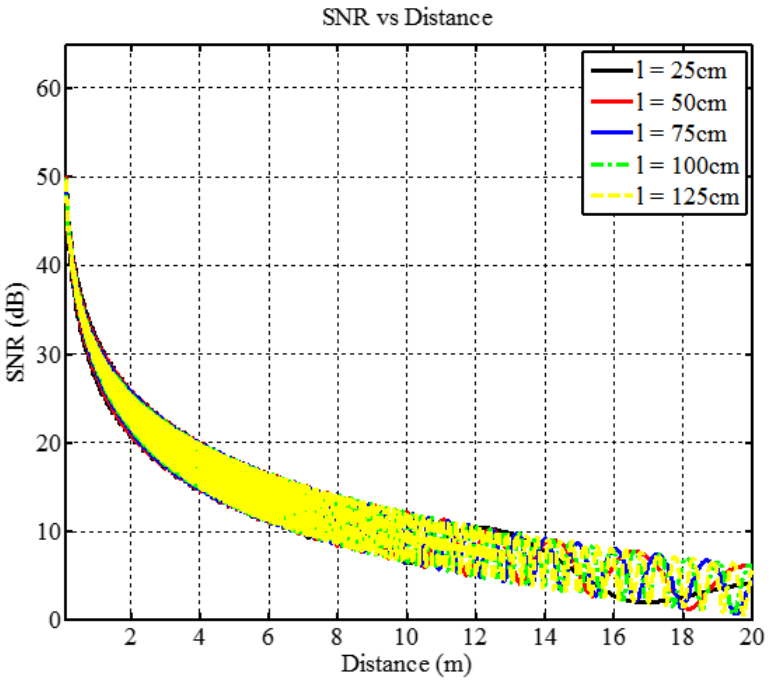


Figure 2.9: The effect of changing the height (L).

in proving that quantitatively. Fig. 2.10 shows the interferer's Angle-Of-Arrival (AOA) on the RX antenna for different situations. For this configuration, the desired signal is received at angle $0^o$; therefore, if the antenna beam-width is narrow enough to filter (spatial filtering) out the interferer signals, the system will be more immune to multi-path. The beam-width can be easily controlled by increasing the number of elements in a uniform linear antenna array setup as shown in Fig. 2.11.

For a uniform antenna array of four elements spaced at half wave-length distances (to suppress the grating lobes), the beam-width is approximately $25^o$. This narrow angle should be sufficient to suppress the interferer and reduce the flat fading effect as can be shown in Fig. 2.12. The immunity against multi-path gets even better with bigger antenna array 2.13.

**NLOS Scenario :** In NLOS scenarios, the link is mainly maintained through a reflected ray. Fig. 2.14 shows a simple model for NLOS situations. Antennas with steerable high gain beams can be adjusted to have their peak gain pointing towards the reflected path. Fig. 2.15 shows the SNR level at the receiver ADC for different types of antenna arrays.

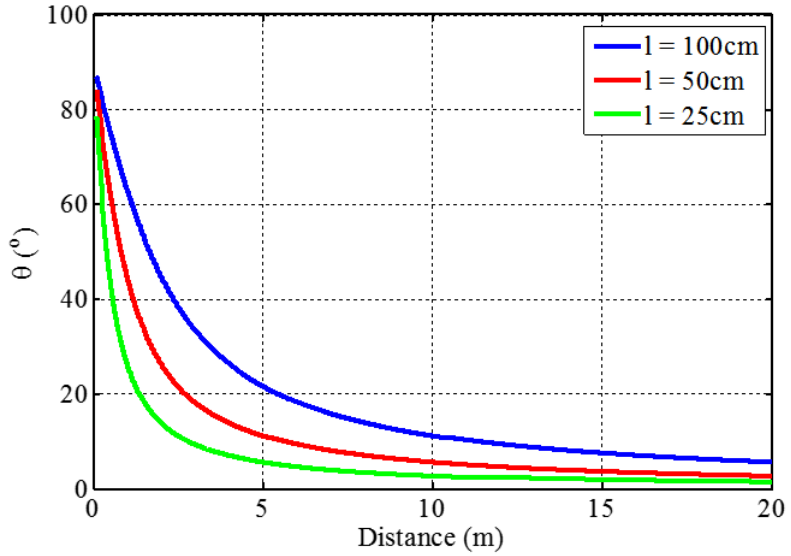


Figure 2.10: AOA for the interferer signal versus distance.

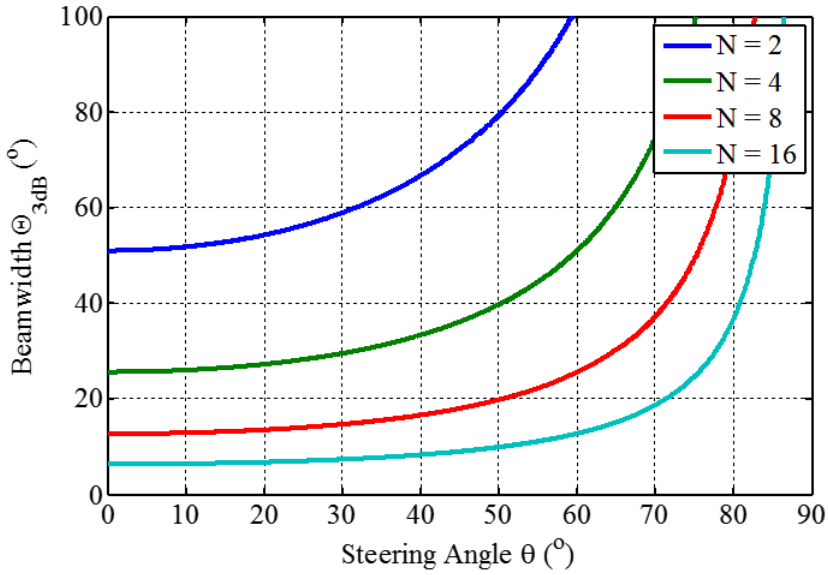


Figure 2.11: Beam-width for N-element arrays versus the steering Angle.

To decode MCS12 signal, a minimum value of 13.5dB is required. This means that at a four-element array is needed to maintain a good coverage in $5\times5$ ($m^2$) room (based on Fig.

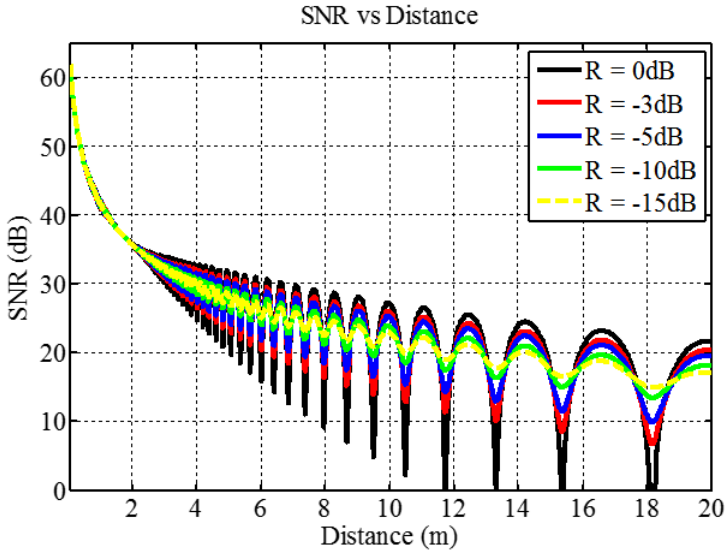


Figure 2.12: SNR versus distance for an array of four elements. This has been simulated at $L = 1m$.

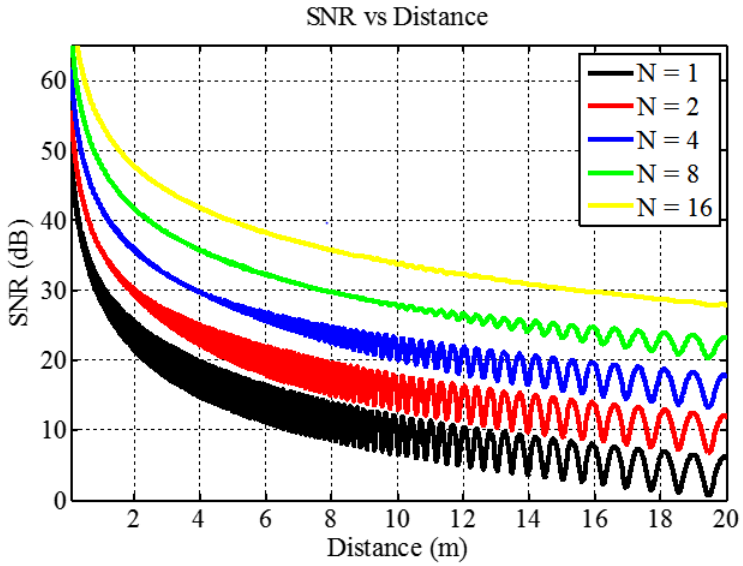


Figure 2.13: SNR versus distance for different antenna arrays simulated at $R = -10dB$ and $L = 1m$.

2.15). It is interesting to note that a higher reflection coefficient results in a more coverage as can be seen in Fig. 2.16.

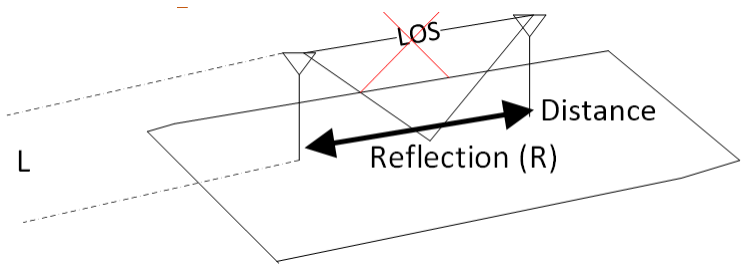


Figure 2.14: Simplified ray-tracing model used for NLOS scenario.

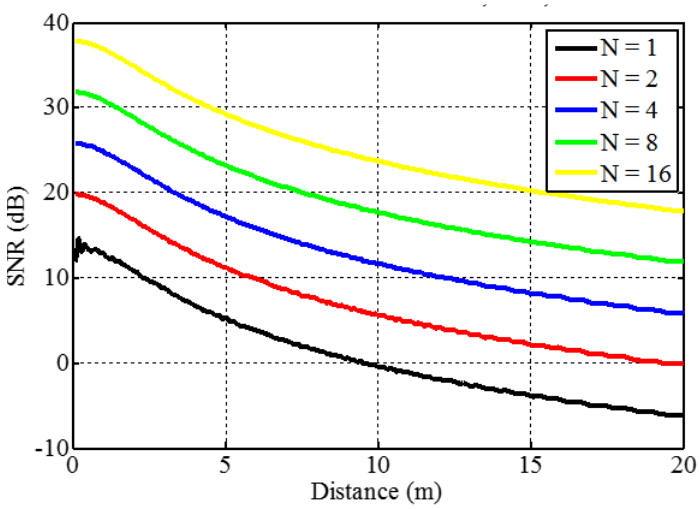


Figure 2.15: SNR (NLOS case) versus distance for different antenna arrays simulated at $R = -10dB$ and $L = 1m$.

### 2.1.3 Example 1: Summary

Based on the previous analysis the MCS12 coverage in a 5×5 ($m^2$) room has been calculated and the average values are given in Table 2.2. The coverage is calculated based on the 13.5dB threshold for SNR. The NLOS cases have been assumed to occur 20% of the time

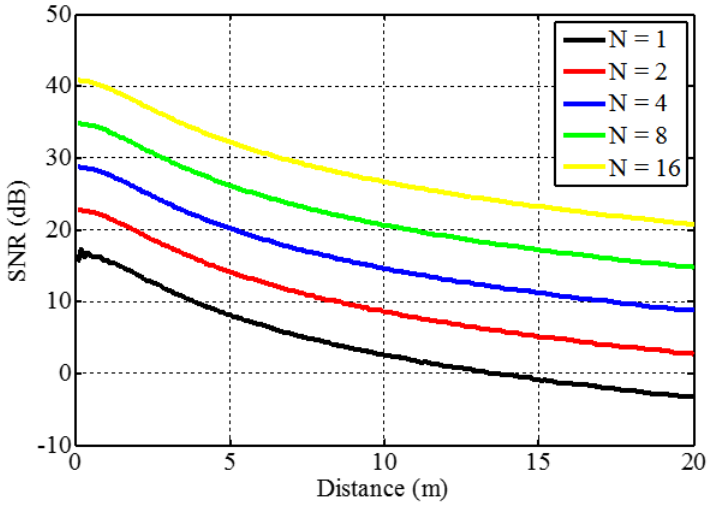


Figure 2.16: SNR (NLOS case) versus distance for different antenna arrays simulated at $R = -7dB$ and $L = 1m$.

while the LOS ones with multi-path have been assumed to occur 80% of the time. The calculated coverage represents statistical averages across many simulations for different practical values of R and L in indoor (office) environment.

Table 2.2: Coverage in a 5×5 ($m^2$) room.

| **N** | **1** | **2** | **4** | **8** |
|---|---|---|---|---|
| **Coverage** | 41% | 77% | 97% | 99% |

Based on Table 2.2 results, an antenna array of $4 \times 4$ elements is needed for the proposed application. The beam steering itself it can be realized using either beam-switching techniques (discrete scanning) or using phased array (continuous or quasi-continuous scanning). Since the number of elements is $4 \times 4$, phased array antenna technique should provide slightly better performances. For smaller arrays, phased array antennas and switched-beams antennas provide similar performances. In some applications, fixed arrays with mechanical rotation/steering is also possible. However, this approach is not feasible due to the size, the cost and the speed limitation[3].

[3]The beam switching requirement should be less than 10 nsec to switch between two beam locations in

We have recently proposed a novel design for a 4 × 4 phased array antennas which significantly simplifies the integration [1]. The proposed architecture significantly reduces the number of phase shifters from N2 to 2N (in this case N=4), the packaging complexity, and the power consumption. Simple schematics that show how this has been done are shown in Fig. 2.17 and Fig. 2.18. The idea is based on the inherent orthogonality in the feeding network between the column and row excitation modes.

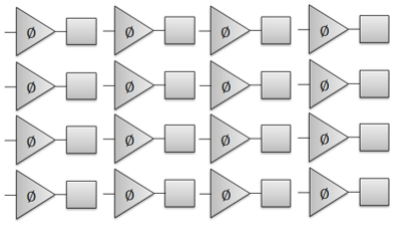

Figure 2.17: Conventional 4×4 phased array patch antenna [1].

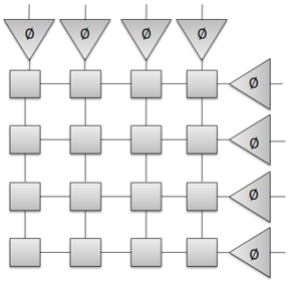

Figure 2.18: Proposed 4×4 phased array patch antenna [1].

## 2.2 Example 2: Automotive Radar (77GHz/79GHz)

The automotive radar is becoming a key technology for the future intelligent transportation systems. However, the antenna requirements of automotive radar systems are yet very challenging. These requirements include the antenna size, cost, loss, range, angular resolution, field of view, thermal stability, and bandwidth [5]. In this example, the antenna and beam-steering requirements for a typical 77GHz/79GHz short-range FMCW 2D automotive radar will be analyzed briefly.

### 2.2.1 Antenna Requirements

**Angular Resolution :** The resolution represents how close two objects can be before the radar fails to distinguish between them. For a short range automotive radar, the required

the WiGig application.

angular resolution is typically $10^o$. This imposes a condition on the beam-width of the antenna. For antenna array implementation, the number of elements is at least 8 elements in the scanning plane (see Fig. 2.11).
**Range :** For a short-range automotive radar, the detection range is typically 50meter (see Fig. 2.19). This imposes a certain antenna gain requirement. A simple formulation to calculate the required gain is shown below.

$$P_{RX\,sensitivity} = \frac{P_{out} G^2 \sigma \lambda^2}{(4\pi)^3 Range^4} \tag{2.4}$$

Using these equations and for the radar system specified below, the required antenna gain $G$ is found to be 21dBi. For antenna array implementation, this can be satisfied with 64 ($8 \times 8$) elements patch antenna array.

- Pout = 10dBm
- BW = 4GHz
- $P_{RX\,sensitivity}$ = -53dBm (This is calculated based on the NF, the BW and the minimum detectable SNR.)
- $G_{TX} = G_{RX} = G$(Same antennas for TX and RX.)
- Margin = 5dB (A value added to the sensitivity analysis to allow some margin for other types of losses not taken into consideration in the simplified equations.)

**Field-Of-View :** The Field-Of-View (or the field of detection) is a critical spec for automotive radar as it defines the maximum angular range that can be detected by the radar. Normally, detection in all directions is preferred; however, the front FOV is the most critical requirement. This front FOV can be easily calculated based on the maximum number of lanes in a street/high-way.

Typically, the short-range radar FOV is $\pm 40^o$ (see Fig. 2.20). For antenna array implementation, the FOV value determines the required antenna spacing since the FOV has to be grating-lobes free. The maximum element spacing (based on $\pm 40^o$) is 0.65 $\lambda$.

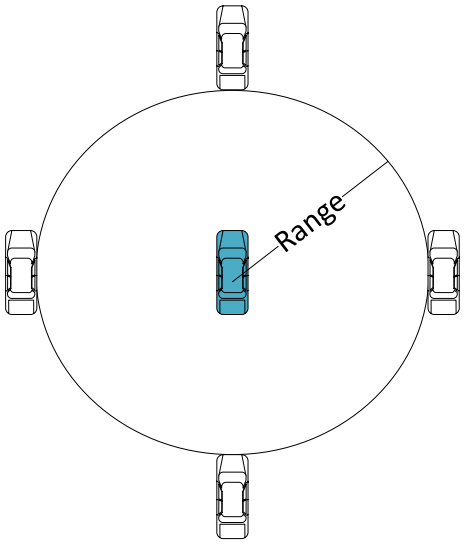


Figure 2.19: The range is the maximum distance at which the car/obstacle can be detected by the radar.

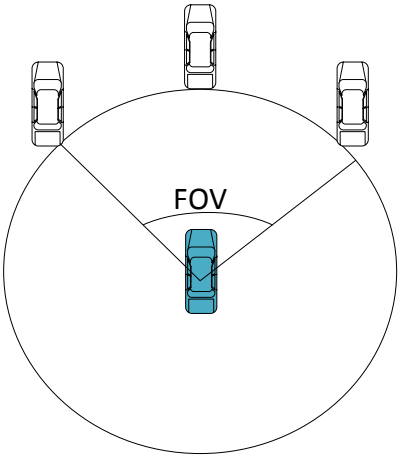


Figure 2.20: The Field-Of-View defines the maximum range of angles that can be detected by the radar.

### 2.2.2 Example 2: Summary

Based on the previous discussion, an antenna array of 0.65 $\lambda$ spaced $8 \times 8$ elements is suitable for the 77GHz/79GHz short-range 2D automotive radar. Because it is 2D scanning radar, the antenna can be considered as a 1D array of 8 elements. While each element can be a travelling wave antenna of 8 patches. The antenna gain has to be at least 21dB which is quite possible since the ideal gain is 24dB. A 3dB is considered as a margin for the feed and the antenna losses.

The bandwidth for the antenna is 4GHz. This will require a non-uniform design for the antenna array to avoid frequency scanning. For eight elements antenna, the performance of a phased array system is quite similar to RF beam-switched configuration. A schematic for the proposed implementation is shown in Fig. 2.22.

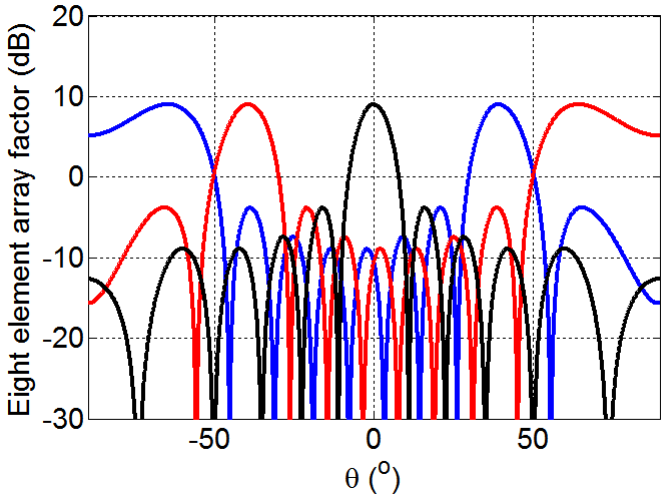


Figure 2.21: Array factor for eight elements antenna array with a 0.65 $\lambda$ spacing showing the center beam and the $\pm 40^o$ beams.

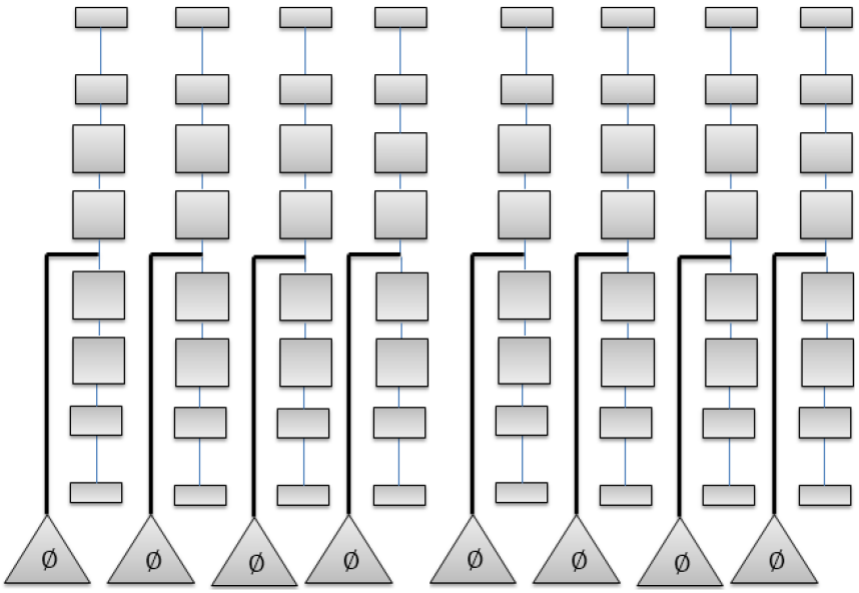


Figure 2.22: A schematic for the proposed radar antenna.

# Chapter 3

# Novel HRS DWG-based Antennas

HRS DWG based platform has been proposed as a low cost and a high efficiency solution for mmWave/sub-THz applications. This Chapter discusses the design, optimization, fabrication and measurement of novel fully dielectric antenna structures for mmWave beam-steering applications. The proposed high performance antennas can be easily integrated with the HRS DWG based platform.

## 3.1 Dielectric Waveguide

DWG-based platform provides excellent performance characteristics for mmWave applications. In this Section, some well-known dielectric waveguide options which will be used later in this research are briefly discussed. Simple design techniques are also covered in this Section. The dielectric material used in this study is High Resistivity Silicon (HRS) with a dielectric constant ($\epsilon_r$) of 11.9 and a resistivity of ($\rho$) $3.2K\Omega cm$.

#### Why DWG at mmWave?

Planar transmission lines (CPW, MSL and SL lines) are well-established guiding structures for microwave applications. However, at these high frequencies, high conductor losses and manufacturing tolerance problems start to appear. For example, the small skin depth at mmWave results in high losses related to the conductor surface roughness. The skin depth is defined by Equation 3.1 [13]. Fig. 3.1 shows the skin depth frequency variations for

different metals. As an example, the copper skin depth at 77GHz is $0.24\mu m$ while the typical surface roughness value varies from 1 to $2\mu m$. This means that the current flow in such structure (see Fig. 3.2) introduces parasitic inductances which change the surface impedance and create losses.

$$\delta = \frac{1}{\omega\sqrt{\mu\epsilon}} \frac{1}{\sqrt{(\frac{1}{2}[\sqrt{1+(\sigma/\omega\epsilon)^2}-1])}} \tag{3.1}$$

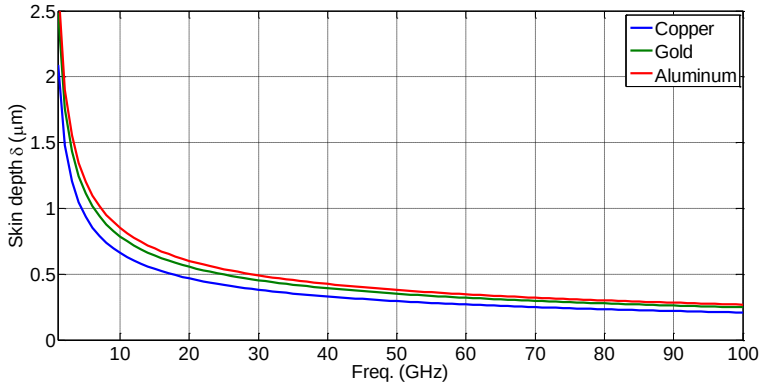


Figure 3.1: Skin depth variations with frequency for different conductors.

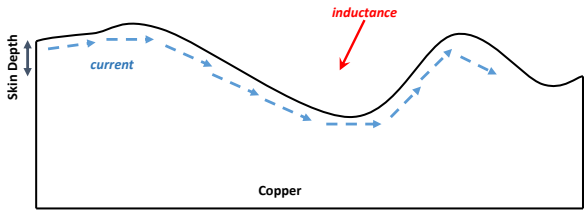


Figure 3.2: surface roughness effect at mmWave.

In addition to this type of loss (which is normally the dominant component at mmWave range), there is the conductor attenuation due to the finite conductivity of the metal as well as the dielectric loss. Furthermore, for CPW and MSL transmission lines (the copper is exposed in air) different types of surface finishing (such as ENIG[1]) are usually used.

[1]ENIG is electroless nickel immersion gold surface finishing which is usually used in PCB for protecting the copper and for flip-chip bonding.

This results in even higher loss. Typically a good CPW line design at 77GHz is expected to have about -2dB of loss in 1cm while a good DWG, as will be shown later, has less than half of this loss since it suffers only one type of loss which is the dielectric loss.

To further investigate the loss characteristics of CPW lines. We have designed and fabricated a 1 mm long CPW line of gold on the same high resistivity Silicon substrate (see Fig. 3.5). As shown in Fig. 3.3, we have measured the gold surface roughness and its RMS value has been found to be $0.5\mu m$. Fig. 3.4 shows the insertion and the return loss of the CPW line measured up to 50GHz. The loss at 40GHz is -0.28dB. If we ignore the mismatch, the intrinsic loss will be -0.14dB (-1.4dB in 1cm or -1.87dB/$\lambda_o$). Since we have fabricated this CPW line with expensive gold evaporation process on HRS substrate, the loss characteristics are much better than the normal PCB CPW lines which use rough copper foils on low-cost polymer substrates. The loss gets higher at higher mmWave frequencies. This loss usually limits the use of these types of transmission lines in high performance antenna feed circuits to frequencies below 100GHz.

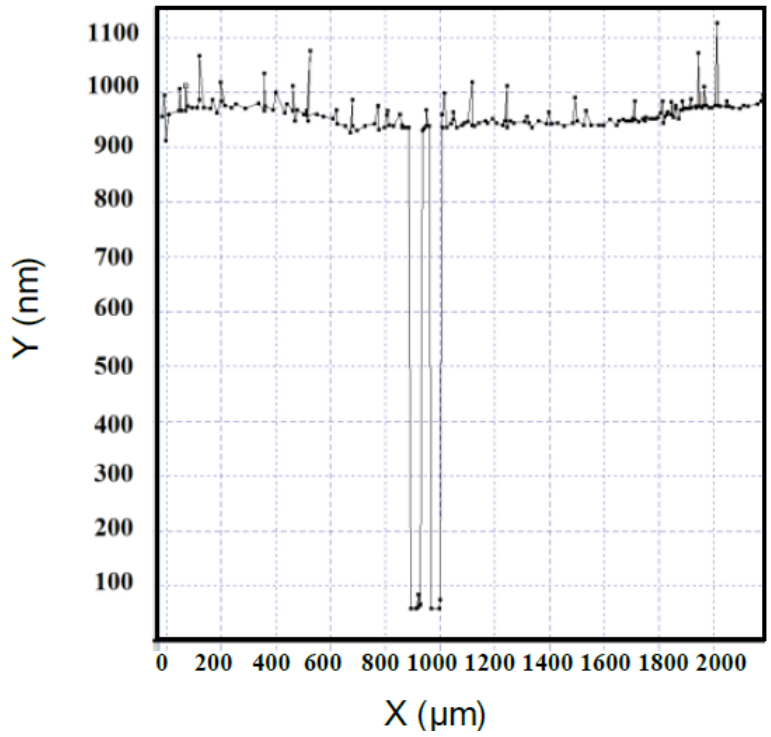


Figure 3.3: Measured surface roughness of CPW metallization on HRS substrate.

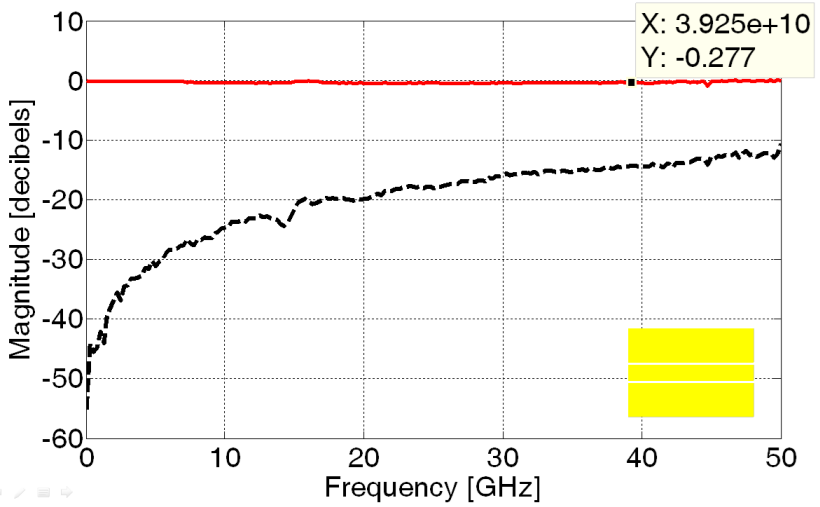


Figure 3.4: Measured S-parameters for 1mm CPW line on HRS substrate.

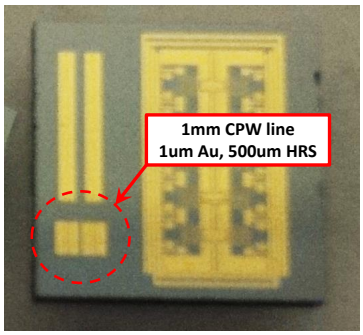


Figure 3.5: Picture of the fabricated test structure.

### 3.1.1 Dielectric Slab Waveguide

The dielectric slab (see Fig. 3.6) is the simplest type of dielectric waveguides and its analysis can be also used in designing the rectangular cross section dielectric waveguide (which is of more interest to us) as will be shown later. As shown below, the dispersion equations of the dielectric slab which can be deduced from the boundary conditions. One classical, yet efficient, method to simultaneously solve the dispersion equations is to use a 2D plot, we will refer to this method as the graphical method [67] and Fig. 3.7 shows the application of the graphical method.

$$(k_c d)^2 + (hd)^2 = (\epsilon_r - 1)(k_o d)^2, \tag{3.2}$$

TM

$$(k_c d)tan(k_c d) = \epsilon_r hd. \tag{3.3}$$

TE

$$-(k_c d)cot(k_c d) = hd. \tag{3.4}$$

Also, the numerical solution for the dispersion can be easily found using many commercial

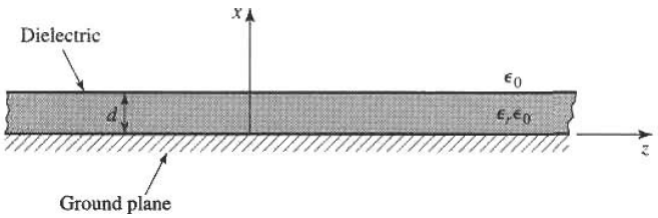


Figure 3.6: Grounded dielectric slab [67].

software packages which have eigen mode solver such as COMSOL and HFSS. Fig. 3.8 shows the 2D model we used to solve the grounded dielectric slab in the HFSS eigen mode solver.

#### Numerical Example

Having a grounded dielectric slab with $\epsilon_r = 11.9$, and thickness= $0.233mm$ working at $f = 77GHz$,

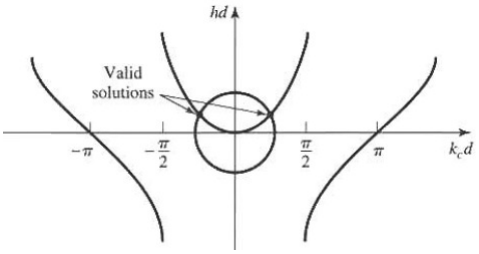


Figure 3.7: Graphical method [67].

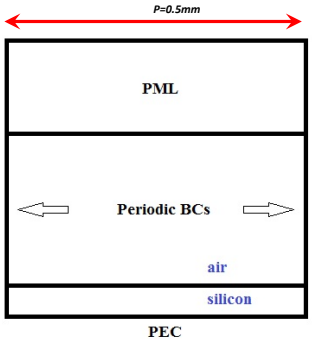


Figure 3.8: 2D model in HFSS.

- First mode solution using an HFSS eigen mode solver (as shown in figure 3.9):$\beta p = 57.2°, p = 0.5mm \Rightarrow \beta = \frac{57.2° \times \pi}{180° \over 0.5 \times 10^{-3}} = 1.99 \times 10^3 m^{-1}$
- First mode solution using the graphical method (as shown in figure 3.10):$\Rightarrow \beta = \sqrt{(\epsilon_r \times (2\pi f/C)^2 - (1.205 \times 2/d)^2)} = 2.06 \times 10^3 m^{-1}$

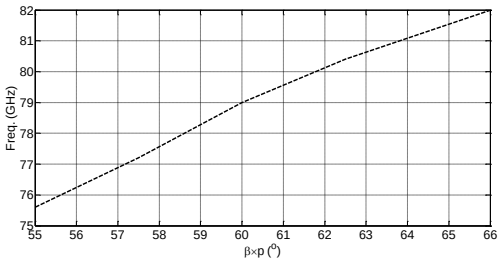


Figure 3.9: HFSS eigen solution.

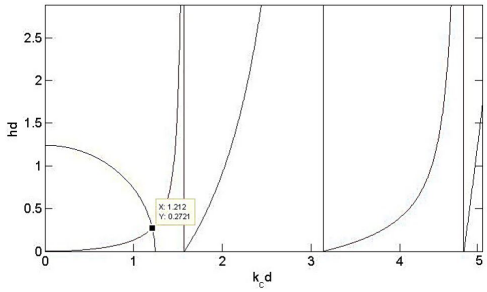


Figure 3.10: Gaphical method.

### 3.1.2 Rectangular Dielectric Waveguide

As mentioned earlier, the dielectric waveguides are more attractive at mmWave frequencies because of their lower propagation loss and lower cost. In the case of the circular cross section, the electromagnetic problems related to the dielectric waveguides can be solved in closed form in terms of the Bessel functions [29]. In the case of the rectangular cross section however, no closed-form solution exists. There is no rigorous analytical method

suitable for the analysis of rectangular dielectric waveguides. But since rectangular cross section waveguides are easier to fabricate and easier to integrate, it is of great interest to this research. The detailed discussion on the analysis of these waveguides are presented in [54]. There are some approximate models, like the Marcatilis method, which can be used to design rectangular waveguides [58]. The Marcatili's method solves two dielectric slabs to find the solution for the waveguide (see Fig. 3.11).

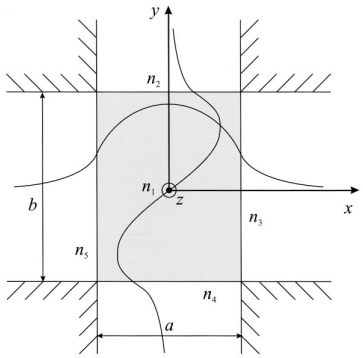


Figure 3.11: The geometry of a rectangular dielectric waveguide in Marcatili's method and the distribution of $H_x$ for the $E^y_{12}$mode[58].

For this research, a commercial solver (HFSS) has been used to extract the dimensions of the waveguide design. Dielectric Image Guide (DIG) is the easiest (from the realization point of view) type of DWG. It has perfect performance characteristics at the mmWave range up to $200GHz$ approximately. Beyond this frequency, DWG is significantly better. The cross section is shown in Fig.3.12. The dimensions of the cross section are $0.7mm \times 0.5mm$. The dominant mode is $E_y$ (y is normal to the ground conductor).


Figure 3.12: Silicon image waveguide

**Experimental Example**

For verification purpose, we have fabricated a rectangular cross section Dielectric-Image-Guide (DIG). A picture of the fabricated DIG in the measurement setup is shown in Fig.

3.13. The measured magnitudes variations with frequency for $S_{21}$ and $S_{11}$ are shown in Fig. 3.14. The total insertion loss is -1.8dB at 90GHz. This is -0.9dB after de-embedding the transition loss which means that the DIG loss is -0.45dB in 1cm or -1.35dB/$\lambda_o$. The structure is matched over the frequency band of interest except for small Fabry Perot resonances due to the mismatch introduced by the two transitions (the transition details is covered in the Chapter 5).

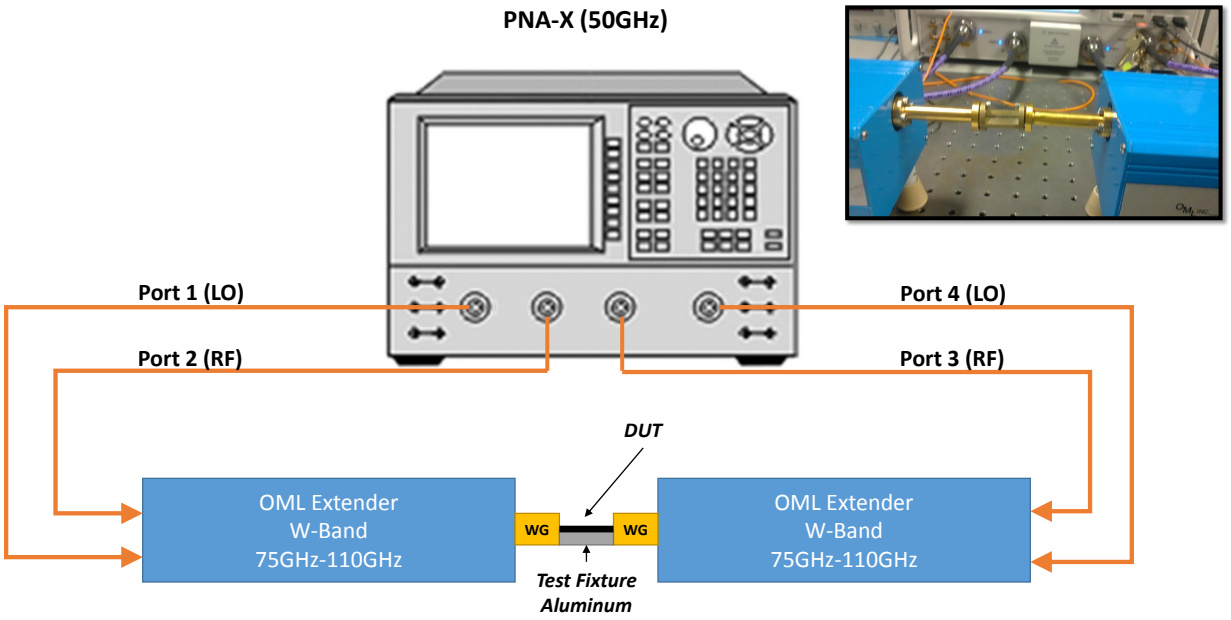


Figure 3.13: Measurement Setup.

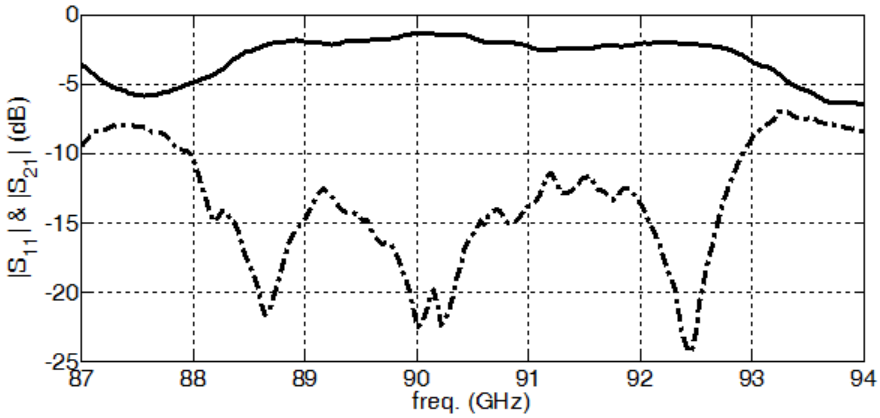


Figure 3.14: Measured $S_{21}$ and $S_{11}$ magnitudes variations with frequency.

## 3.2 Novel DWG-based Multi-Beam Grating Antenna

The simplest and the fastest electronic beam-steering approach is beam-switching. The beam-switching is usually achieved by using an antenna system with a fixed set of directional beams. The system selects the desired beam/direction using an RF switch(s). This technique provides lower cost and faster beam-steering (compared to phased arrays) but it also normally has a low spatial resolution due to the finite number of beams. The typical switching time of the available commercial switches operating at the mmWave band is in the order of few nanoseconds. This makes the beam-switching based antenna systems ideal for many mmWave applications with strict timing requirements. In addition, for low antenna gain (small antenna/fewer number of elements) applications, the angular resolution is already limited by the wide beam-width of the antenna array. In such cases, the discrete nature of beam-switching based antenna systems can not be considered as a significant disadvantage.

To achieve a very wide scanning coverage, quasi-optics type Beam-Forming Networks (BFNs) are mainly used, such as the Rotman lens [70], [74]. The Rotman lens based switched beam system has been extended to 360 ° of scanning. The Rotman lens design procedure at mmWave is a bit complicated. In addition, Rotman lens suffers from problems such as the low efficiency, the high side lobes levels and the phase errors (which eventually results in some distortion in the radiation pattern).

This dissertation presents a solution that combines the BFN and the antenna into one structure. The proposed antenna is planar and fully dielectric (all-silicon). The radiation mechanism is based on the dielectric grating. The antenna has been designed in the vehicular radar band (77GHz); however, the proposed idea is also applicable for higher frequencies where the dielectric antennas are the best candidates.

### 3.2.1 First Configuration: Twelve Beams Annular Grating Antenna

This section presents a new idea for a twelve beams, all-Silicon (HRS) mmWave antenna. The whole structure is (as shown in Fig. 3.15) planar and the radiation mechanism is based on dielectric grating. This structure significantly simplifies the integration which is

crucial for mmWave systems.

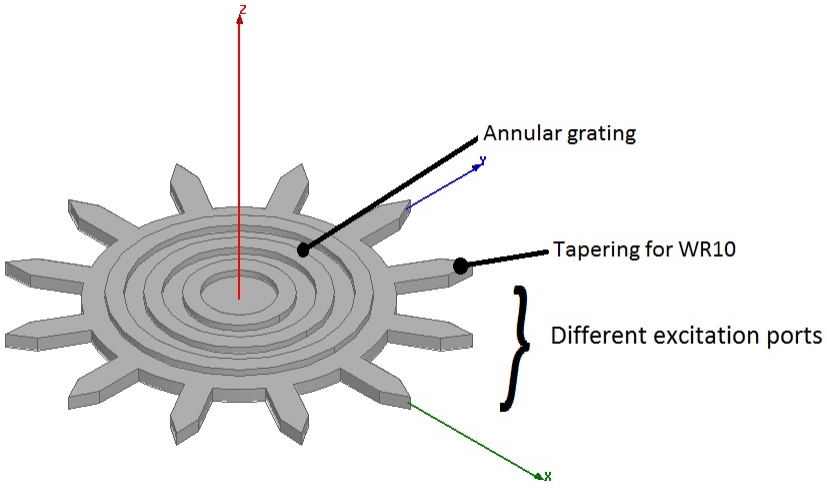


Figure 3.15: Proposed twelve-beams dielectric grating antenna

The proposed structure consists of a disk with an annular dielectric top grating. The cross section of these top grating grooves is rectangular to simplify the fabrication and the analysis. The antenna has a full symmetry about the z-axis. This symmetry is essential for full range scanning, as the beam angle should (intuitively) depend only on the location of the excitation port. For each port, the feeding structure is a simple rectangular DWG. Tapering is used to match the DWG to the WR10 waveguide interface used for testing[2].

### Design Optimization: A- Optimization Objectives

The first step in the optimization problem is to set the optimization objective(s). Since high efficiency requirement is already guaranteed by using high resistivity Silicon, we have set the optimization objective to only maximize the realized gain (the realized gain takes into consideration both the antenna efficiency and the mismatch loss) and to minimize the side lobes level.

[2]Details about the transition are available in Chapter 5.

**Design Optimization: B- Optimization Parameters**

The second step is to define the optimization parameters. In our case, the design parameters are simply related to the antenna geometry, the frequency and the material (the dielectric constant and the loss tangent). The dielectric constant ($\epsilon_r$) and the operating frequency should be considered as the given parameters. However, a very quick test has been conducted to obtain a better understanding of their effect on the given problem. According to [44], we expect that they will significantly affect the beam angle as it strongly depends on $k_0$ and $\beta$ in the circular grating based radiation. A quick simulation is given in Fig. 3.16 to show this effect. For this quick test, the frequency is $77GHz$, the grooves depth is half of the Silicon wafer thickness ($\frac{0.5mm}{2}$), the grating profile is $0.98mm$ in width with a $1.3mm$ period. An image waveguide design with a big ground plane under the antenna has been used (this practice is mostly used to eliminate the downward beam. It also simplifies the fabrication and testing).

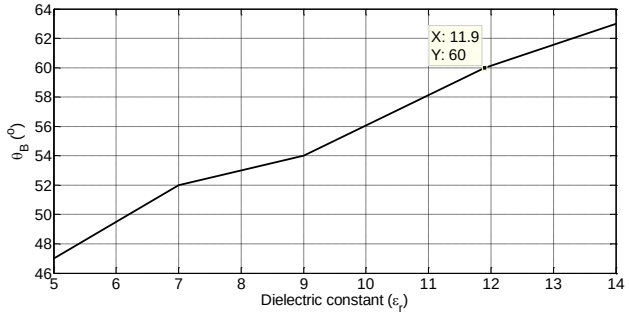


Figure 3.16: Effect of $\epsilon_r$ on the beam direction.

For simplicity, the antenna size will be excluded from the optimization problem. This means that the disk radius will be kept at a fixed arbitrary value ($13mm$). For an aperture efficiency of 1/12 (12 beams), the maximum expected gain from this antenna is 15dB at 77GHz (the aperture efficiency formula is given in Equation 3.5). Then, the remaining parameters are the grating period and the grating depth/thickness. Changing the grating period, as shown in Fig .3.17, affects the antenna gain.

Similarly, changing the grating thickness affects the gain too without having a significant effect on the beam angle. Fig. 3.18 suggests that the maximum gain is $14dB$ which has been found at a grating profile with a thickness of $1.7mm$ and a $2.4mm$ periodicity.

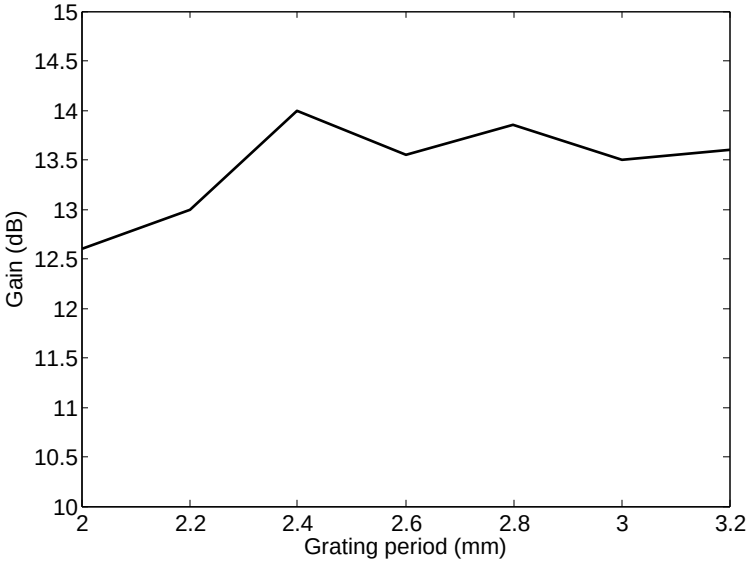


Figure 3.17: Changing the grating period (d) slightly changes the gain and has no effect on beam angle

We have defined an optimization problem where the optimization objective is, as mentioned earlier, to maximize the gain (the goal is $14dB$) and to minimize the side lobes ($\leq -10dB$). The parameters to be optimized are the grating width and the grating period. The initial design parameters used are the ones corresponding to the maximum gain grating profile found earlier by a simple sweep (thickness of $1.7mm$ and periodicity of $2.4mm$). The optimized grating has been found to have a period of $1.3mm$ and a width of $0.98mm$. We have used Genetic Algorithm [36] optimization technique to solve this problem. The GA converged (less than 5% criterion) within the first 500 generations. The used algorithm has the following settings (based on some preliminary trials):

- Real encoding for the population,
- The selection criterion used is the survival of the fittest,
- The mutation rate is 1%,
- Simulated binary crossover is used for mating,

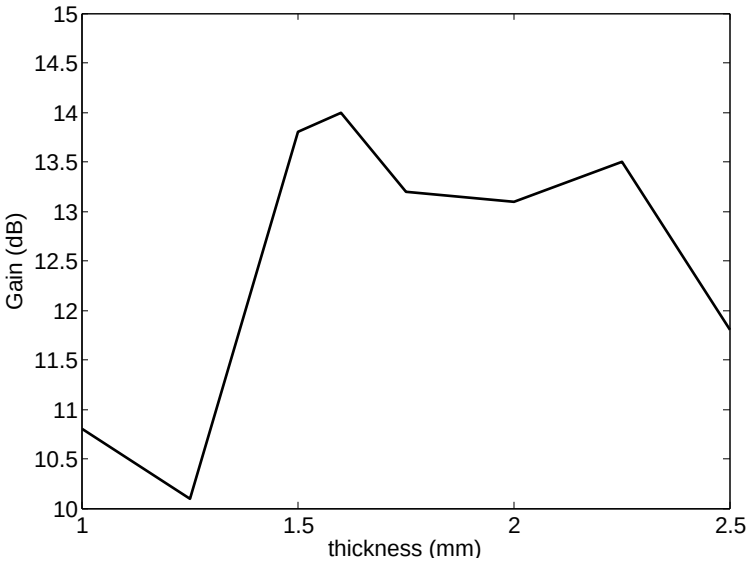


Figure 3.18: Changing grating thickness for a fixed period of 2.4mm

- Number of generations is 500 each with a population of 30 individuals.

**Simulation Results**

Fig. 3.2.1 shows the radiation pattern for the $\phi = 0°$ excitation. The gain pattern shifts when the excitation port changes. Fig. 3.20 shows the gain pattern (in dB) versus the $\phi$ for the angle of the main beam centered at $\theta_B = 60°$. As it can be noticed, the patterns are identical shifted copies from each other. The antenna simulated reflection has been less than $-18dB$ thanks to the tapered WR10 to dielectric image guide transition[3].

### 3.2.2 Second Configuration: Five Beams Annular Grating Antenna

The size of the aforementioned design is relatively big; therefore, we present a more compact version of the antenna with five ports only. Fig. 3.21 shows the proposed five-beam

[3]Details about the transition will be described in Chapter 5.

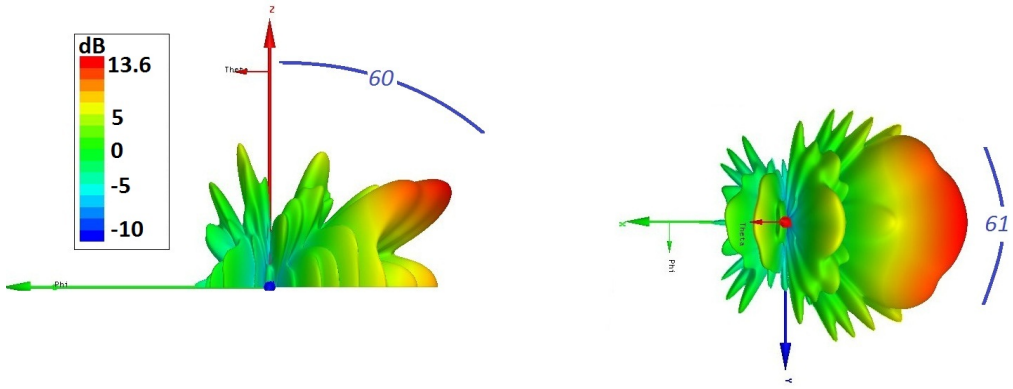


(a) Elevation (b) Azimuth

Figure 3.19: Shows the radiation pattern for $\phi = 0°$ excitation

dielectric grating antenna. This configuration parameters are the same as the first configuration except that we have an additional optimization objective which is to ensure that the five beams are similar (with a gain difference less than $0.5dB$). This slight beam variability came from the fact that the antenna now is no longer symmetric. The optimized grating pattern has been found to have a period of $3.19mm$ and width of $1.7mm$.

Similar to Design 1, by switching the excitation/receiving port we steer the azimuth angle $\phi$ of the beam keeping the elevation one $\theta$ fixed (in the proposed design it was set to $\sim 60°$). The following are the simulation results for this antenna.

### Simulation Results

As shown in Fig. 3.22, the gain pattern shifts when switching the input port. This figure shows the linear gain pattern versus the $\phi$ (at the angle of the main beam $\theta$=60 °). The results show that the patterns are slightly different (the change is less than $0.5dB$). This change is because the structure is not fully symmetrical as only half of the disk has been used.

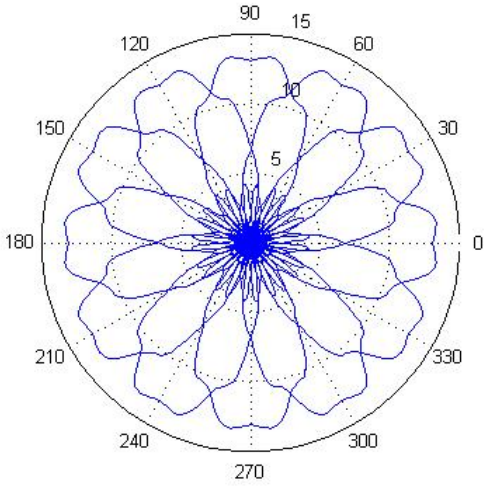


Figure 3.20: Polar plot for the gain (dB) for different ports vs $\phi(\theta_B = 60°)$

### 3.2.3 Fabrication

A two-mask fabrication process has been developed and used. The substrate is a high resistivity Silicon [1 0 0] with a dielectric constant ($\epsilon_r$) of 11.9 and a resistivity ($\rho$) of $3.2K\Omega cm$. The used Silicon wafer has a diameter of $10cm$ and a thickness of $500\mu m$. The fabrication process steps have been developed/optimized in the nanoFAB at the University of Alberta and in the Quantum NanoFab at the University of Waterloo. The process steps can be summarized as follows:

**Process**

(a) Piranha Cleaning (see Fig. 3.23(a))

- Prepare $H_2SO_4 : H_2O_2 \Rrightarrow 3 : 1$
- Immerse the silicon wafer for 15minutes

(b) Sputtering Al 0.5microns at each side

(c) Coating with thin photo resist $\backsim$ 1.25microns

- Use HPR 504,Pour 5-10mL

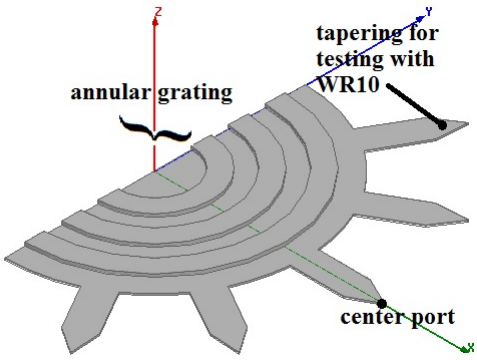


Figure 3.21: shows the uniform Multi-Beam Dielectric Grating Antenna (MB DGA): configuration 2.

- Spread 10 seconds at 500RPM
- Spin 40 seconds at 4000RPM
- Use the hotplate set to $115°C$ for 90 seconds
- After soft baking the wafers, they must be rehydrated for approximately 15min

(d) Litho and patterning the PR with mask 1

- The optimum exposure time is typically between 2-3 seconds
- The developer used is 354. The resist should develop in approximately 15-20seconds.

(e) Patterning the Al

- Al wet etchant $\sim$ 60 seconds

(f) Coating with thick photo resist $\backsim$ 12.5microns

- Use AZ4620, pour 5-10mL
- Spread 10 seconds at 500RPM
- Spin 25 seconds at 2000RPM
- Use the hotplate Set to $100^oC$ for 90 seconds
- After softbaking of wafers, place in a box with a damp cleanroom wipe, close, and leave for 2 hours.

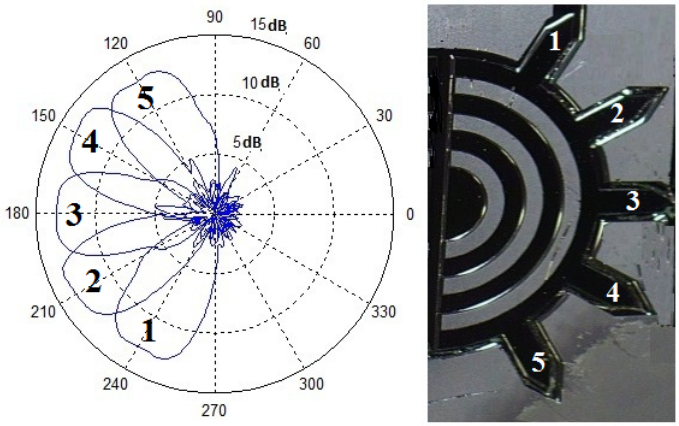


Figure 3.22: Polar plot for the five-beams gain (dB) for different ports vs $\phi(\theta_B = 60°)$

- After the hydration period, the wafers are ready to be exposed.

(g) Litho and patterning the PR with mask 2

- The exposure is 730 mJ (12 sec)
- The developer used is diluted AZ400K developer, the resist should develop in approximately 1 minute.

(h) Deep RIE for a thickness of $l_1$

- Standard Bosch process.

(i) Stripping the PR mask

(j) Deep RIE for a thickness of $l_2$

- Standard Bosch process.

(k) Stripping the Al mask with wet etching

(l) Dicing

The Coventor model is shown in figure 3.24

The sample of the fabricated antenna is shown in Fig. 3.25

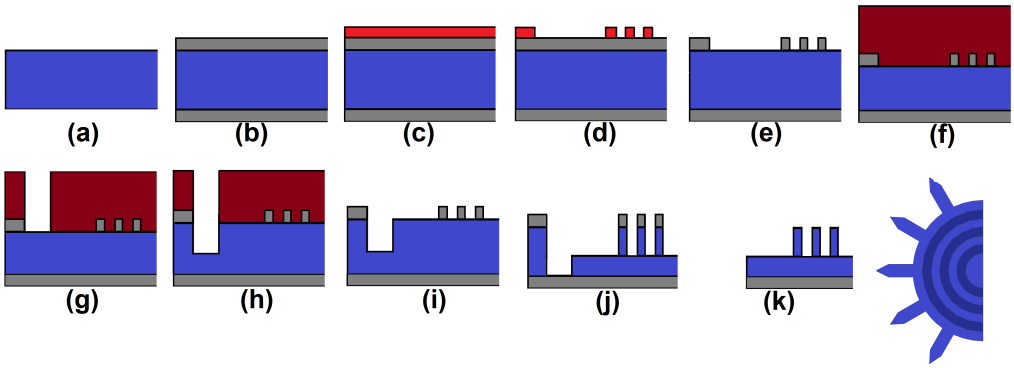


Figure 3.23: Process flow: Each step is illustrated in the process list

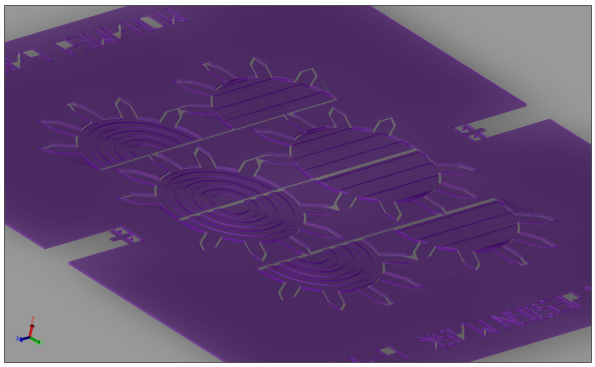

Figure 3.24: The 3D model developed by Coventor tool.

### 3.2.4 Measurement Results

A quick test has been conducted for the fabricated antenna to verify the design. Two test setups in the CIARS (Centre for Intelligent Antenna and Radio Systems) lab at the University of Waterloo have been used, one for measuring the magnitude of reflection coefficient ($|S_{11}|$) and the other for measuring the radiation pattern.

- $S_{11}$ measurement setup (see Fig. 3.26):
  - AUT,
  - PNAX and W-band mixer,
- Radiation pattern measurement setup (see Fig. 3.27):

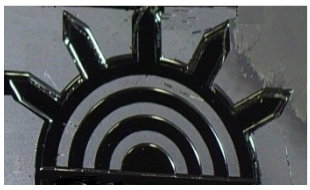

Figure 3.25: Fabricated MB DGA.

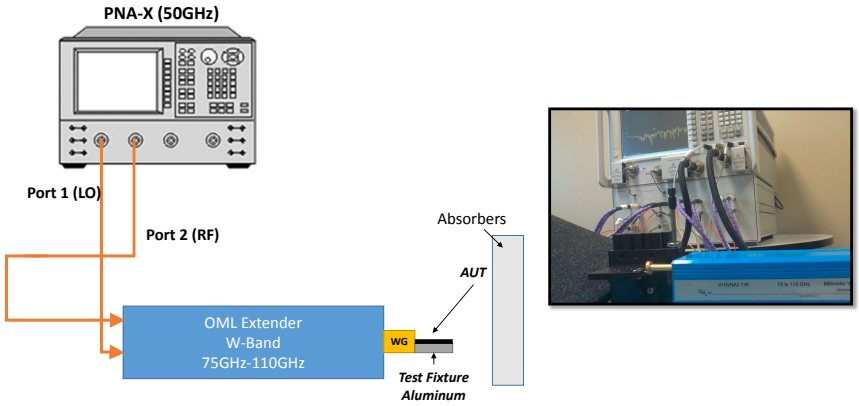


Figure 3.26: $S_{11}$ measurement setup.

- AUT,
- Standard WR10 horn antenna,
- Signal generator and harmonics mixer for WR10,
- Spectrum Analyzer and passive mixer for WR10,

The test has been done for the antenna excited from the center port. Ideally, the other ports should be terminated but since the coupling between ports is always less than $-20dB$, the reflected power from the open termination can be neglected. This makes the measurement setup simple. The measured and the simulated radiation patterns have good agreement as shown in Fig. 3.28. Fig. 3.29 shows the matching measurement. The measurement has more reflection than the simulation. This may be attributed to the imperfect alignment; yet, the antenna is well-matched across the band from $75GHz$ to

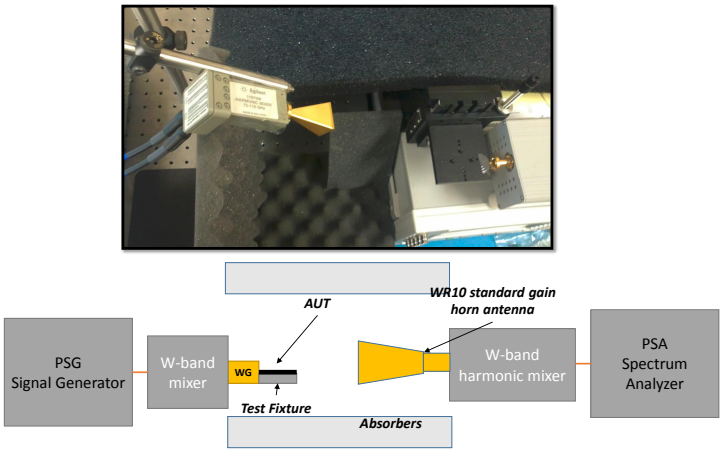


Figure 3.27: Radiation pattern measurement setup.

$80GHz$.

The dielectric grating antenna has a high efficiency of 91%(simulated value). The antenna is capable of generating five beams at $77GHz$ with a $5GHz$ radiation (with less than $1dB$ variations in the pattern) and matching bandwidth. The most popular competitive design at this frequency range is the Rotman lens approach[53]. Compared to this approach, the presented multi-beam antenna has the following advantages;

- No need for the integration between the Beam Forming Network and the Antennas; because the antenna is naturally integrated to the feed network which makes the design much simpler.
- Due to the symmetry of the structure, the phase errors are minimal and hence no gain/pattern variabilities between beams.
- No wasted power in the dummy ports; simply because we don't have ones.
- The proposed structure is fully dielectric hence it has higher efficiency and better chance for scalability to higher frequency range.
- The isolation between ports is better than -20dB which makes the testing much easier (No need for termination).

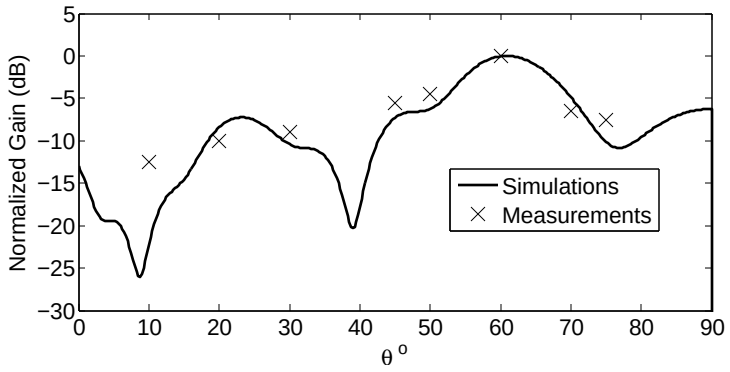


Figure 3.28: Measured and simulated radiation (gain) patterns.

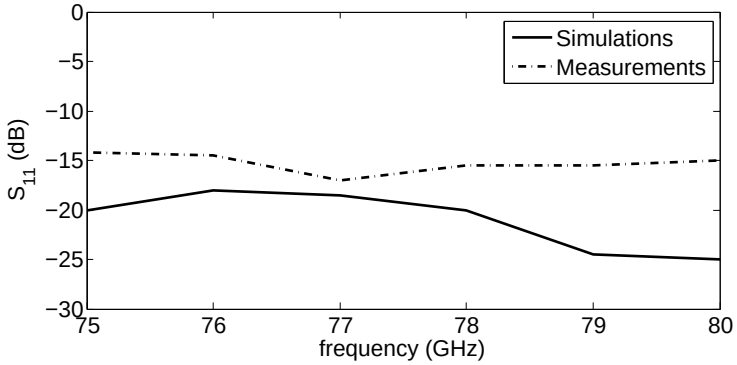


Figure 3.29: Measured and simulated $|S_{11}|$.

On the other hand, there are some Rotman lens designs (that use multi-layer implementations) which have slightly more compact dimensions. However, for the automotive radar application, the size of the presented design ($2.6cm \times 1.3cm$) is totally accepted.

Another classical approach for beam-switching is using Luneberg lens [82], few designs have been reported in the millimeter-wave band [39]. However, a low cost planar implementation is yet challenging. This is mainly due to the Lunebergs law which requires inhomogeneous dielectric constant. This is usually simulated by complex or non-planar designs.

## 3.3 Novel DWG-based Pixelated Antenna

In this Section, a new approach for designing a single-mask antenna for mmWave/sub-THz applications is presented. Since, the antenna space is critical to almost all mmWave applications, the available antenna space should be optimally used to serve the required application. Wireless mmWave devices targeting consumer electronics market are examples for applications with restricted antenna sizes. In such applications, the whole transceiver, including the antenna, has to fit in a very compact area (approximately 1-2 $cm^2$). Similar restrictions exist in automotive radar industry. In addition, generally speaking, smaller mmWave antenna structures have less conductor and dielectric loss.

We have developed a method using Genetic Algorithm [61] to optimize the shape of the antenna in a given allocated space for certain performance metrics. In [62], some theoretical performance limitations for planar antennas are investigated. In our proposed approach, the practical performance bounds for dielectric antennas are explored. Although the proposed method is not supported with theoretical derivations, it offers a fast approach to flexibly engineer the shape of the mmWave dielectric-based antenna for the given specifications/requirements. Since the optimization algorithm takes into consideration both near field (while optimizing the matching) and far field (while optimizing the radiation pattern) simultaneously, the resultant antenna shape would look irregular and complex.

The building block of the dielectric pixelated antenna is the dielectric pixel which, for the proposed antenna, is a high resistivity Silicon cube of $\lambda/2$, which is $0.5mm$ in Silicon at $77GHz$. Higher resolution (smaller pixel/cube size) is expected to results in better performance to some extent. Based on some initial gain requirement (15dBi at 77GHz), the proposed antenna has been chosen to have 10×20 pixels (or $5 \times 10\ mm^2$). Fig. 3.30 shows the allocated space for the proposed antenna.

For this particular example, there are $2^{20\times10} = 1.6\times10^{60}$ different designs that can be realized by different combinations of pixels allocation. Only specific combination of pixels would result in a design which meets the required performance objectives. Such design can be found by applying binary variable optimization techniques. The Genetic Algorithm (GA) is known to be efficient in achieving the global optimum with less sensitivity to the initial condition [3]. GA is also suitable for the problems with a high number of unknowns, and, hence, it is suitable for this problem. The optimization parameters are the binary elements of the 10×20 matrix, representing the existence/absence of the dielectric pixels.

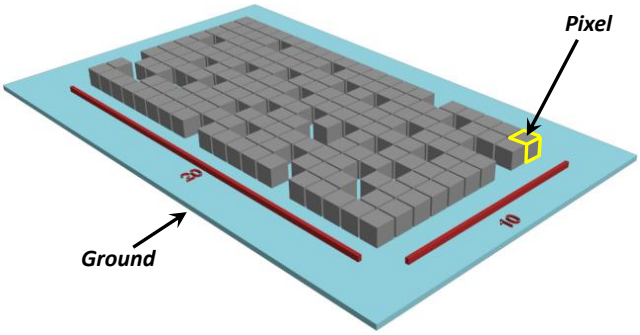


Figure 3.30: The general schematic of a pixelated antenna.

For the proposed antenna, we have used HFSS solver along with the MATLAB built-in Binary Genetic Algorithm optimizer. Based on some preliminary tests, the setting of the GA has been set as follows based on some preliminary tests;

- Population Size = 20
- Maximum number of generations = 200
- Elite Group Size/Migration = 20%
- Cross-over Group Size =80%
- Mutation Group Size =1%
- Cross-over Type = Scattered
- Mutation Type = Uniform

As shown in Fig. 3.31, the user starts with defining the antenna allocated space as well as the required pixels resolution. Then the user defines the optimization objective which could be defined at a single frequency or over a range of frequencies. For example, the optimization objective can be the minimization of the magnitude of $S_{11}$ at 100GHz. Then, the user defines the GA settings (as previously explained) before he runs the optimizer.

The GA optimizer starts with a random population of individuals. This is the initial population (the first generation). The number of individuals (the population size) is 20. Each individual is essentially a binary string of 200 bits. For each individual, HFSS is called

with the corresponding antenna configuration. After the full-wave problem is solved, the cost function is calculate and stored in a log file. Since the HFSS simulation is very time consuming, before the HFSS is called, the scripts searches the log file history and if the design values matches a record that has been already simulated, it updates the cost function without executing the HFSS solve command. This process is done for each individual in the generation before sorting based on the objective function is performed then a new set of individuals is created (Next generation). The next generation is formed based on three elements, namely;

1. Elite group: This is the top 10% individuals from the previous generation. They are kept without changing for the new generation.
2. Cross-over: This is a group generated by uniformly swapping parts of the binary string between two individuals from the previous generation.
3. Mutation: This is randomly generated individuals in the new generation to prevent fast stagnation.

### 3.3.1 Example 1: Pixelated antenna optimized for maximum gain

The relation between the gain of an aperture antenna and the physical area is governed by Equation 3.5. The aperture efficiency is a dimensionless parameter with a maximum value of 1.0. However it is practically impossible to achieve this value since all the antennas have losses. These losses include power dissipation, non-uniform illumination, and edge diffraction. An estimate of the practical values of the aperture efficiency, for some recently reported antennas in the V-band, is shown in Table 3.1. It can be observed that the simplest approach to obtain better aperture efficiency is to have higher number of elements which is not feasible for applications with restrictions on the antenna size. For smaller aperture size, optimal configuration of elements and their excitation should be optimized for maximum gain. In the pixelated antenna concept presented here the feed structure and the configuration of the antenna elements are optimized at the same time.

$$Gain = \eta_{aperture} \frac{4\pi A_{physical}}{\lambda^2} \tag{3.5}$$

Table 3.1: Different designs at 60 GHz.

| **Design** | **Size ($\lambda_0$)** | **Gain (dB)** | $\eta_{aperture}$ |
|---|---|---|---|
| Horn-type PCB Antenna [24] | 0.9×2.2 | 8 | 25% |
| Dielectric Tapered Antenna [42] | 2.2×2 | 13 | 37% |
| SIW fed Cavity Array Antenna [85] | 13.4×13.4 | 33 | 89% |

In this example, the optimization objective is to simply maximize the gain at 77 GHz. This also includes obtaining a matched design (-10dB). The convergence plot is shown in Fig. 3.32. It shows the cost function (which is the antenna gain in this example) versus the generation index. The optimal value of 29 has been achieved within the 200 generations. From computational point of view, one can think that the design costs 40000 HFSS simulations (200 generations × 20 individual at each generations). However, this is not correct since the elite group are kept for each generation (no re-simulation). In addition, for this binary type of variables, some values are statistically repeated many times during the optimization search. These values are calculated once and stored. The average total run time for this example of optimization process (including the HFSS simulation) is approximately 8 hours on a 4 core machine.

The 3D model of the optimal design is given in Fig. 3.33. The feed structure is a Silicon image waveguide with the same thickness as that of the antenna ($500\mu m$). This leads to a smooth transition and lower fabrication cost. The Silicon image guide has a tapered input section that works as a matching transition to the metallic waveguide (WR10) port of the PNA-X millimeter-wave extender. The field distribution is shown in Fig. 3.34. By carefully examining the plot, we will notice that effectively half of the structure is contributing to the radiation. Hence, the optimized compact structure can be only 5 × 5 $mm^2$. This is another advantage of this algorithm. The radiation pattern is shown in Fig. 3.35. The achieved gain is 14.6dB. By simulating half of the structure, the achieved gain is also 14.6dB.

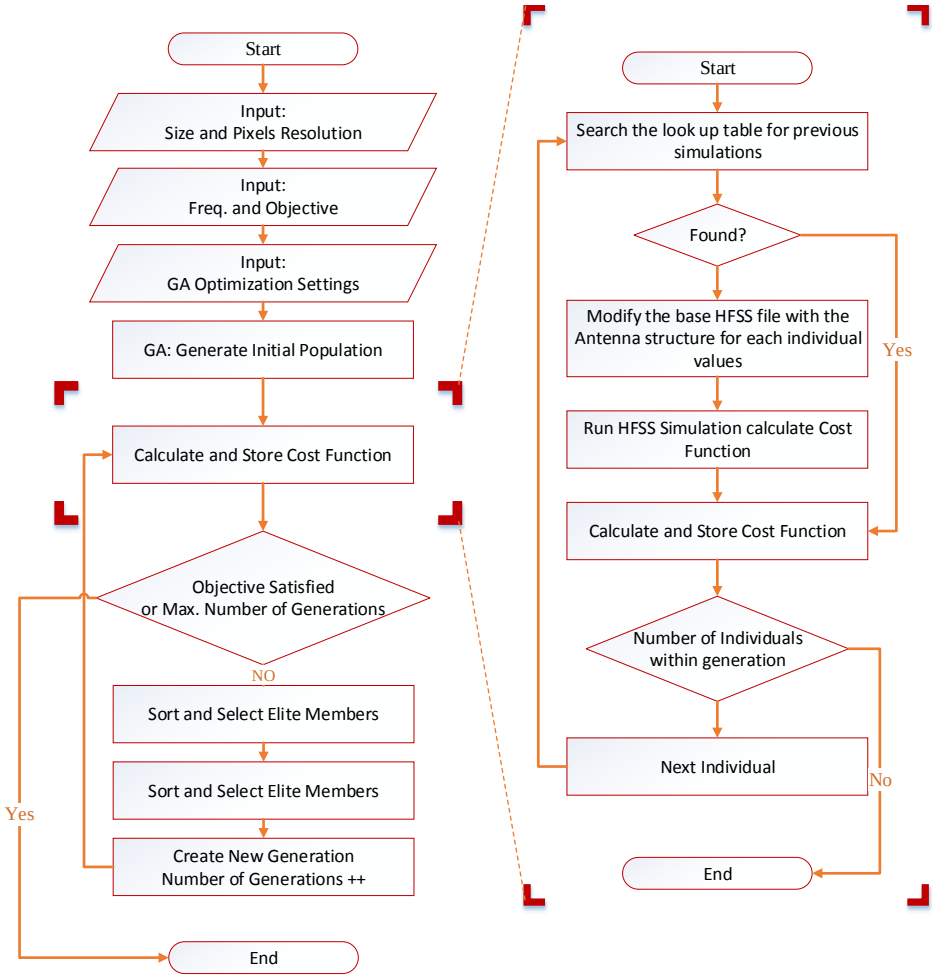


Figure 3.31: Flow chart of the proposed antenna design method.

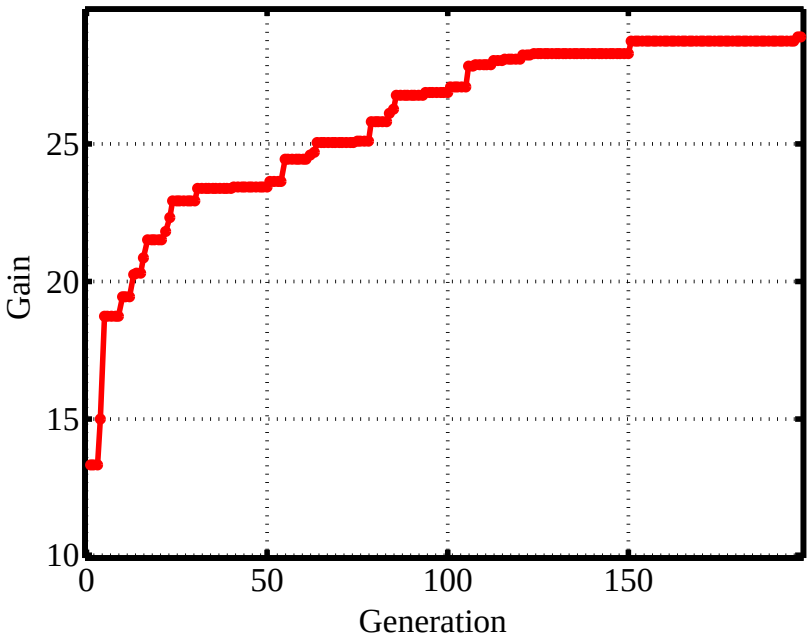


Figure 3.32: Convergence plot for Example 1.

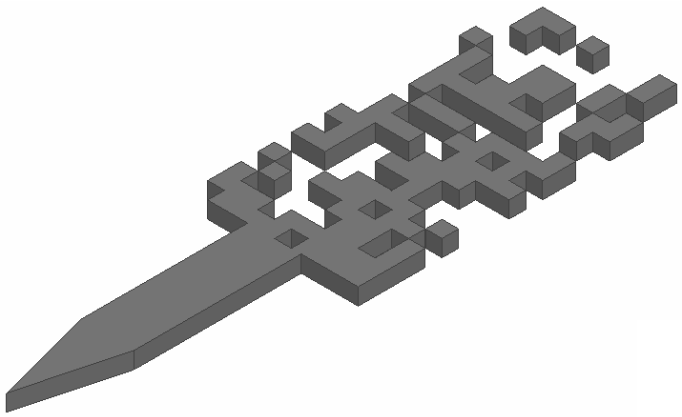

Figure 3.33: 3D model of the optimal design of Example 1.

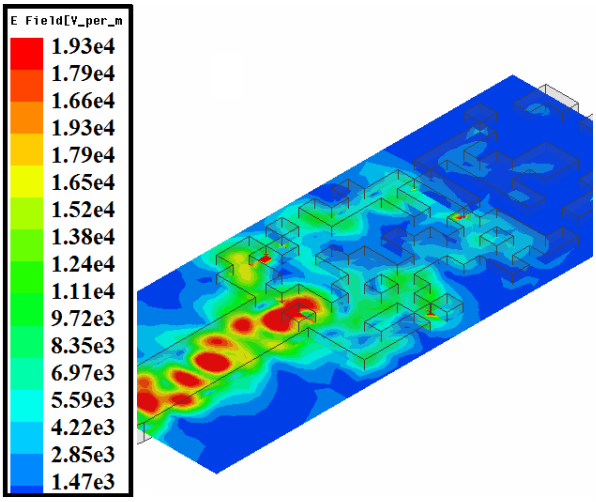


Figure 3.34: E field distribution of Example 1.

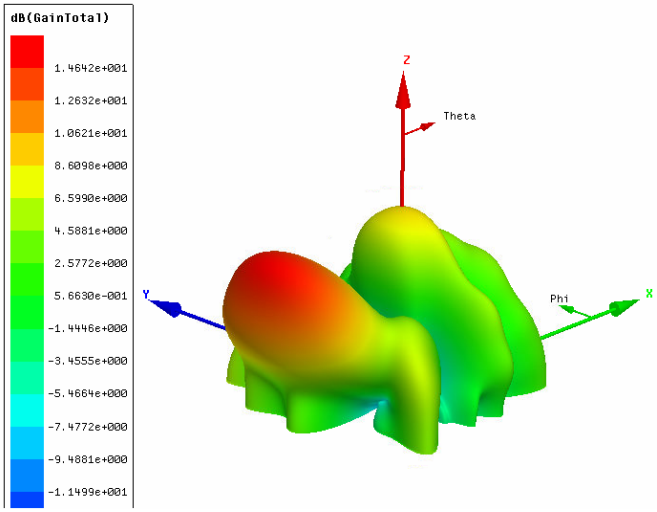


Figure 3.35: Gain pattern of Example 1.

### 3.3.2 Example 2: Pixelated antenna with multiple optimization objectives

In this example, the optimization objectives are more complex. The optimization objectives along with the optimal values are given in Table 3.2. The cost function for these objectives is shown in Equation 3.6. As can be seen, the values were represented in linear scale instead of logarithmic (dB) scale. This scale has been found to be better in the optimization process. Since the dB scale is less sensitive to small variations, it causes the optimization process to saturate quickly.

Table 3.2: Cost Function at 77 GHz.

| **Parameter** | **Objective** | **Optimal Value** | **Measured Value** |
|---|---|---|---|
| $S_{11}$ | -15dB | -9.1dB | -12.6dB |
| **Gain** | 15dB | 13.0dB | NA |
| **Beam Angle** | $25^o$ | $27^o$ | $25^o$ |

$$Cost = -[32 - Mag(Gain(\theta = 20^o, \phi = 180^o)) + 100 \times (0.17 - Mag(S_{11}))] \quad (3.6)$$

The GA optimization process has been performed for a single frequency (77 GHz) and converged within the first 50 generations/populations. The 3D model of the optimal design is given in Fig. 3.36.

As can be seen in Fig. 3.37, the fabricated antenna includes, unlike the model shown in Fig. 3.36, 15$\mu$m beams grid to mechanically support the antenna and keep the disconnected pixels in their specified positions. The effect of these beams is a slight shift in the frequency response. The antenna has been fabricated and tested. A single-mask dry etching process has been developed and used. Fig. 3.38 shows the reflection coefficient of the proposed antenna. The $S_{11}$ measurement has been conducted using Agilent PNA-X (N5242) attached to W-band OML extenders. A simple WR10 to DIG tapered transition is used.

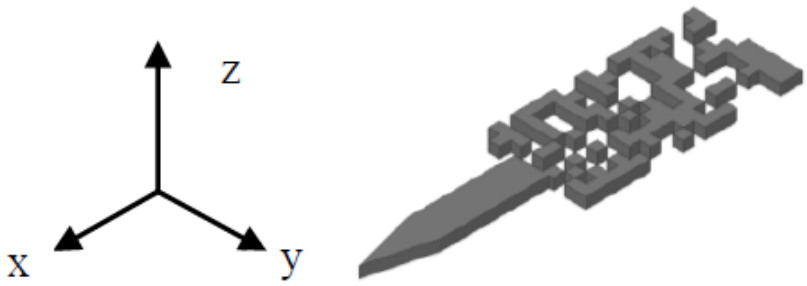


Figure 3.36: 3D model of the optimized antenna.

Figure 3.37: Fabricated pixelated antenna sample.

The antenna radiation pattern has been measured using CIARS NSI planar near field scanning system[4]. The measured and simulated E plane patterns at 77 GHz are shown in Fig. 3.39. Some ripples in the measurement pattern are mainly due to a small air gap (50-100$\mu m$) between the antenna and the test fixture (due to assembly). Fig. 3.40 shows the revised simulation after including the air gap effect as well as the finite ground.

[4]http://ww2.nearfield.com/Sales/300Vscanners.htm

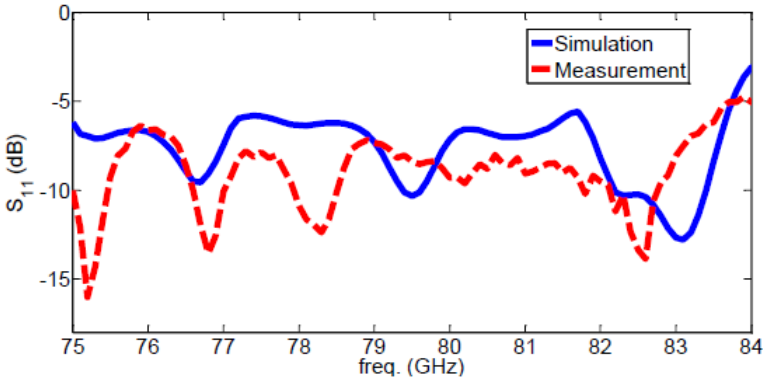


Figure 3.38: $S_{11}$ in dB (simulated and measured).

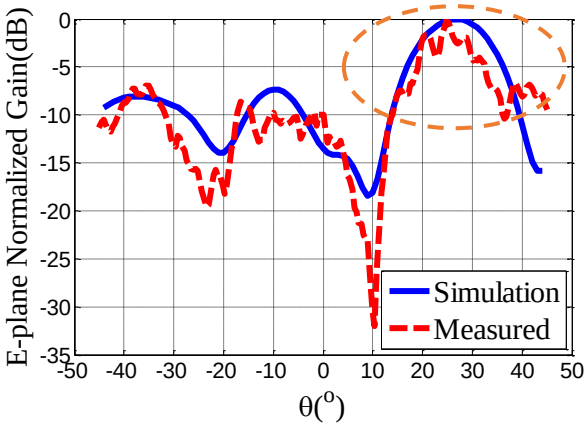


Figure 3.39: E-plane normalized gain (simulated and measured) at 77 GHz.

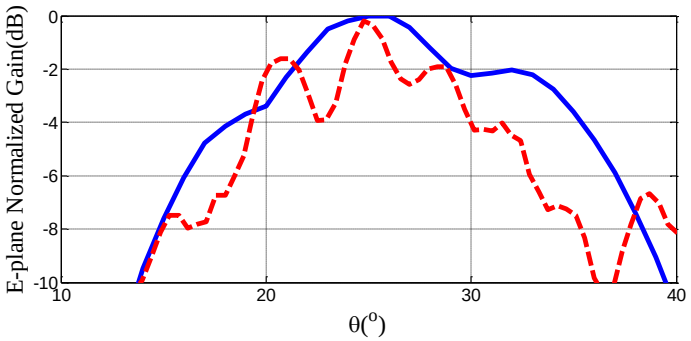


Figure 3.40: Simulated pattern (solid line) after including non-idealities in test fixture. The dotted line shows measured results.

### 3.3.3 Comparison with Tapered Rod (Reference Antenna)

In this sub-Section the pixelated antenna radiation pattern is compared with that of a tapered rod antenna as a reference. The tapered rod antenna is simply a tapered section of the DIG with a length of 10mm. This tapering section makes the structure radiates with small impact on the overall impedance matching. A picture of the tapered antenna is shown in Fig. 3.41. The S-parameters of the tapered antenna is shown in Fig.3.42 while the radiation pattern at 77GHz is shown in Fig. 3.43. The pixelated antenna sample designs of the previous sub-Sections are compared to the reference antenna in Fig. 3.44.

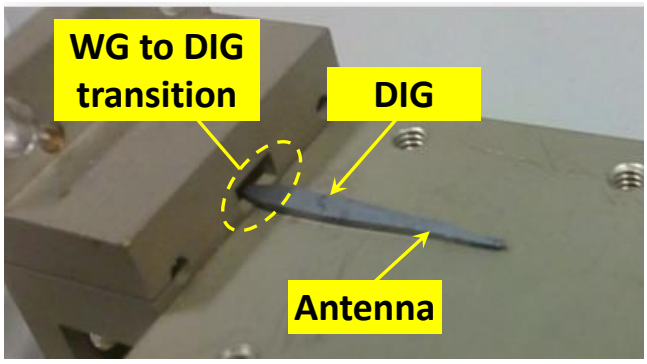


Figure 3.41: Picture of the tapered antenna mounted on the test fixture used for measurements.

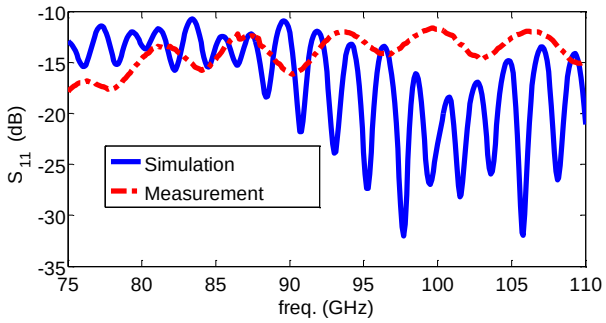


Figure 3.42: Picture of the tapered antenna mounted on the test fixture used for measurements.

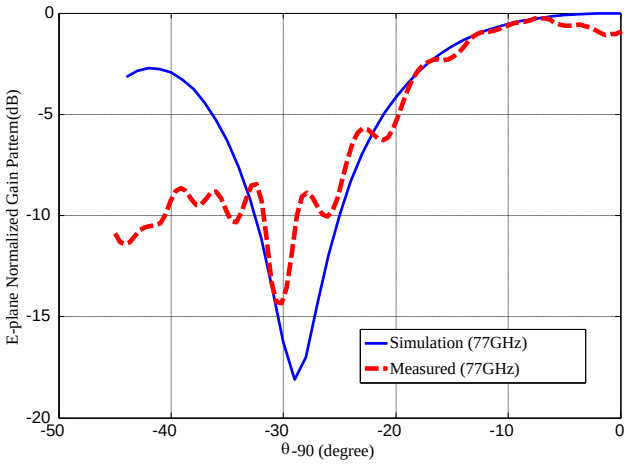


Figure 3.43: Radiation pattern at 77GHz for the reference antenna.

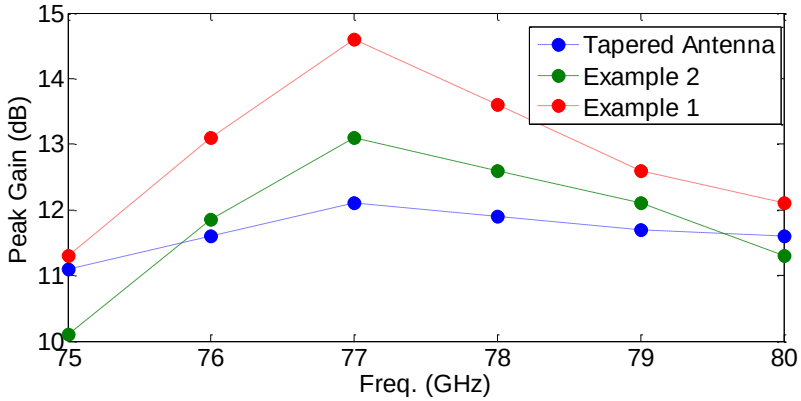


Figure 3.44: Gain comparison between the three examples.

## 3.4 New DWG-based Travelling Wave Antenna

One of the potential antenna candidates that can be easily integrated with the dielectric waveguide is the dielectric grating antenna. The dielectric grating antenna has interesting radiation properties which can be used in beam-steering. In 1D linear grating, changing the grating period directly steers the beam as shown in Equation 3.7.

$$\theta_n = sin^{-1}\left(\frac{\lambda_o}{\lambda_g} + \frac{n\lambda_o}{d}\right), \left|\frac{\lambda_o}{\lambda_g} + \frac{n\lambda_o}{d}\right| \leq 1 \tag{3.7}$$

Where $\theta_n$ is the beam angle, $\lambda_o$ is the wavelength in free space, $\lambda_g$ is the wavelength in the guiding structure, and $d$ is the grating period.

Structures with this type of radiation are usually referred to as leaky wave antennas [20],[12] which are of significant interest for beam-steering applications [65],[68]. In [89], a new dielectric grating antenna for mmWave applications is proposed. The antenna is based on rectangular dielectric image guide with grating on its sides which simplifies the fabrication process and introduces flexibility in the grating profile. The antenna achieves an efficiency of 90% and a gain of $18dB$ at $100GHz$. It provides a frequency scanning capability up to 25°. The proposed structure is a one-dimensional periodic leaky-wave antenna, a structure supporting the propagation of a slow wave which is modulated through the periodic discontinuities. Typically, open structures provide the slow-wave guiding media. This kind of periodic antenna can be beneficial of realizing beam steering from the backward direction to the forward direction since it is capable of supporting both backward and forward waves.

The antenna has been built and tested (see Fig. 3.45). To define the bandwidth of the antenna, reflection coefficient and maximal gain of the antenna is taken into account. These two parameters are shown in Fig. 3.46.

A new CPW-fed dielectric antenna with side grating has also been developed. The CPW to DIG transition details will be described in Chapter 5. The proposed structure is essentially a travelling wave antenna which is highly desirable for high gain and frequency scanning applications. The proposed antenna is operating in the V-band.

The antenna model is shown in Fig. 3.47. The simulated gain versus frequency curve is shown in Fig. 3.48. As can be seen the antenna has a peak gain of 18dBi around 62.5GHz. The 3D gain pattern at this frequency is shown in Fig. 3.49. This type of travelling

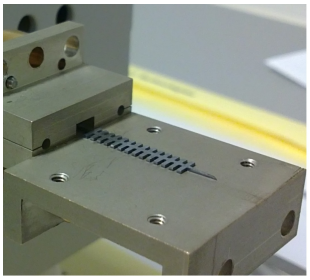

Figure 3.45: Picture of the dielectric side grating antenna [89].

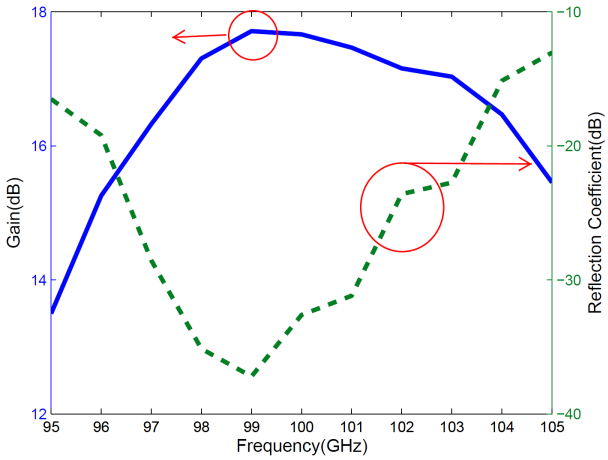


Figure 3.46: Maximum gain and reflection coefficient of rectangular profile over the operating frequency range [89].

wave antenna structure provides frequency scanning feature which can be very useful in applications such as imaging and radar. Fig. 3.50 shows the frequency sweep feature of the proposed antenna.

The proposed antenna has been fabricated and tested. The antenna length is 30mm while the grating period is 2mm. Fig. 5.17 shows a picture of this antenna fed by a CPW line. More details are available in Chapter 5.

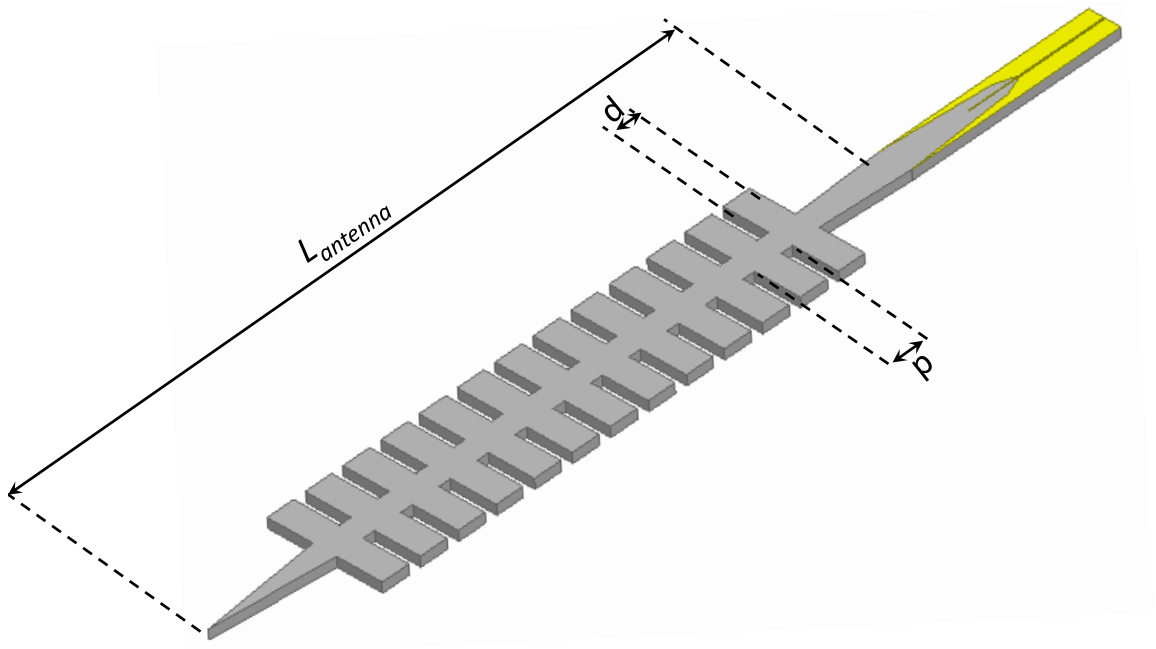


Figure 3.47: 3D model of the proposed CPW-fed side grating antenna.

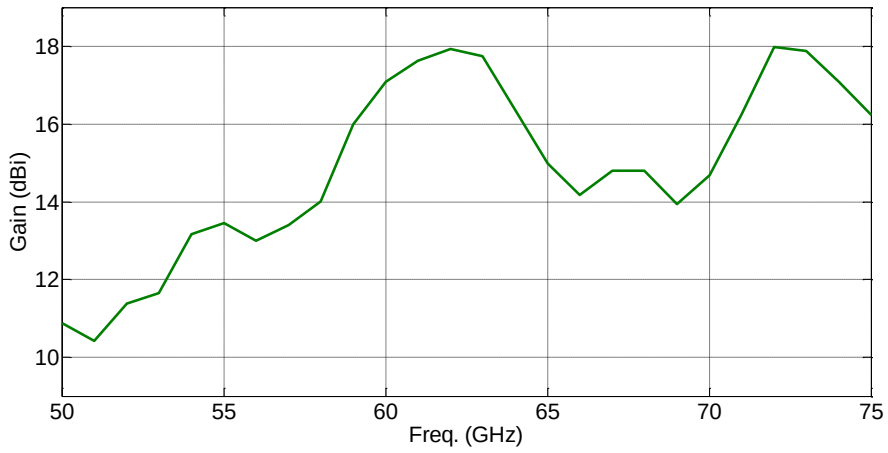


Figure 3.48: The gain frequency response of the proposed antenna.

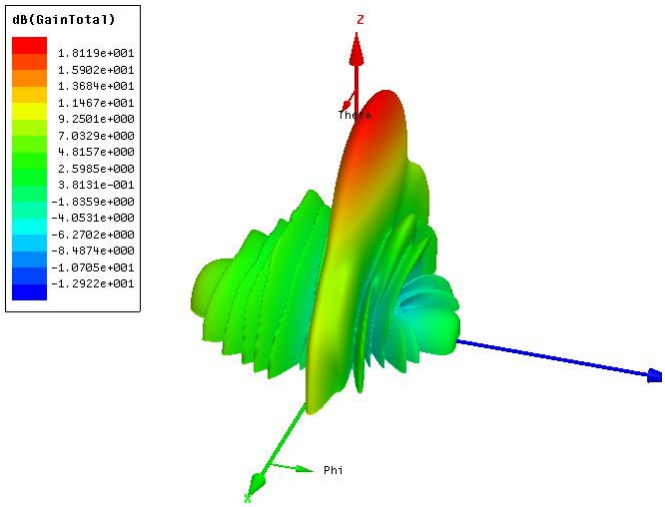


Figure 3.49: Gain pattern of the proposed antenna at 62.5GHz.

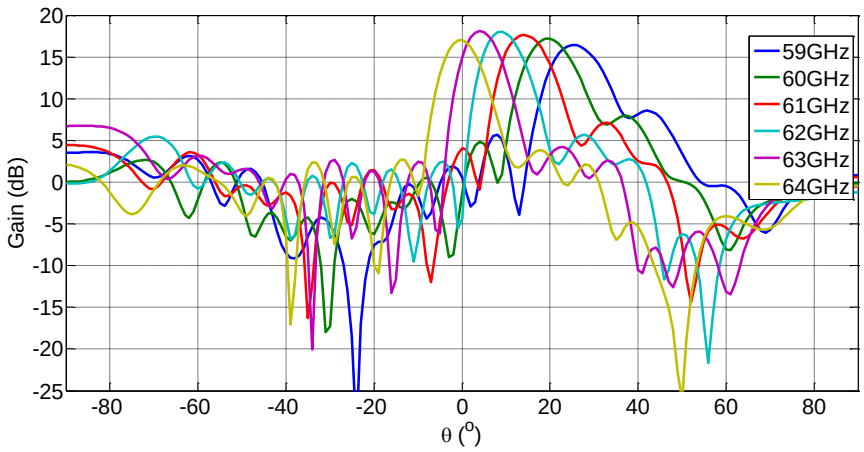


Figure 3.50: E-plane gain pattern for different frequencies.

Figure 3.51: A fabricated sample of the proposed CPW-fed side grating antenna.

# Chapter 4

# Novel HRS DWG-based Phase Shifters

Phased array technology is rapidly advancing due to the emerging mmWave applications which require high resolution beam-steering [72]. Compared to switched beam antenna systems, phased arrays provide more degrees of freedom in beam-steering. However, they are usually more preferable in systems with large number of antennas due to the associated complexity. Phased arrays commonly consist of four building blocks: the active elements, RF manifold (feed network), phase shifters, and antennas. High performance integrated phase shifter is a key component in mmWave phased array systems. Passive phase shifters can significantly reduce the cost in TDD (Time Division Duplex) based phased array transceivers since they are usually bi-directional (phase shifters and antennas can be shared between the transmitter and the receiver). In addition, passive phase shifters generally have lower power consumption compared to their active counterparts.

Low-cost compact integrated phase shifters with low insertion loss and low power consumption are highly desirable for the aforementioned applications. In addition, minimal insertion loss variation for the full range of phase shift over a wide frequency band is a crucial requirement. Various phase shifter technologies have recently been reported [25],[30],[69]. Among them, the ferroelectric phase shifters [25] provide fast tuning speed, high power handling capability, and low power consumption; however, they suffer from high insertion loss variations. Liquid crystal phase shifters [30] are usually not very lossy but they are too slow for phased array applications and suffer from considerable insertion loss variation with phase shift as well as the well-known hysteresis problem. In addition, they are sensitive to temperature variations, which is a significant concern for automotive or outdoor

applications. Low-loss mmWave phase shifter driven by dielectric elastomer actuators has been recently reported [69]. However, this phase shifter is bulky and the control voltage is too high (in the range of kVs) which limits its practical application. Phase shifter based on dielectric loading has also been reported [73]. Although, the performance of this MEMS-based phase shifter [73] is acceptable for some mmWave phased array applications, the size and the high cost are the main limitations.

## 4.1 Phase Shifter Loss Variation Requirement

The phase shifter insertion loss variation effect on antenna pattern is shown in Fig. 4.1 which depicts the array factor of eight elements antenna array with non-uniform excitation for a different phase shifter characteristics (1-ideal phase shifter which has 0dB loss variation, 2- phase shifter with 2dB loss variation, and 3- phase shifter with 6dB loss variation). The antenna array model is shown in Fig. 4.2. The array factor has been calculated based on Equation 4.1.

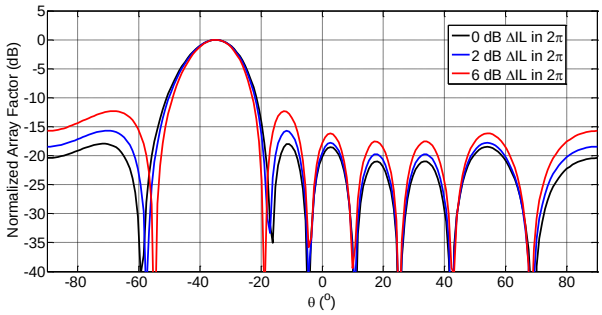


Figure 4.1: The array factor for an eight element non-uniform (linear tapering is used) excited linear antenna array for different phase shifter performances.

$$AF(\theta) = \sum_{i=1}^{8} a_i IL(\phi_i) e^{-j(kx_i sin(\theta)+\phi_i)} \tag{4.1}$$

Where $IL(\phi_i)$ is the insertion loss of the phase shifter for a phase shift $\phi_i$, k is the wave number, $x_i$ is the location of the $i$th antenna element (the antennas are spaced at half

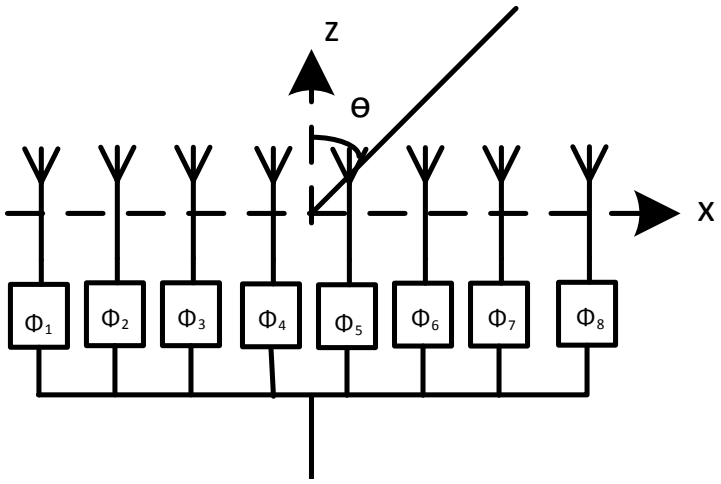


Figure 4.2: The antenna array model used for calculating the array factor.

wavelength) and $a_i$ is the excitation coefficient of antenna element number $i$ (linear amplitude tapering is used to suppress the side lobes).

Fig. 4.3 shows the effect of insertion loss variation on the SLL of an eight elements phased array. Three different array tapering (non-uniform excitation profiles) are shown as well as a uniform array. As can be seen the SLL is strongly dependent on the loss variation value ($\|\Delta IL\|$ is defined as the phase shifter maximum insertion loss variation across all the phase shift values). Phase shifter loss variation also reduces the peak gain.

The insertion loss variation with phase shift is typically compensated in phased array antennas by adding a variable gain amplification/attenuation stage to each phase shifter (as shown in Fig. 4.4). This solution adds to the complexity, cost, power consumption, and the noise level of the phased array antenna system. In this work, we have been investigating an alternative approaches by realizing high performance phase shifters with both minimal average loss and minimal loss variation over the full phase shift range.

In the following Sections, two new phase shifting concepts are presented. Both are based on HRS DWG technology which provides perfect performance at the mmWave/sub-THz range. In addition, it can form a fully homogenous low-cost/low-loss platform suitable for mmWave/sub-THz antenna system that can be easily integrated with active devices

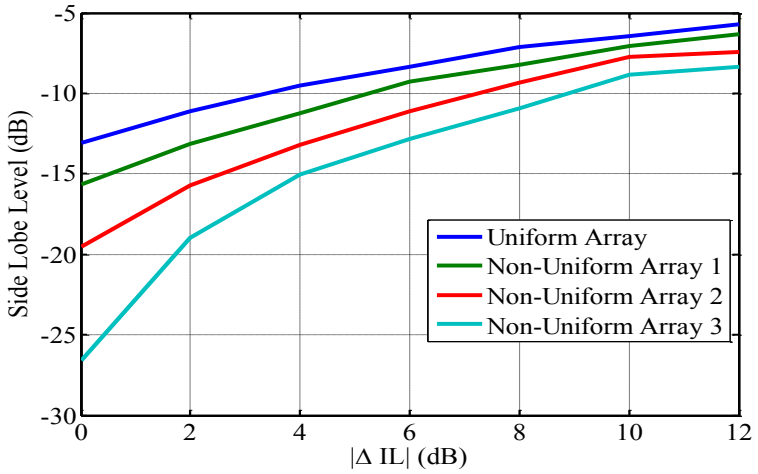


Figure 4.3: The effect of phase shifter insertion loss variation on the side lobe level of eight elements array.

in this range of frequencies [15]. The main difference between the two new phase shifters is the actuation plane; one is vertical while the other is horizontal/lateral. The size and the performance of slightly different which make each one suitable for different applications.

## 4.2 Wiggling Dielectric Waveguide Delay Line/Phase Shifter (WDWG)

This Section introduces a novel modified version of the conventional rectangular cross section dielectric waveguide/image-guide and a new variable phase-shifter/time-delayer structure, which is suitable for phased array antenna applications in mmWave/sub-THz band.

The idea of the proposed structure is based on modifying the signal path physical length. To change the phase shift or the time delay, a part of the dielectric waveguide is cut into small disjoint segments, which can be moved back and forth, causing a variable signal path length. Fig. 4.5 illustrates the proposed idea. A number of movable dielectric blocks (in the particular example shown in Fig. 4.5, this number is 7) lie in the middle

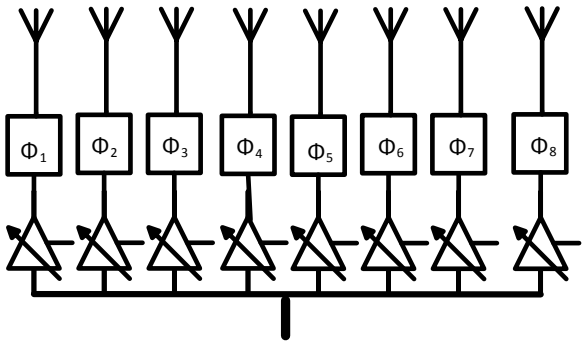


Figure 4.4: A schematic of an eight element transmitter phased array.

of each structure. The rest of the structure is the conventional rectangular cross section dielectric waveguide. Our proposed structure is full Silicon and can be implemented using the deep reactive-ion-etching [59] fabrication process. The proposed design can tolerate less than $1:30$ etching aspect ratio (low cost fabrication process).

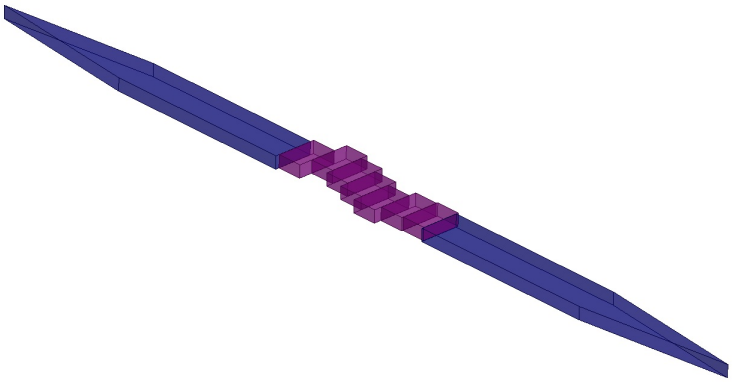

Figure 4.5: Diagram of the proposed phase shifter

Fig. 4.6 shows one particular design that has three free blocks only. This represents the simplest form of the new phase shifter. In the middle of the structure lie three sliding blocks (which can be displaced independently by adding transversal planar displacements), the rest of the structure is the conventional dielectric waveguide with a rectangular cross

section.

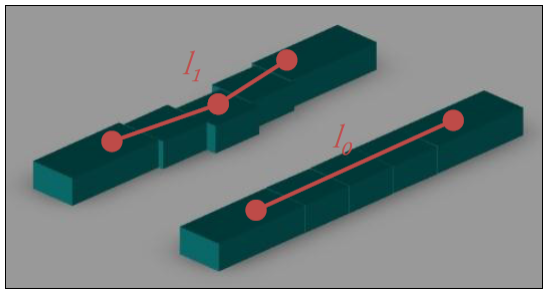


Figure 4.6: Shows three free blocks version of the phase shifter.

Fig. 4.7 shows the field distribution for arbitrarily chosen phase shifts. Interestingly, the EM wave bends to fit in the modified waveguide, these bends lead to an increase in the electrical length, and, hence, the total phase. Also, the larger the shift we achieve, the more the radiation loss we have. This can be noticed from the field plot (note for this design the block length was arbitrary set to be $1.5\lambda$).

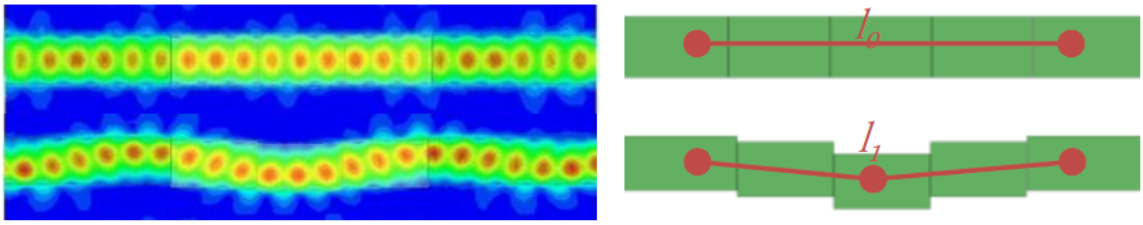


Figure 4.7: Shows field modulation while changing the sliding parts.

### 4.2.1 Simplified Model

Extensive simulations are needed for optimizing the design. This, especially when the number of the free blocks is high, makes the design using full field solver difficult. Therefore, we have developed a simple model to estimate the phase based on a first order fitting for the signal path inside the shifted blocks. In Fig. 4.6, the path difference $(l_1 - l_0)$ has been

calculated for the different block shifts and used to calculate the overall phase shift.

For simplicity, we will verify our model on the three block phase shifter, and for further simplicity, we will assume that the three displacements are dependent, in that the first and the last block should have the same shift, while the displacement of the middle block is 2× shift. These assumptions are for the simplification of the verification step; however, the model generality is still valid. Fig. 4.8 shows a good agreement and verifies the basic idea of relating the phase shift with the transversal displacement.

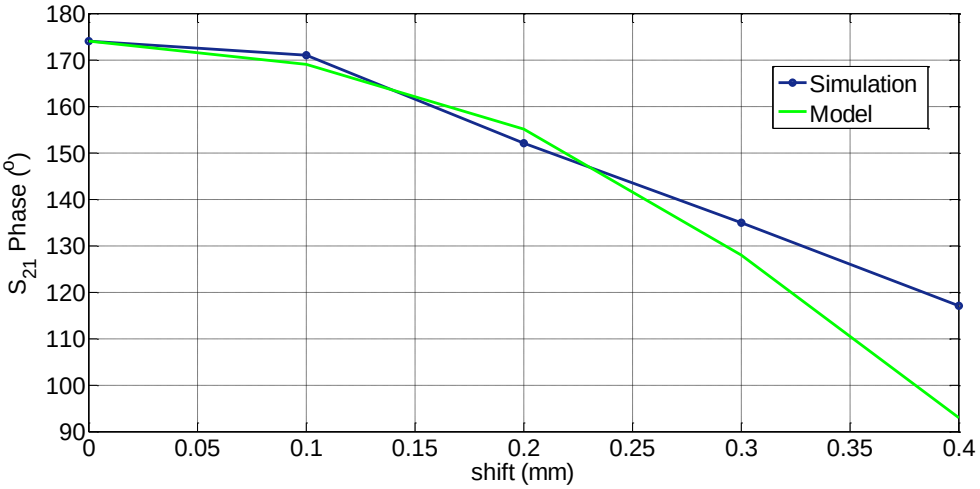


Figure 4.8: Shows the phase shift for both full field simulations and model.

This model is insufficient to estimate the insertion and the return loss; therefore, we have developed a complementary model based on macro-modeling. Macro-modeling uses a divide-and-conquer technique where the given problem is divided into smaller parts, and then those smaller parts are matched to a pre-defined model library. In our case, as shown in Fig. 4.9, the model library is done for a single step with all possible shifts it can take. Then to match a complete structure we simply cascade the $S$ parameters of the individual steps. This library is done by full 3D simulations. Although, the problem was simplified by selecting a single mode of modeling, higher order modes can be easily added if a more accurate model is needed.

Fig. 4.10 shows a good agreement between our model and the full field simulated structure. The average time saved was 50% for the three blocks structure. This is a significant time reduction given that the optimizer needs to simulate 15000 different structures for each phase point.

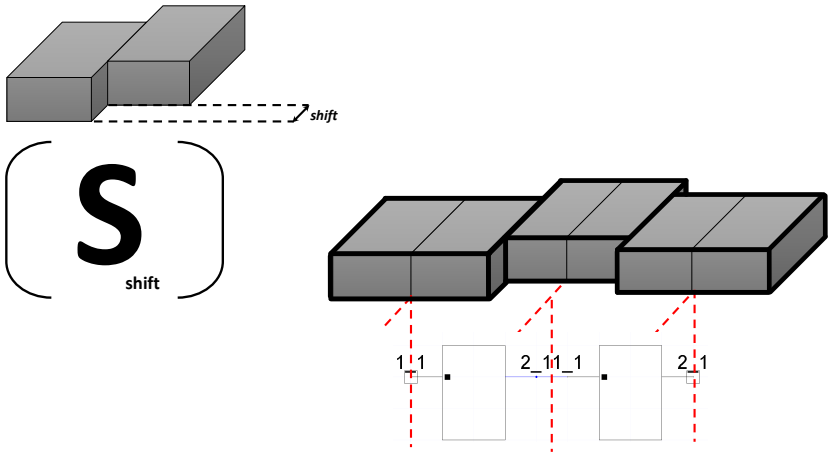


Figure 4.9: Shows the macro-modeling structure.

### 4.2.2 Gap size

Transition gaps are the gaps between the sliding blocks. This gap allows for moving the blocks. The gap size is limited by the fabrication constraints. We are using deep reactive-ion-etching to etch this device and it is expensive to have an aspect ratio higher than 1 to 30. Any perpendicular component of the electric field at the gap interface will cause a high reflection; therefore we had set our propagating mode to be TE polarized.

### 4.2.3 Example 1: Seven blocks 77GHz phase shifter

After presenting the concept, we now present our first design. We have arbitrarily chosen the number of sliding blocks to be seven. It is up to the designer to choose the number of elements he can afford in his design, the more elements you introduce the smoother performance you can achieve, but the layout will get more complex. The design frequency

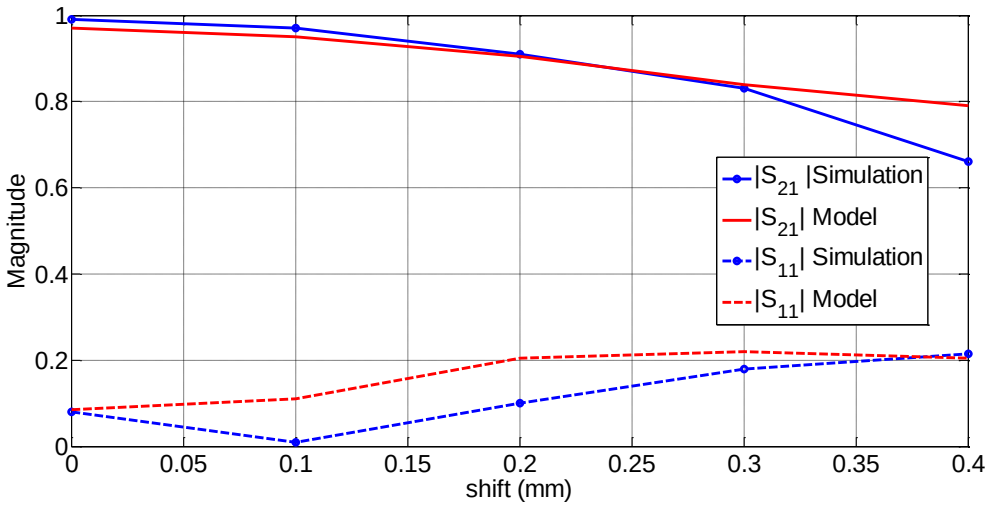


Figure 4.10: Shows the magnitude of S parameters for both full field simulation and cascaded macro-models.

is $77GHz$ and the silicon waveguide ($\epsilon_r = 11.9, tan\delta = 0.005$) has a cross section of 1.6x0.5mm, while each block has a length of $1mm$ ( $\lambda$) and the transitional gap is of $17umm$ (which is $\sim 1/30$ of the $0.5mm$ wafer's thickness).

### Optimization

As introduced earlier, the signal experiences an amount of delay proportional to the physical path length that can be controlled by the proper positioning of the free blocks. Each delay value can be achieved by a variety of configurations of these free blocks; however, we are interested in the configuration that minimizes the losses (radiation and reflection). Therefore, we have defined an optimization problem with the displacements' values for all the sliding blocks as the problem unknowns (see Fig. 4.12) and the optimization objective is to maximize the guided transmission for a given center frequency and phase shift. This optimization will be conducted once in the design phase when the optimal sets are tabulated in a look up table. The actuation controller shall recall these values when phase shift changing is needed.

We have chosen to go with GA as it easily matches the problem. The GA chromosome will be a vector of the different blocks' displacements (genes) and we will use real encoding

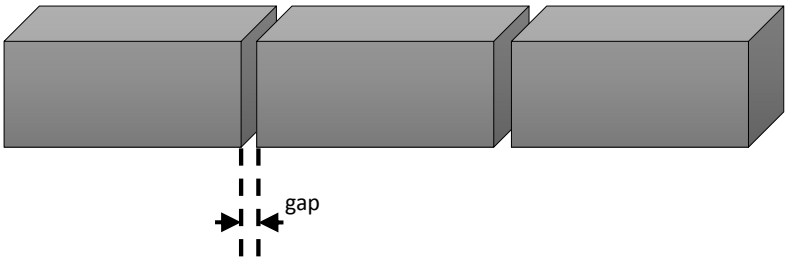


Figure 4.11: Transitional gap.

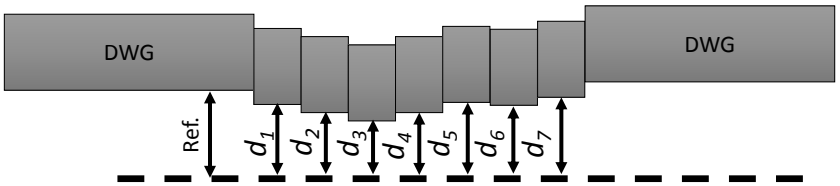


Figure 4.12: Shows different displacements assignment.

for the population; hence, the length of the chromosome string is the number of sliding blocks. The selection criterion used, based on some preliminary trials, is the survival of the fittest and the mutation rate is 1%. A simulated binary crossover is used for mating. Each generation of the 500 generations has a population of 30 individuals.

**Simulation Results**

Fig. 4.13 shows the combined performance of a set of wiggling configurations, resulted from an extensive optimization, with phase shift varying from 0° to 360° in 2.5° steps, an insertion loss between -1.8dB and -4.3dB, and a return loss better than -13dB. Although, a simplified model based on cascading the simulated and stored scattering parameters for arbitrarily shifted 2 wiggling blocks has been used for speeding up the optimization, the final designs were verified and fine-tuned by a commercial full-wave solver (HFSS).

The structure literally increases the signal path, and, hence, introduces a True Time Delay (TTD). In other words, different frequency components shall experience linear phase shifts; therefore, as far as the linearity in phase shift is concerned, all frequencies should be accommodated with our design. By restricting the IL for a tolerance less than $0.5dB$

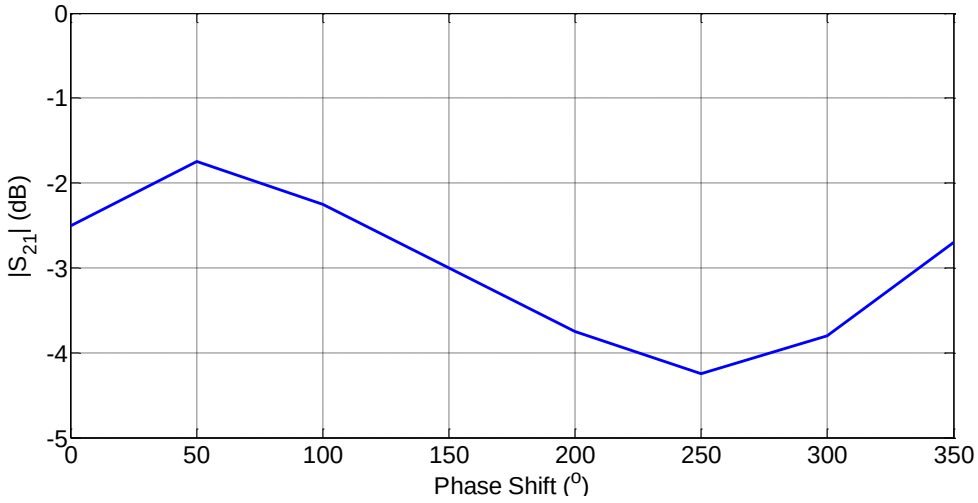


Figure 4.13: Shows the insertion loss vs different phase shifts.

across the entire band of operation, a band width from $75GHz$ to $80GHz$ was obtained. Fig. 4.14 verifies the proposed conclusion about the phase linearity (phase variation slope is constant: $\Delta\phi/\Delta f = -153.6°/GHz$).

**Experimental Results**

To prove the concept, three configurations have been optimized for three different phases. Configuration 1 represents the reference sample where no wiggling occurs. The wiggling values of the other two configurations are shown in Table 4.1. The simulated E field distribution across the top surface of the test structures is shown in Fig. 4.16. The expected values for phase and amplitude normalized to the non-wiggling case are shown in Table 4.2.

A tapered part of the DIG is used as a transition to the WR10 waveguide. WR10 is the PNA-X interface at W-band. The tapered transition has a length of 7mm. The loss of the tapering transition has been characterized separately and its effect has been de-embedded from the measured data. A simple single-mask fabrication process with standard steps and recipes has been used to achieve both low cost and reproducibility. The used substrate

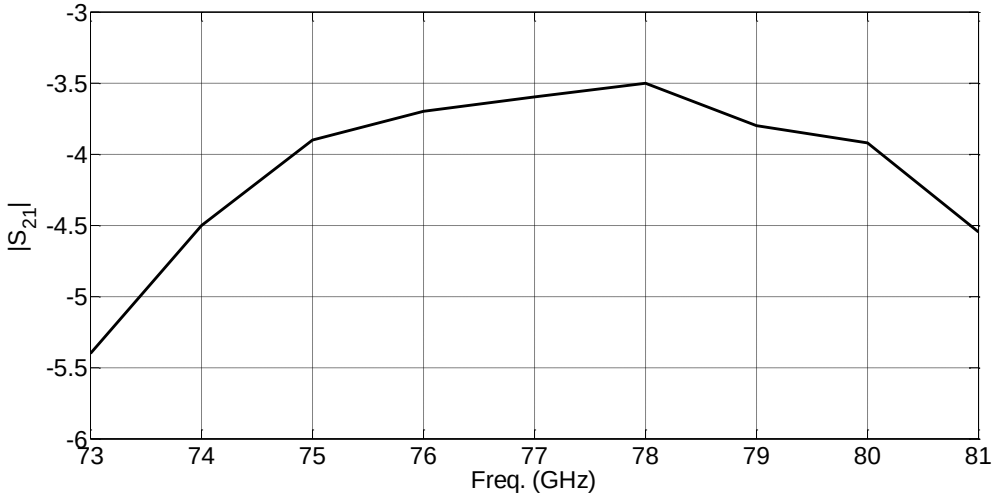


Figure 4.14: $S_{21}$ magnitude variations with frequency for 150° phase shift setup.

Table 4.1: Optimized Configurations.

| Config. | d1-ref | d2-ref | d3-ref | d4-ref | d5-ref | d6-ref | d7-ref |
|---|---|---|---|---|---|---|---|
| 2 | $610\mu m$ | $535\mu m$ | $121\mu m$ | -$245\mu m$ | -$423\mu m$ | $9\mu m$ | $20\mu m$ |
| 3 | $338\mu m$ | $567\mu m$ | $63\mu m$ | -$365\mu m$ | -$607\mu m$ | -$315\mu m$ | -$223\mu m$ |

is high resistivity silicon (1 0 0) wafer with a diameter of 100mm and a thickness of $475\mu m$.

The fabrication process steps can be summarized as shown in Fig. 4.17. Simply, [Step (a)] we clean our high resistivity silicon wafer in Piranha solution before [Step (b)] we sputter 0.5m of Aluminum at each side of the silicon substrate. Then, [Step (c)] we coat it with a thin photo resist (Shibly 1811 with a thickness of 1.3m) on one side of the Aluminum before [Step (d)] performing an optical lithography with a 130mm Chrome mask. [Step (e)] The Aluminum is then patterned using the wet etching process. Meanwhile the back side Aluminum is kept protected with tape. After that, [Step (f)] Deep Reactive-Ion-Etching (DRIE)(Standard Bosch process) is performed for the whole wafer thickness (a carrier wafer is used during the through wafer etching). Then, [Step (g)] we strip the Aluminum mask with Aluminum wet etchant again.

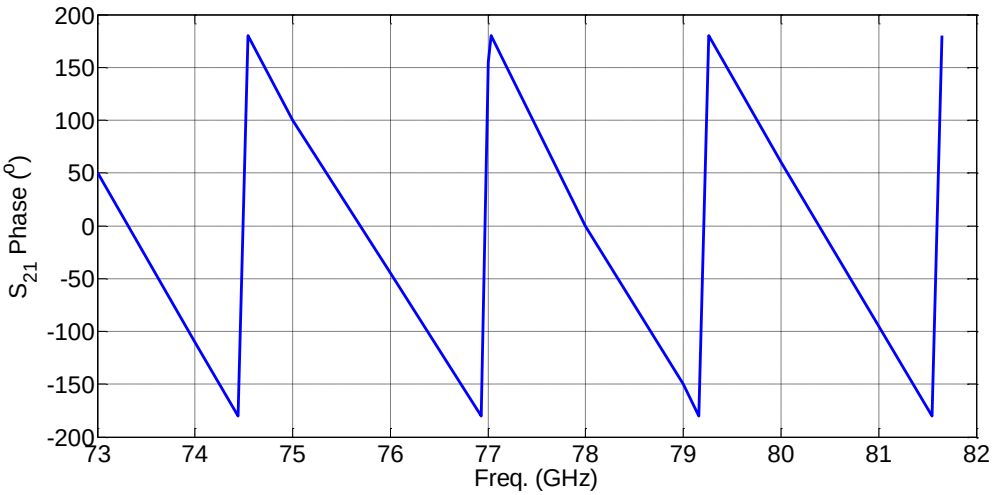


Figure 4.15: $S_{21}$ phase frequency dependence for 150° phase shift setup.

Table 4.2: Configurations simulated performance normalized to Config. 1 at 77GHz.

| Config. | $\Delta\phi$(unwrapped phase) | $\Delta\phi$(wrapped phase) | $\Delta IL$ |
|---|---|---|---|
| 2 | -242$^o$ | 118$^o$ | -1.4dB |
| 3 | 679$^o$ | -40$^o$ | -5.1dB |

Fig. 4.18 shows the fabricated samples along with the measurement setup. The S parameters have been captured using Agilent PNA-X (N5242) attached to W-band OML harmonic mixers.

The simulated and measured (after de-embedding the transition effect) results for the proposed test structures are shown in Figs 4.19 and 4.20. The phase-frequency variations are shown in Fig. 4.19 while the amplitude-frequency variations are shown in Fig. 4.20. A frequency shift of $\sim 0.5GHz$ is observed which could be attributed to inaccurate dielectric constant. The measured insertion loss matches the trend of the simulated one; however there is an additional loss in the measurements which could be due to radiation or mismatch loss created by the test structure non-idealities which are not captured in the simulations.

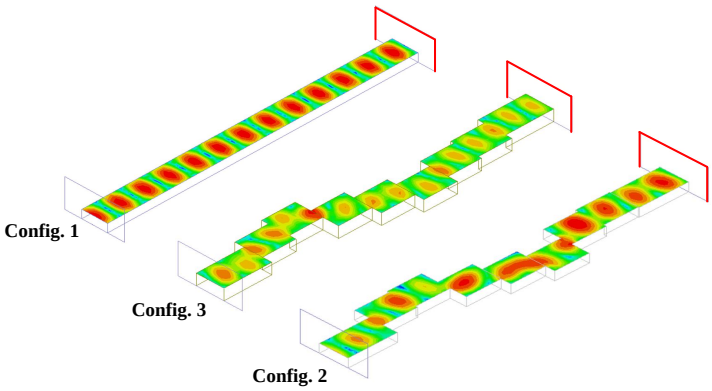


Figure 4.16: E-field distribution for the designed test structures.

### 4.2.4 Phase Shifter Implementation

There are two approaches to implement an electrically controlled phase shifter using the presented structure. The first one is to implement a switched line type phase shifter. This approach is simple but the area is relatively big and the resolution is limited to the number of the WDWGs that can fit in the allocated space. Fig. 4.21 shows this phase shifting concept.

The second approach is to implement vertical actuation using MEMS or piezoelectric effect. This is more complex to implement but provides better performance, compact area and fine resolution.

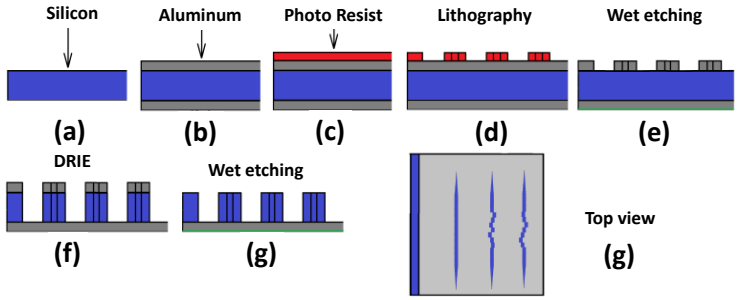


Figure 4.17: Single print through wafer silicon etching process for the wiggling dielectric waveguide fabrication.

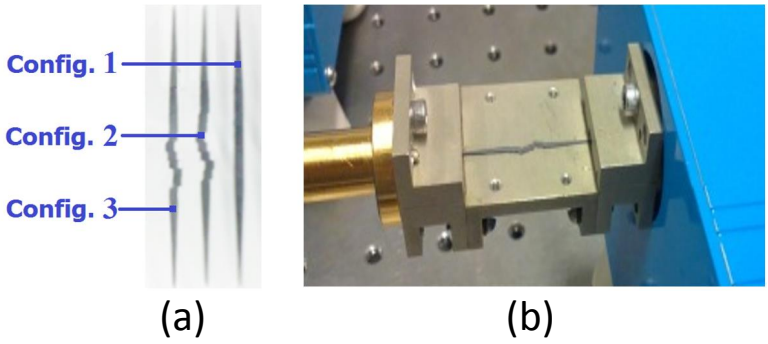


Figure 4.18: a) Three fabricated samples, (b) Measurement setup for the sample with the Configuration 3.

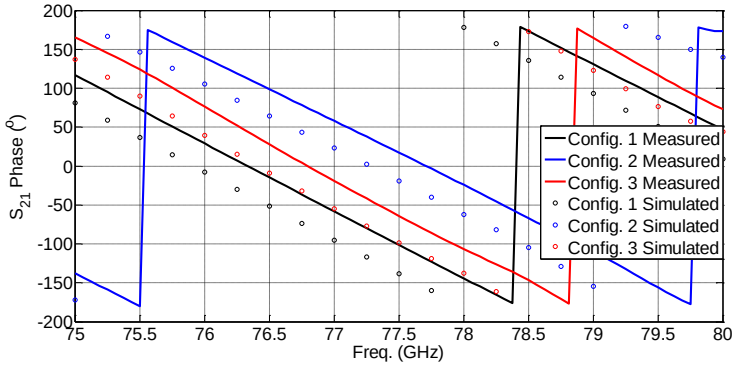


Figure 4.19: $S_{21}$ phase variations with frequency for the three test structures.

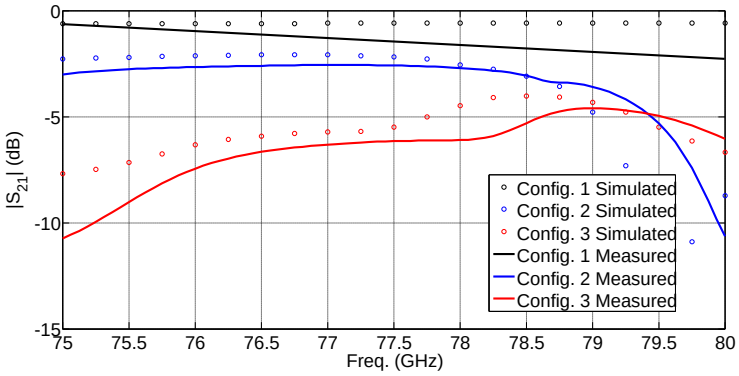


Figure 4.20: $S_{21}$ magnitude variations with frequency for the three test structures.

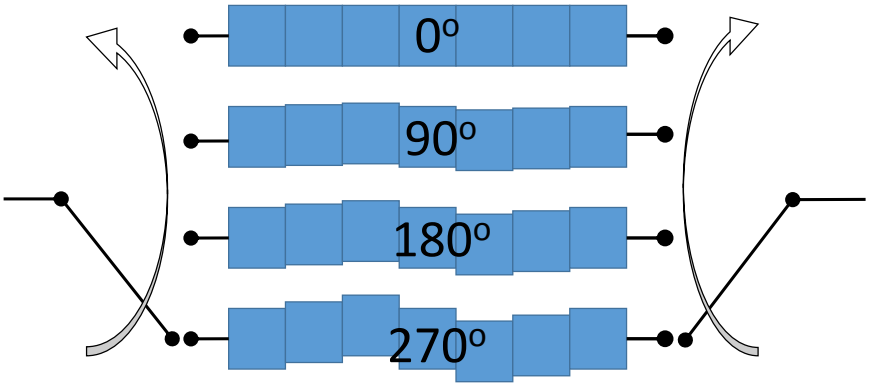


Figure 4.21: WDWG based Switched Line Phase Shifter.

## 4.3 Novel BLT Phase Shifter

In this Section, another new phase shifting structure based on HRS DIG is presented [8]. The proposed structure changes the phase shift of the propagating mode by varying the DIG propagation constant using a high dielectric constant slab of Barium Lanthanide Tetratitanates (BLT) ceramic made of BaO-Ln2O3-TiO2 (where Ln = La, Ce, Pr, Nd, Sm, or Eu). BLT compositions are well known as commercial dielectrics for RF applications due to their high permittivity ($\epsilon_r$ can go up to 170), low temperature coefficient, and low dielectric losses over a wide range of temperatures and frequencies [63]. The used BLT samples have accurate measured dielectric constants with $\pm 0.3\%$ tolerance (provided by supplier).

The high dielectric constant leads to a significant size reduction, which is highly desirable in many practical applications. Recently, we have presented a microwave phase shifting structure based on a BLT ceramic loaded CPW line[4]. The proposed CPW-based phase shifter is shown in Fig. 4.22. Although this structure has a superior performance in the Ka-band, it is not very practical in higher mmWave/sub-THz frequency range due to the loss and the fabrication limitations; therefore, here we extend the concept proposed in [4] to a new BLT loaded HRS DIG phase shifter.

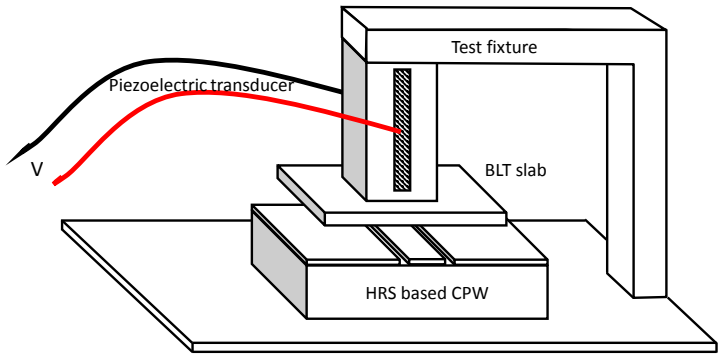


Figure 4.22: 3D model of a test structure for the proposed phase shifter.

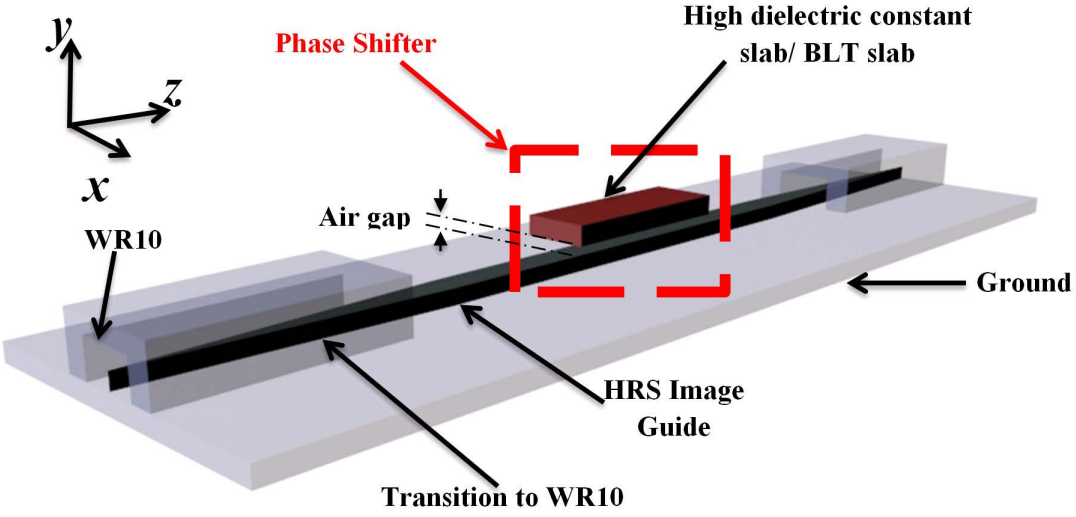


Figure 4.23: 3D model of a test structure for the new BLT-loaded HRS DIG phase shifter.

### 4.3.1 Design

As shown in Fig. 4.23, the proposed concept uses a DIG using HRS substrate. The propagation constant and the mode of the DIG is changed by placing a high dielectric constant BLT material on top of it at a small distance (few microns). A large variation of the phase shift is obtained by changing the air gap only by several microns. To prove the concept, phase shifters with different types of BLT materials with dielectric constants up to $\epsilon_r = 165$ have been simulated, fabricated and successfully tested. The resulting tuneable phase shifter has minimal insertion loss variation, less than that other techniques reported so far, over the full range of phase shift.

The design procedure of this phase shifter test structure is summarized in the following steps:

#### Step 1: Design of a W-band HRS based DIG

The HRS rectangular cross section DIG is designed to ensure a single mode operation $E_y^{11}$ across the bandwidth of interest. The design sample under consideration is optimized to

operate over the W-band ($75GHz$ to $110GHz$). For the particular design example reported in this work, the DIG has a width of $700\mu m$ and a height of $500\mu m$. The total length of the waveguide is $10mm$. A cross section of the DIG showing the E field distribution at $100GHz$ is depicted in Fig. 4.23.

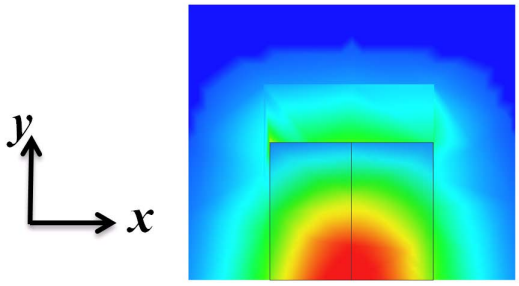


Figure 4.24: Cross section in the DIG shows the E field magnitude distribution at 100GHz.

**Step 2: Design of HRS DIG to WR10 metallic waveguide transition**

To test the proposed phase shifter, a transition from HRS DIG to $WR10$ waveguide ports has been designed. An HRS dielectric linear tapered section is added to the rectangular DIG [1]. The total length of the matching section ($5.7mm$) has been chosen to provide a compact but low loss transition. Fig. 4.25 and Fig. 4.26 show the $3D$ of model in HFSS for the whole test structure along with E field distribution at $100GHz$.

Fig. 4.27 shows the simulated S-parameters for this test structure (this includes the DIG, the transition and the metallic waveguide). The ripples in $S_{11}$ are due to small mismatches at both ends (Fabry Perot resonances). Although the transition plays important role in testing the phase shifter, it is not a part of the phase shifter itself. For example, the phase shifter can be part of homogenous DIG based phased array antenna system or integrated directly to flip-chip based active components through DIG to CPW transition [15] without the tapered transition. Hence, the phase shifter actual size should not include the tapered transition length.

[1] More details about this transition is available in Chapter 5

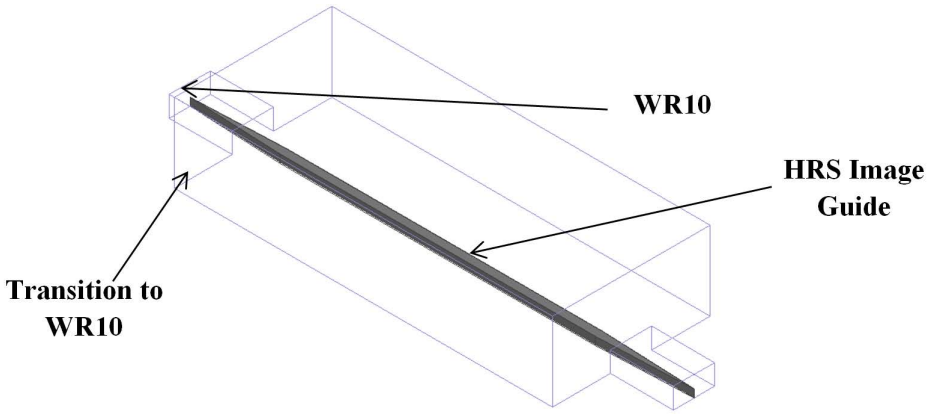


Figure 4.25: HFSS model of the whole test structure.

**Step 3: BLT slab design and air gap calculation**

The effect of the high dielectric constant slab top loading on the DIG dominant mode propagation with a small air gap in between has been studied by simulations. Different dielectric materials with different lengths have been placed at different distances from the DIG. An example is given here for a BLT sample with a relative permittivity of 165 and a length of $5mm$. When the spacing between the BLT slab and the DIG is $5\mu m$, the $S_{21}$ magnitude and phase are $-2dB$ and $113^o$ respectively and the field distribution is given by Fig. 4.28. When we increase the air gap by $20\mu m$ the $S_{21}$ magnitude and phase change to $-1.97dB$ and $-157^o$ respectively and the field distribution is given by Fig. 4.29. The difference in phase between the two cases is almost $90^o$ $((180 - 113) + (-157 - -180))$ this can be visually checked by comparing the time domain E field distribution for the two cases shown in Fig. 4.28 and Fig. 4.29.

The used BLT slab has a thickness of $250\mu m$ and a width of $2mm$. Practically, both the width and the thickness of the BLT slab (as long as it is much larger than the air gap) should not have any appreciable effect on the performance. Three different BLT slabs (samples) have been studied for the proposed phase shifter application. Fig. 4.30 shows a comparison between the three samples at $100GHz$. The first sample has a dielectric constant of 42 and a length of $5mm$. Sample 2 has a dielectric constant of 80 and a length of $3mm$. Sample 3 has a dielectric constant of 165 and a length of $5mm$.

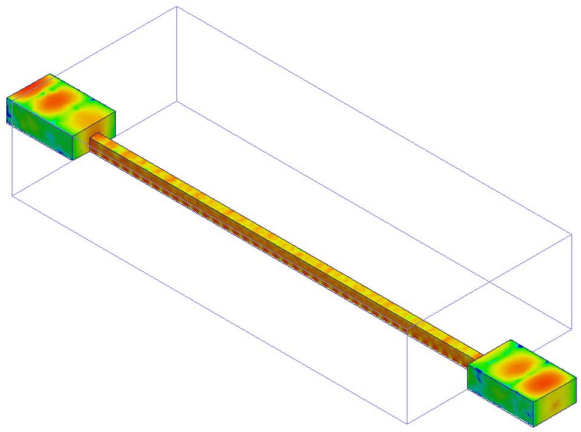

Figure 4.26: E field distribution at 100GHz.

### 4.3.2 Fabrication Process

#### Optical lithography and dry etching

The HRS has been fabricated using a single-mask fabrication process. The fabrication details for an HRS single-mask dry etching process have been covered previously in this thesis. The fabrication process steps can be summarized as shown in Fig. 4.31. One of the main advantages of this technique is its high-dimensional accuracy obtained from the photolithography and DRIE processes. With photolithography, depending on the quality of the Chrome mask, very small dimensional errors down to $\pm 0.3\mu m$ are realizable. The DRIE process is able to provide almost vertical sidewalls with a very small roughness.

Fig. 4.32 and Fig. 4.33 show the picture and SEM scans of the fabricated waveguide sample. HFSS simulations show that the effect of roughness on the propagation constant of the waveguide is negligible. The measured width of the fabricated waveguide is $700 \pm 2\mu m$.

The roughness of the Silicon surface was measured by a profiler. The standard deviation value of the surface roughness is $13nm$ (see Fig. 4.34).

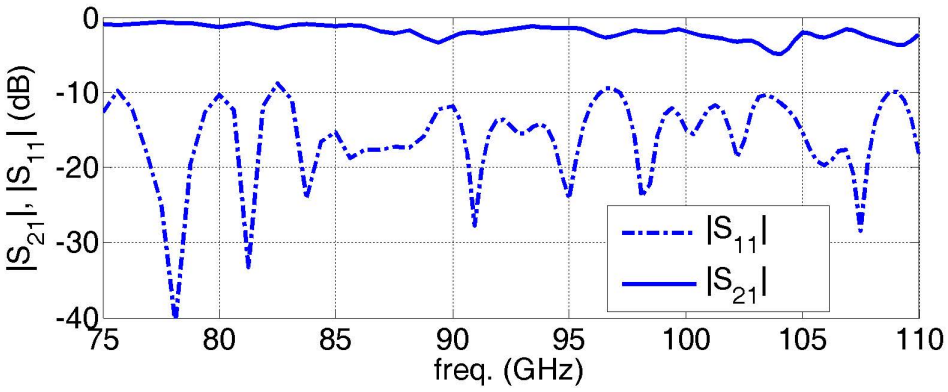


Figure 4.27: Simulated $S_{21}$ and $S_{11}$ magnitudes versus frequency.

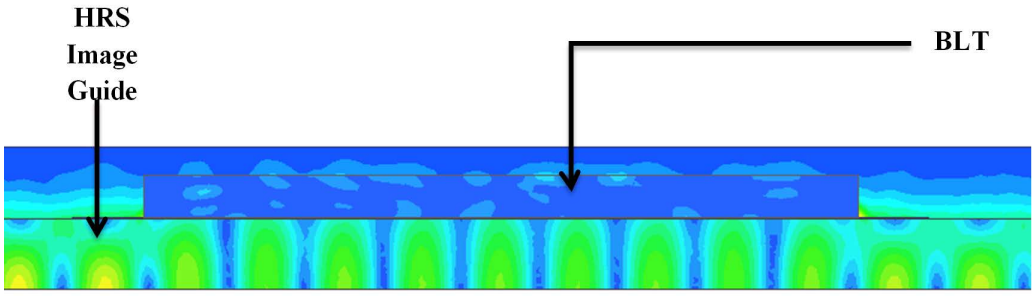


Figure 4.28: E Field distribution at 100GHz longitudinal cut at air gap=5$\mu m$.

### Laser micro-machining

The BLT slab has been cut using laser machining. Laser machining is an accurate, chemical-free, and fast process (no mask preparation is needed) which can be used as an alternative solution to etching technique in many emerging applications. The laser machine which is used for cutting the BLT samples is the ProtoLaser U3 UV system from LPKF. The laser wavelength is 355$nm$. Since the 200$\mu m$ thick BLT material is very fragile, it can be easily broken with excessive laser power. Therefore all the laser parameters are optimized to achieve a clean edge cut without breaking the sample. Fig. 4.35 shows the surface roughness of the BLT slab after polishing. Based on our measurements, the standard deviation value of the surface roughness is 79$nm$.

As can be seen from the graph, the BLT slab has (as well as many of ceramic based

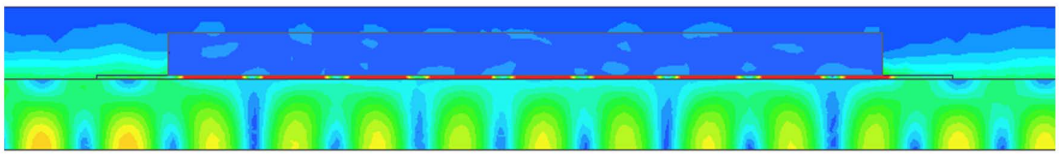

Figure 4.29: E Field distribution at 100GHz longitudinal cut at air gap=25$\mu m$.

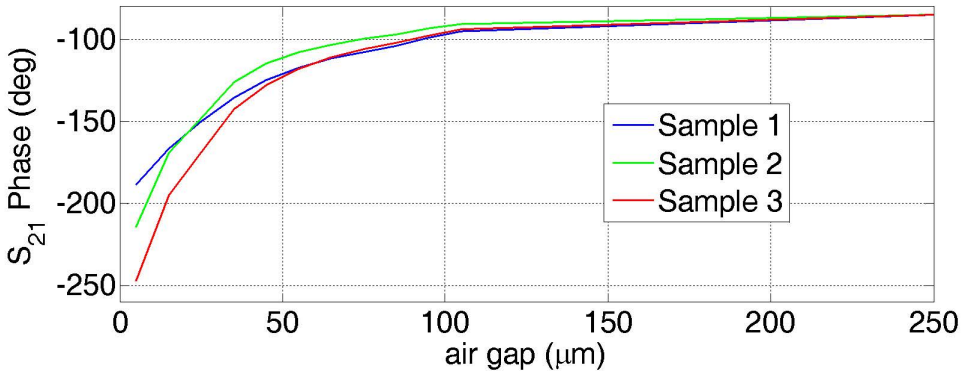


Figure 4.30: Phase shift variation versus air gap at 100GHz for the studied samples.

material) some surface cracks. Since the width of these discontinuities are in the order of few microns, the effect is negligible on the dielectric constant over the frequency range of interest in this work. This has been verified with the good agreement between simulations (where the BLT slab model does not have these sharp discontinuities) and measurements as will be shown later.

### 4.3.3 Measurements Results

The measurement is performed using a micro-positioner with a probe end attached to the top side BLT sample. The attachment is done using a $\sim 10\mu m$ drop of silver paste. The paste has insignificant effect on the operation as the E field is highly concentrated under the BLT slab (inside the air gap region), while the glue exists on the other side of the BLT slab.

The measurement is performed using Agilent PNAX connected to OML mmWave

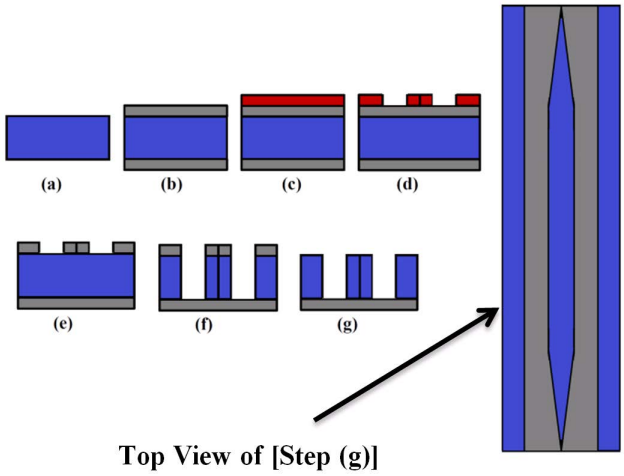


Figure 4.31: Optical lithography Fabrication Process for the proposed structure.

Figure 4.32: Fabricated sample: Picture of the waveguide.

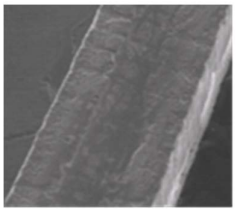

Figure 4.33: Fabricated sample: SEM scan of the waveguide.

WR10 extenders. The micro-positioner setup is used to move the BLT slab up and down and vary the air gap with high accuracy. The measurement setup along with the test structure is shown in Fig. 4.36 and Fig. 4.37. The surface roughness limits the minimum air gap between the HRS DIG and the BLT slab. The calibration and initial measurement are done for the HRS DIG in the absence of BLT slab and the results are shown in Fig. 4.38.

The measurement results presented in this Section are obtained for the following three different high dielectric constant slab samples:

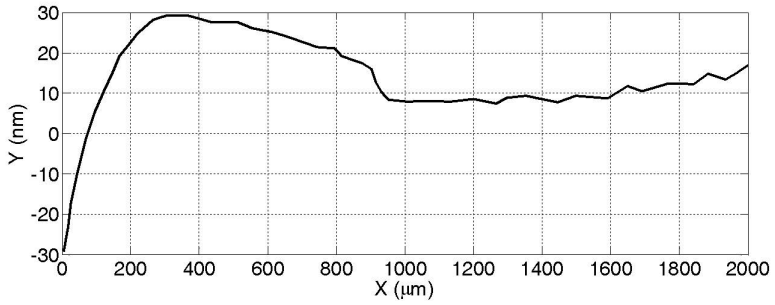


Figure 4.34: Silicon surface roughness profile.

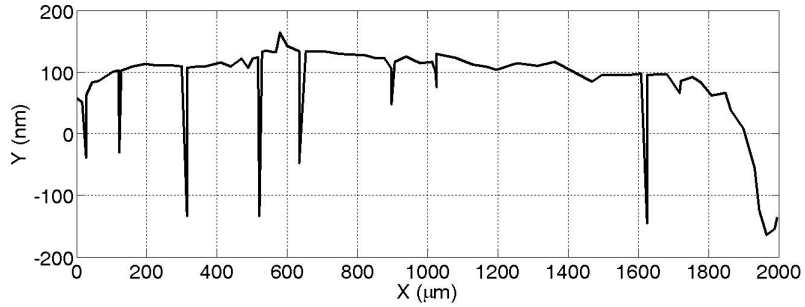


Figure 4.35: BLT slab surface roughness profile after polishing.

**Sample 1**

The high dielectric constant slab for Sample 1 has a dielectric constant of 42 and a length of $5mm$. Fig. 4.39 shows the $S_{21}$ and $S_{11}$ magnitudes variation versus frequency for different air gaps. The $S_{21}$ phase variation versus frequency is shown in Fig. 4.40. In all the following graphs each micro-positioner step is considered $10\mu m$.

**Sample 2**

The high dielectric constant slab for Sample 2 has a dielectric constant of 80 and a length of $3mm$. Fig. 4.41 shows the $S_{21}$ and $S_{11}$ magnitudes variation versus frequency for different air gaps. The $S_{21}$ phase variation versus frequency is shown in Fig. 4.42.

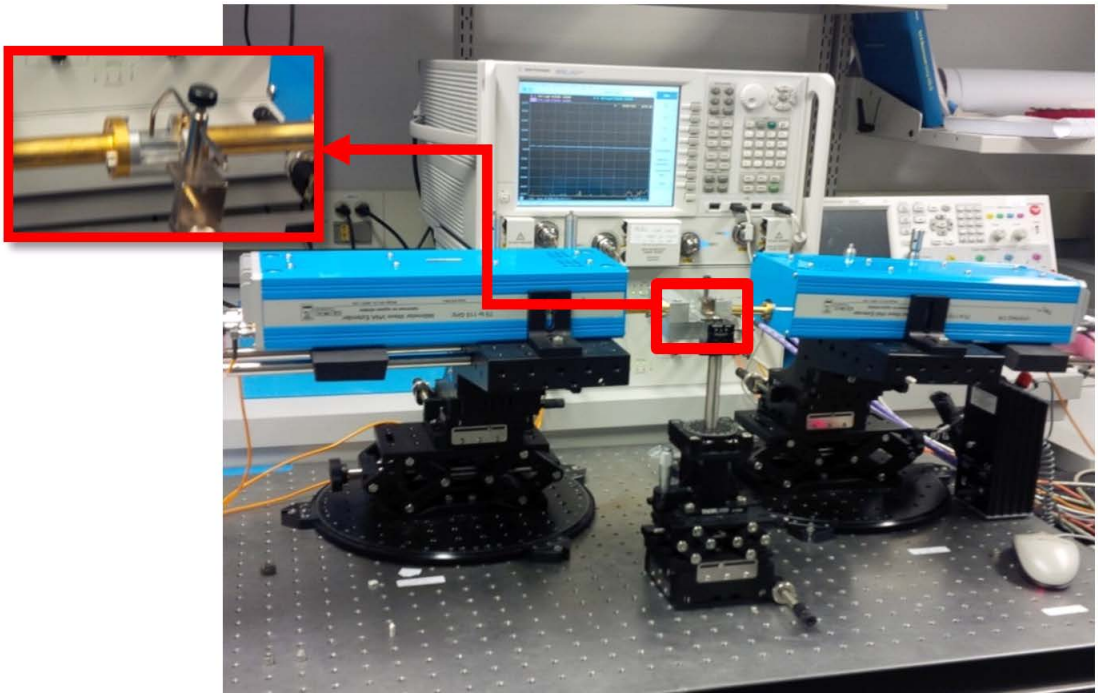

Figure 4.36: The experimental setup.

### Sample 3

The high dielectric constant slab for Sample 3 has a dielectric constant of 165 and a length of $5mm$. Fig. 4.43 shows the $S_{21}$ and $S_{11}$ magnitudes variation versus frequency for different air gaps. The $S_{21}$ phase variation versus frequency is shown in Fig. 4.44. The main phase change occurs in the first two steps ($20\mu m$) which is suitable for practical application.

### Summary of measurements

Three different high dielectric constant slabs have been tested. Summary of the measurements results at $100GHz$ for different dielectric samples are shown in Table 4.3. Fig. 4.45 shows a comparison between the simulations and measurements of the obtained phase shifts for the three tested samples at $100GHz$.

It can be noticed that the loss of smaller phase shift $60^o$ is actually higher than the larger phase shift $107^o$. This can be attributed to the fact that that the larger phase shift is

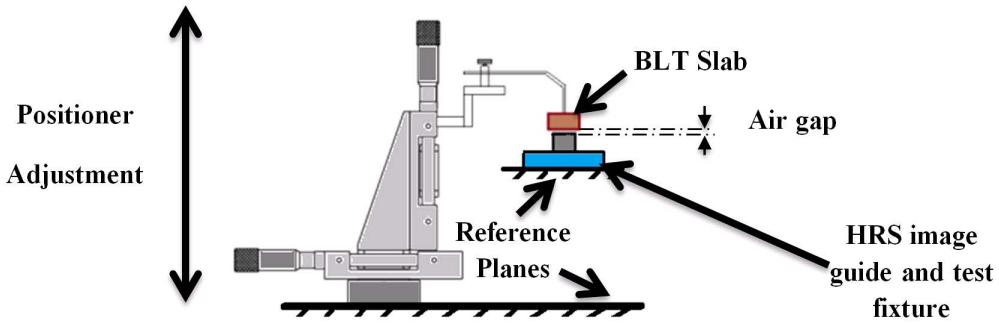


Figure 4.37: Schematic of the micro-positioner setup.

Table 4.3: Summary of Measurements at $100GHz$.

| Sample | Maximum Phase Shift | Average Insertion Loss | Insertion Loss Variation |
|---|---|---|---|
| 1 | $60^o$ | $-3dB$ | $1dB$ |
| 2 | $107^o$ | $-2.8dB$ | $0.6dB$ |
| 3 | $150^o$ | $-2.85dB$ | $0.7dB$ |

obtained using a higher dielectric constant slab which makes the fields more concentrated in the lossless air gap.

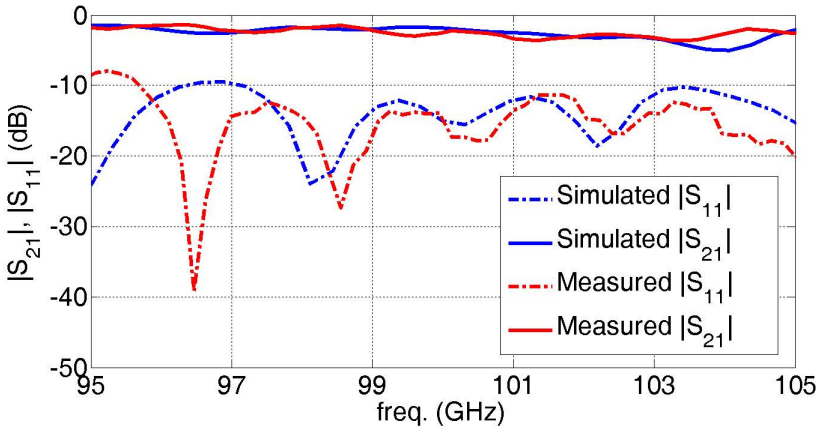


Figure 4.38: Measured and simulated magnitudes of $S_{11}$ and $S_{21}$ versus frequency for the DIG in the absence of the BLT slab.

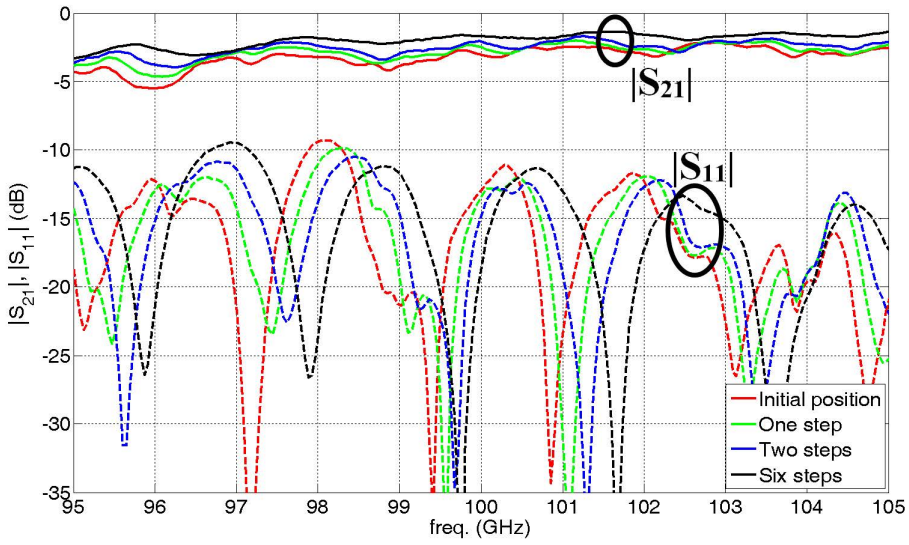


Figure 4.39: Measured $S_{21}$ and $S_{11}$ magnitude variation versus frequency for different air gaps.

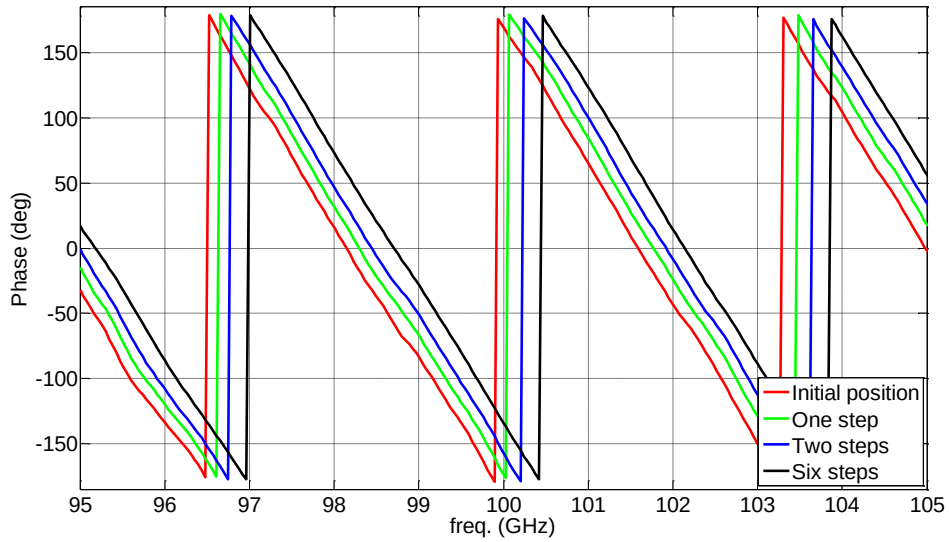


Figure 4.40: Measured phase variation versus frequency for different air gaps.

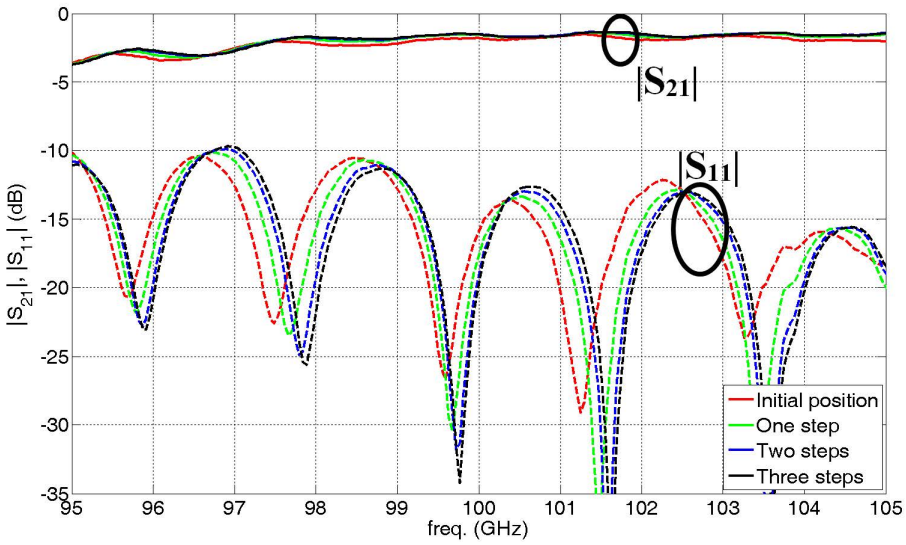


Figure 4.41: Measured $S_{21}$ and $S_{11}$ magnitude variation versus frequency for different air gaps.

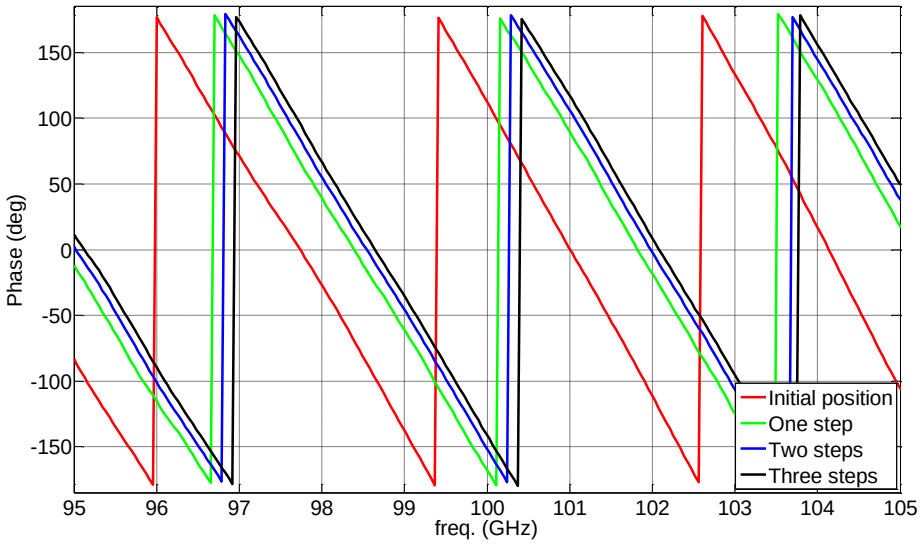


Figure 4.42: Measured phase variation versus frequency for different air gaps.

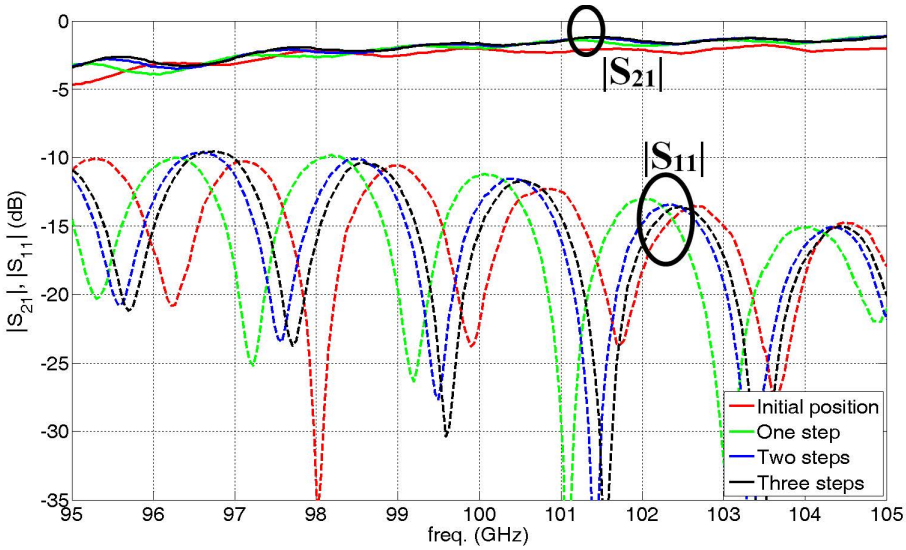


Figure 4.43: Measured $S_{21}$ and $S_{11}$ magnitude variation versus frequency for different air gaps.

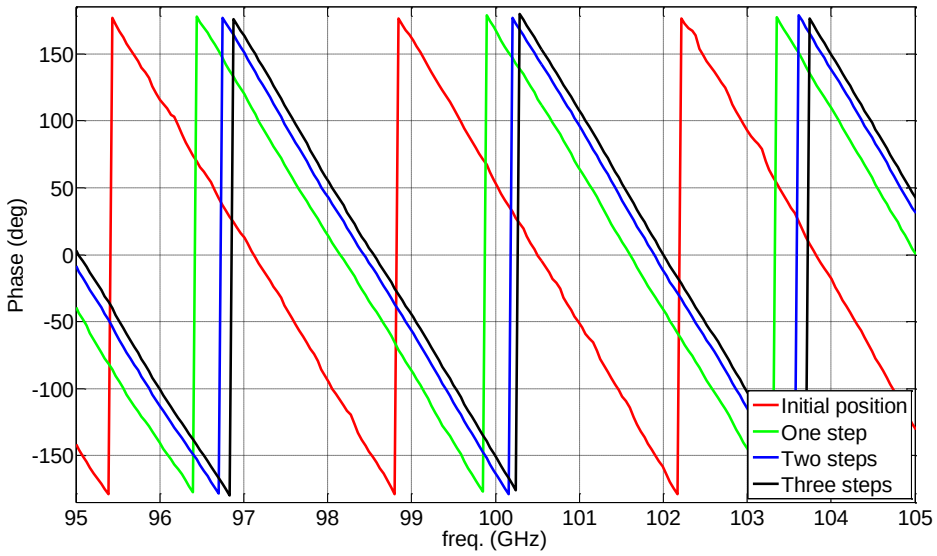


Figure 4.44: Measured phase variation versus frequency for different air gaps.

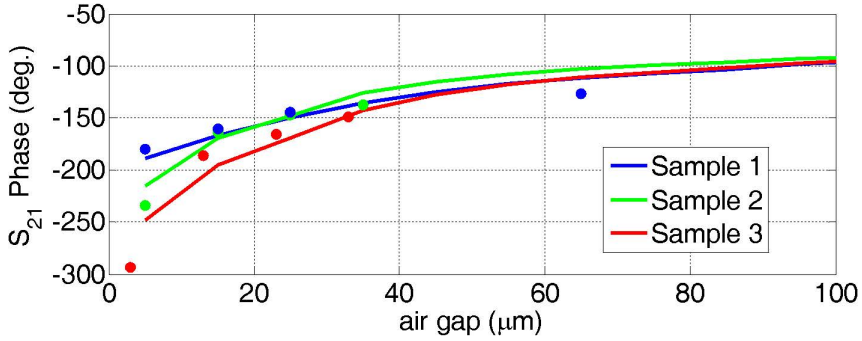


Figure 4.45: Phase shift variation simulations (solid line) and measurements (circles) versus air gap at 100GHz for the studied samples.

### 4.3.4 Electrically Controlled Version

After we have proven the new phase shifter concept using micro-positioner setup, we are going to present a more practical version (from packaging point of view) of the phase shifter[9]. In this Section, an electrically controlled version of the proposed phase shifter is presented.

#### Design

As shown in Fig. 4.46, the proposed phase shifter is essentially a high dielectric constant slab attached to a piezoelectric transducer and both are kept at a controllable distance from an HRS DIG.

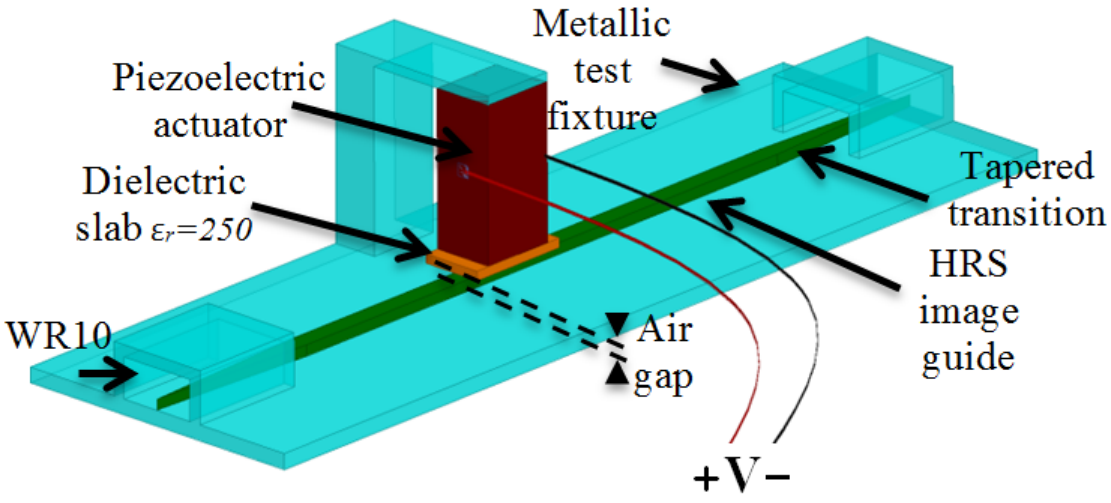


Figure 4.46: 3D model for the electrically controlled version of the proposed phase shifter.

There are various types of piezoelectric actuators that can be used in this application. We chose a commercial piezoelectric actuator [30] that has dimensions of $2 \times 3 \times 13.5mm$ and a travel range of $13\mu m$. The dielectric slab used in this work has a dielectric constant of 250 and has a length of $4mm$, a width of $2mm$ and a thickness of $0.5mm$.

### Results

In This test, the HRS DIG has been cut using the laser technique which provides a fast and no-mask prototyping method. An extra step is added to remove the oxidation layer with Silicon wet etching. The dielectric slab is then attached to the piezoelectric transducer with glue. The whole test structure has been tested using the measurement setup shown in Fig. 4.47. The piezoelectric attachment is depicted in Fig. 4.48 and Fig. 4.49.

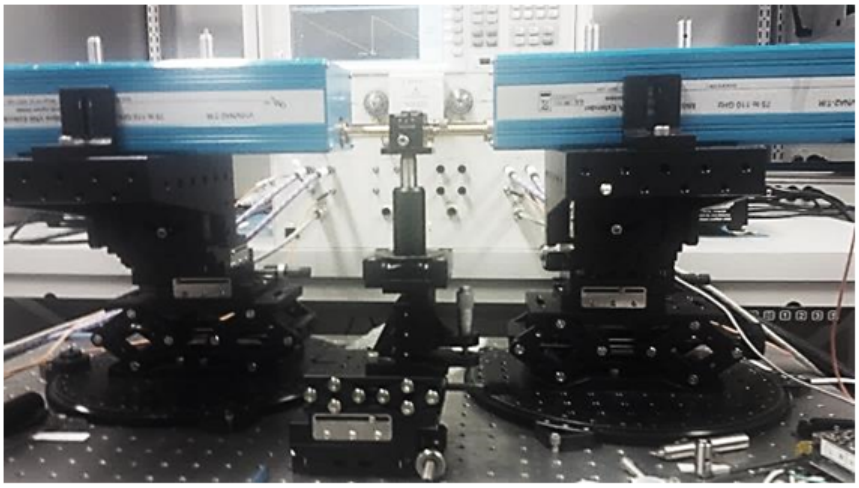

Figure 4.47: Measurement setup.

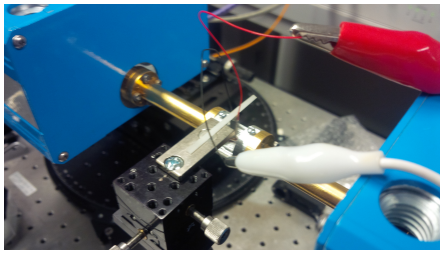

Figure 4.48: Piezoelectric transducer.

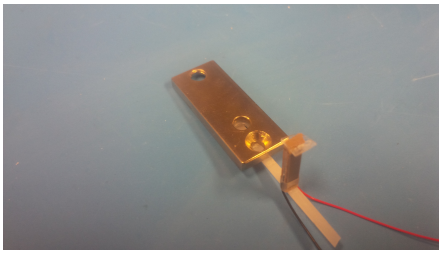

Figure 4.49: Piezoelectric attachment to the BLT slab.

For calibration, the HRS DIG was tested alone (without the dielectric slab). In this

Section we modified the test fixture to make sure the HRS DIG is fixed during the test (See Fig. 4.50). The measurement results are shown in Fig. 4.51. The insertion loss is $-1.8dB$ at $90GHz$. The structure is matched over the frequency band of interest except for small Fabry Perot resonances due to the mismatch introduced by the two transitions and the screws in the fixture.

Figure 4.50: Modified test fixture.

After measuring the HRS DIG alone, the whole test structure, including the high dielectric constant slab, (shown in Fig. 1) has been tested. The simulated and measured S-parameters are shown in Fig.s 4.52 and 4.53. The graphs show the insertion loss, return loss, and phase shifting characteristics of the developed phase shifter for two values of the piezoelectric transducer voltages. The measurements show a phase shift of $85^o$ at $90GHz$ with very low insertion loss variation ($-0.2dB$).

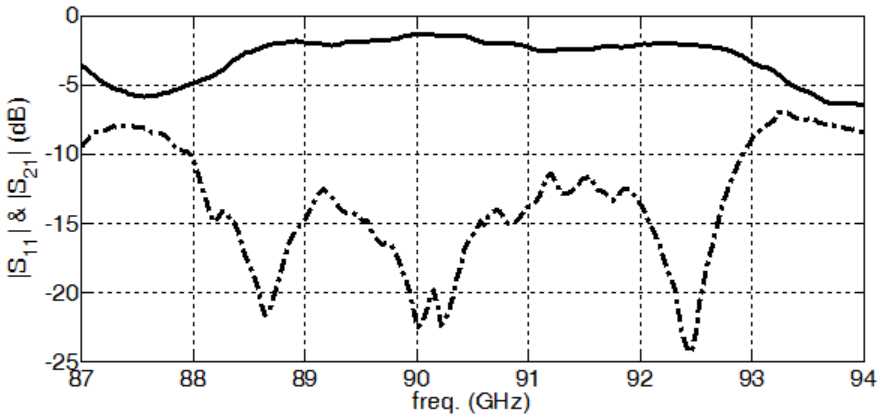


Figure 4.51: Measured $\|S_{11}\|$ and $\|S_{21}\|$ of the DIG in the absence of the dielectric slab.

Table 4.4 summarizes the performance of the proposed phase shifter as compared to other good designs reported in the literature. As shown, the $\Delta\phi/IL$ value of the proposed

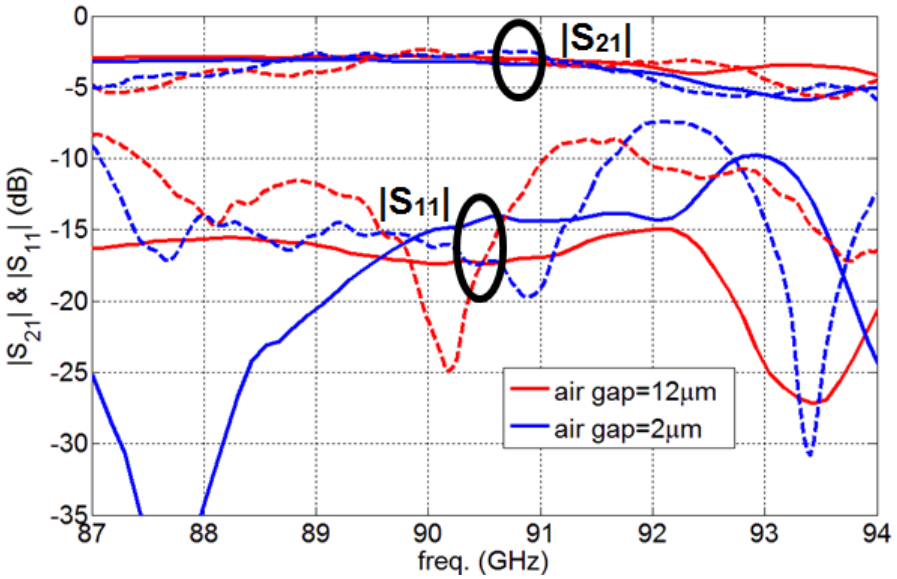


Figure 4.52: $\|S_{11}\|$ and $\|S_{21}\|$ of the test structure for two different states of the piezoelectric transducer. The measurement results are shown in dotted lines while the simulation results are shown in solid ones.

phase shifter clearly outperforms the other designs.

On the subject of mechanical reliability, from our experience with the measurement setup, the presented BLT phase shifter performance is immune from mechanical vibrations due to movements. The proof is simply that we had the measurement setup for this experiment installed on a normal table inside one of the labs where different researchers have been moving during the measurements; however, the phase shift characteristics are yet quite stable. We think that this is due to the fact that any type of oscillation applies equally to both the dielectric waveguide and the dielectric slab. This makes the change in the air gap value negligible.

As for the thermal stability, when the ambient temperature changes, the dielectric constant of the BLT slab changes and the air gap thickness changes as well. However, the dielectric constant for the BLT material used is fairly stable $\leq 30 ppm/^{\circ}C$. To make the air gap constant, a fixture with thermal expansion coefficient similar to that of the piezoelectric transducer should be used.

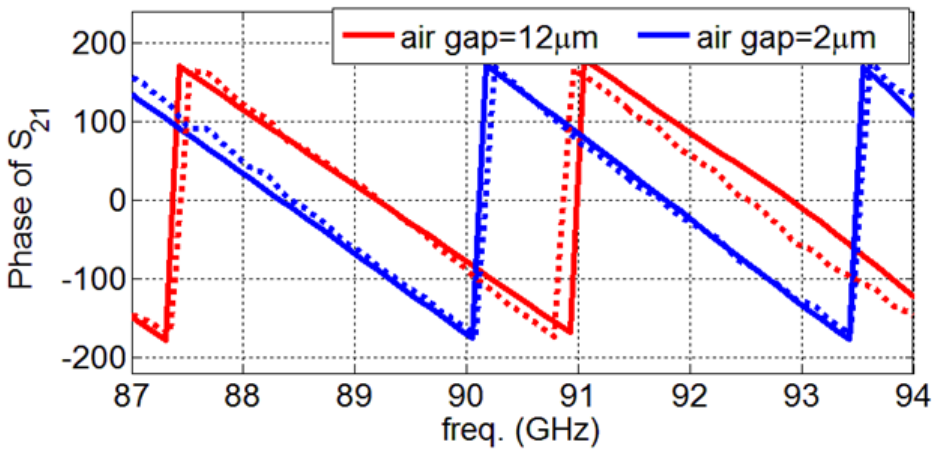


Figure 4.53: Measured phase shift of the test structure for two different states of the piezoelectric transducer. The measurement results are shown in dotted lines while the simulation results are shown in solid ones.

In addition, most of the phased array systems usually have complex calibration systems to deal with the performance deviation over temperature. This drift is normally slow and weak.

Table 4.4: Performance Comparison of Available Phase Shifters.

| Design | $Freq.(GHz)$ | $\Delta\phi/IL(^o/dB)$ | $Max.IL(dB)$ | $\Delta\phi/Length(^o/cm)$ |
|---|---|---|---|---|
| Ref [76] | 76.5 | 55 | -5.8 | 129 |
| Ref [73] | 75 | 71 | -3.5 | 715 |
| This work | 90 | 405 | -2.8 | 210 |

# Chapter 5

# HRS DWG Integration with Active Components

This Chapter is focused on the integration of the aforementioned passives (the proposed integration techniques are also applicable for any DWG-based passives) with active components. This is an essential task for achieving a low cost and high performance mmWave beam-steering antenna system. Our investigation so far shows that the optimal integration with active components can be achieved through a high performance flip-chip to rectangular DWG transition. The following Section justifies this approach.

## 5.1 Flip-chip on DWG Packaging Approach

The rectangular DWG has been chosen for this transition because it is easy to fabricate (low cost) and easy to integrate with all of our proposed high performance passive components [1]. As for the assembly method, the flip-chip technology has been chosen. The flip-chip technology provides an RF connection with a short electrical length compared to wirebonding and hence the associated parasitics are considerably smaller [55]. For this reason, the flip-chip has recently attracted huge attention among the mmWave integration and packaging community [35], [37] and [11].

[1] For a detailed discussion about the different advantages of using DWG for mmWave applications please visit Section 3.1.

In order to achieve low loss, low cost, wide band, and compact flip-chip to DWG transition at mmWave frequencies, I present the structure shown in Fig. 5.1. Since the CPW lines are usually used on both sides of the flip-chip connection, a transition from DWG to CPW has been used. For simplicity, the proposed structure can be divided into three transitions (equivalently three design steps):

- Step 1: Metallic waveguide (WR10 has been used in this example) to dielectric waveguide (DWG) transition (this transition has been introduced for testing purposes only),
- Step 2: DWG to CPW transition,
- Step 3: CPW to flip-chip transition,

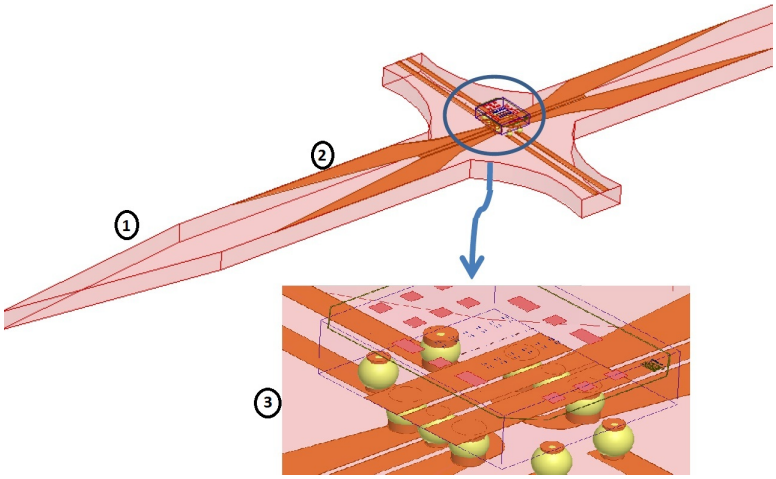


Figure 5.1: 3D model of the proposed flip-chip integration structure.

The shape of these transitions have been inspired by the modal characteristics of the electromagnetic waves' propagation in these three types of structures. The silicon waveguide starts with a tapered transition to gradually match the mode diameter of the WR10 waveguide. The CPW starts with a tapered transition as well to minimize the reflection and smoothly focus the field between the metals. The CPW final spacing has the 50Ω impedance to match the flip-chip circuit input impedance. As will be shown later, the impedance should be slightly different than 50Ω to cancel the parasitics introduced by flip-chip bumps and pads. The CPW ground traces are tapered again before the flip-chip

to ensure more confined signal transmission. The design details of the proposed integration technique will be discussed in the following Sections.

## 5.2 WG to DWG/DIG Transition (Step 1)

The mode diameter of the metallic waveguide should be gradually matched to that of the DWG. This can be achieved with a simple tapered DWG transition as shown in Fig. 5.2. The idea of matching DWG to waveguide using linear tapering has been rigorously explored in literature [54]. In Fig. 5.2, we explore the effect of changing the tapering profile on the matching. The tapering length ($L_t$ in Fig. 5.2) should be optimized to achieve the smallest transition with the maximum transmission and the minimum reflection.

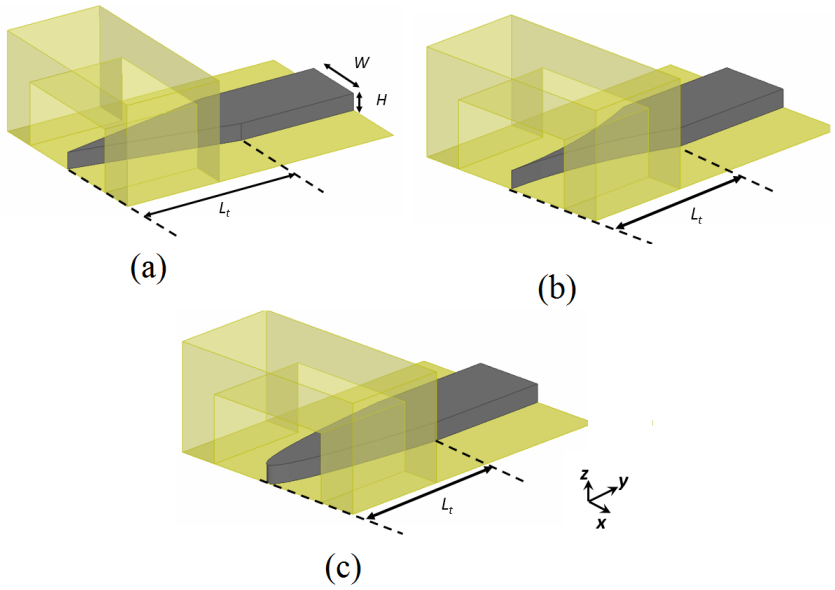


Figure 5.2: 3D model for the proposed WG to DIG tapered transition with different profiles; (a)Profile 1: y=$\alpha_1$x, (b)Profile 2: x=$\alpha_2 y^2$ and (c)Profile 3: y=$\alpha_3 x^2$.

Fig. 5.3 shows the HFSS simulation results for V-band WG to DIG transitions with three different profiles. By increasing the tapering length, the matching and the insertion

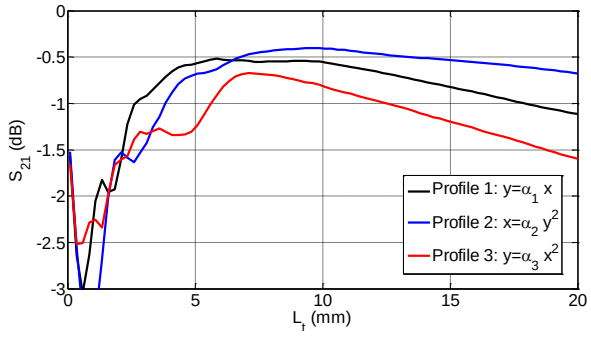


Figure 5.3: Transition insertion loss vs tapering length $L_t$ for different tapering profiles.

loss get better but at some point the transition length starts to add significantly to the total loss; therefore an optimal point should be chosen. It can be seen that for a short transition length, the linear profile (Profile 1) is better as it adds only -0.5dB at a length of 6mm. However, if the transition is allowed to be longer, Profile 2 seems to work better (Profile 2 provides -0.4dB at a length of 10mm).

### 5.2.1 Test Structure: Back-to-Back WG to DIG to WG transition

The performance of the WG to DIG transition can be verified by the test structure shown in Fig. 5.4. This test structure is a 20mm long V-band DIG followed by 6mm linear tapered transitions on both ends (total length is 32mm). The simulated S-parameters are shown in Fig. 5.5. A similar test structure for the W-band has been designed and measured. The cross section of the DIG is $0.7mm \times 0.5mm$ with a length of 10mm. A picture of the fabricated test structure is shown in Fig. 5.6. The used tapered section has a length of 6mm.

Fig. 5.7 shows the measured and simulated results for the proposed W-band test structure. It has been noticed that there is some discrepancy between the simulated and the measured results specially in the matching ($|S_{11}|$) frequency response. This is mainly due to the surface roughness of the test fixture (which introduces air gap in the DIG structure) and the in-accurate positioning of the DIG. To reduce the gap between simulations and measurements, a higher quality test fixture/setup is needed; however, it would be quite

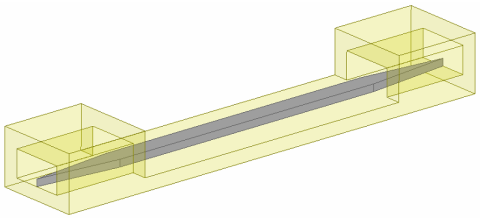

Figure 5.4: V-band back-to-back WG to DIG test structure with linear 6mm tapered transition.

expensive [2]

[2]As an example, the results for an experiment we have performed with a higher quality test fixture is given in Section 3.1.

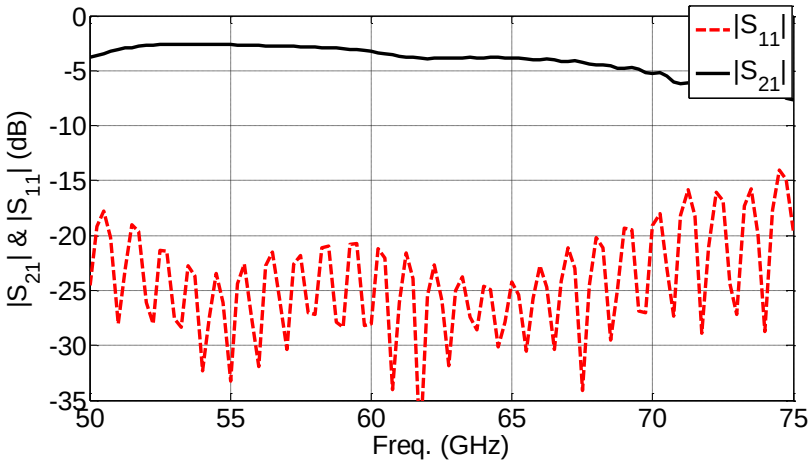


Figure 5.5: Simulated S-parameters for a V-band back-to-back WG to DIG test structure with linear 6mm tapered transition.

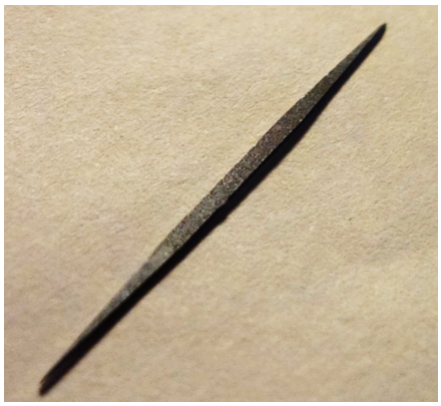

Figure 5.6: Fabricated W-band back-to-back WG to DIG test structure.

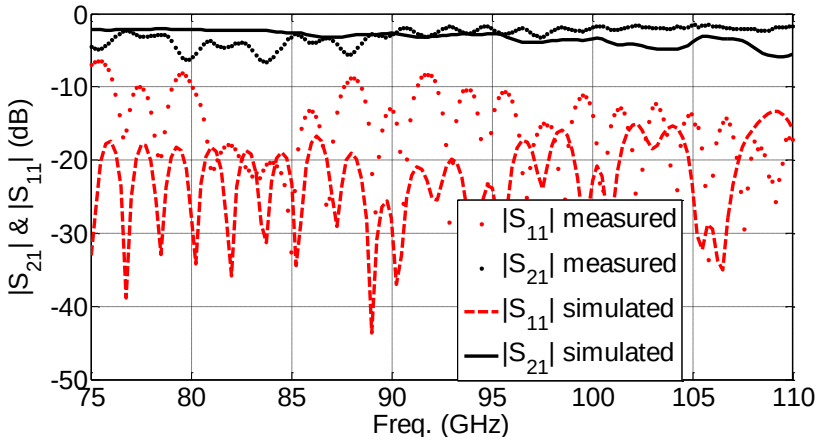


Figure 5.7: Simulated S-parameters for a W-band back-to-back WG to DIG test structure with linear 6mm tapered transition.

## 5.3 CPW to DIG Transition (Step 2)

A CPW to DIG transition is presented in this sub-Section. A gradual tapered transition is used to match the CPW line to the DIG. Fig. 5.8 shows two tapered profiles we have explored for this type of transition. The tapering is done on the ground traces of the CPW line only (Since it is already narrow, we decided not to taper the signal trace). We have proposed two tapering profiles; one is the simple linear tapered profile while the other is a quadratic profile. The transition is essentially defined by two variables. The first variable (which will be referred to as $L_{t1}$) is the extension of the ground traces after the 50Ω CPW line section. The other variable (which will be referred to as $L_{t2}$) is the extension of the signal trace (middle conductor) after the 50Ω CPW line section.

The performance of the proposed CPW to DIG transition can be tested by making ei-

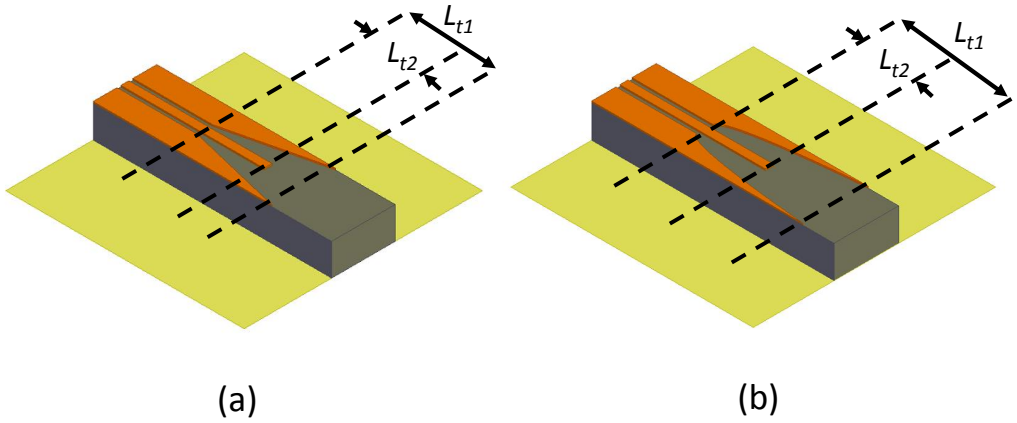


Figure 5.8: 3D model for the proposed CPW to DIG tapered transition with different profiles; (a)Profile 1: Linear, and (b)Profile 2: Quadratic.

ther a test structure with a back-to-back CPW to DIG transition followed by a DIG to

CPW transition or a test structure with a DIG to CPW followed by CPW to DIG. Since the input/ouput interface of the available mmWave measurement equipment is normally waveguide based, a transition from the DWG/DIG to waveguide is needed. This makes the second test structure (DIG to CPW followed by CPW to DIG) a bit longer and more complex to de-embed. In Section 5.4, the details for this type of test structures are provided.

### 5.3.1 Test Structure: Back-to-Back CPW to DIG to CPW transition

As shown in Fig. 5.9, the test structure is a 50Ω CPW line designed on HRS substrate followed by a CPW to DIG transition. Quadratic tapering profile has been used in this test structure. The transition is then followed with a long DIG section (long enough to eliminate direct coupling between the two CPW sections -input and output-). The same CPW line and transition are then used in the reverse order to form the back-to-back test structure. The total length for this test structure is 30mm. Fig. 5.10 shows the simulated S-parameters for a V-band back-to-back test structure with 50Ω CPW interface. The insertion loss at 60GHz is -2.5dB. After de-embedding the DIG loss, the loss of the CPW to DIG transition is calculated to be -0.7dB at 60GHz.

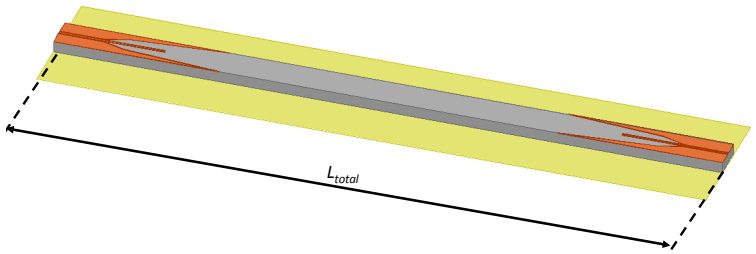


Figure 5.9: 3D model for the proposed back-to-back CPW to DIG test structure.

A similar test structure has been designed to operate in the W-band. The simulated and measured S-parameters are shown in Fig. 5.11. The measured results are in good agreement with the simulated ones. The insertion loss at 80GHz is -4.4dB. After de-embedding the DIG loss, the loss of the CPW to DIG transition is calculated to be -1.6dB at 80GHz.

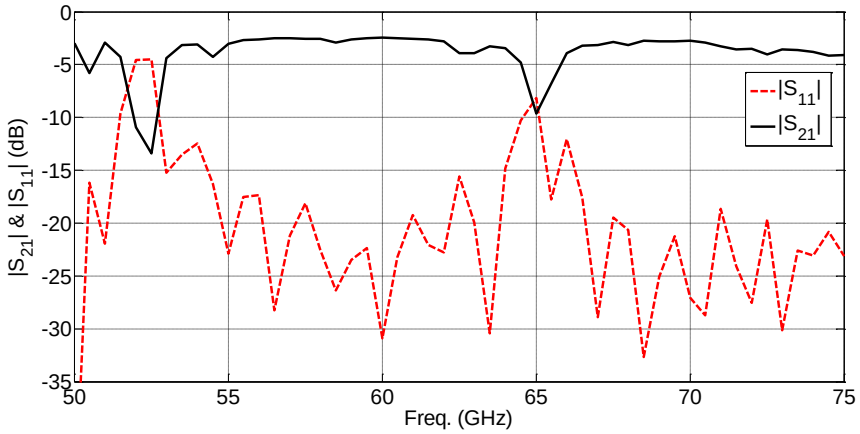


Figure 5.10: Simulated S-parameters for the back-to-back test structure operating at the V-band.

A picture of the fabricated test structure is shown in Fig. 5.12. A two-mask process has been developed and used for the fabrication of the proposed transition. The process consists of standard steps and recipes to achieve both low cost and reproducibility. The process steps can be summarized as shown in Fig. 5.13. Simply, [Step (a)] we clean our high resistivity silicon wafer through RCA1 process before [Step (b)] sputtering 0.5m of Aluminum at each side of the silicon substrate, which is then [Step (c)] coated with a thin photo resist (Shibly 1811 with a thickness of $\sim 1.6\mu m$) on one side of the Aluminum. Then [Step (d)] an optical lithography with a 130mm Chrome mask is performed to make a mask on the wafer for Al etching.

In [Step (e)] the Aluminum is patterned using the wet etching process and the thin photo resist is removed. Meanwhile the back side Aluminum is kept protected with a tape. Then, a mask is prepared for silicon etching. In [Step (f)] a thick photo resist (AZP4620 with a thickness of $\sim 10.3\mu m$) is applied on the top side of the wafer before [Step (g)] performing optical lithography. [Step (h)] Deep Reactive-Ion-Etching (DRIE) (Standard Bosch process) is then performed for the thickness of 500m (a carrier wafer is used during the through wafer etching). Then, [Step (i)] we remove the thick photo resist with acetone.

As shown in Fig. 5.14, the setup used for the measurements is simply a Keysight (formerly Agilent) network analyzer with W-band waveguide extender modules (OML)

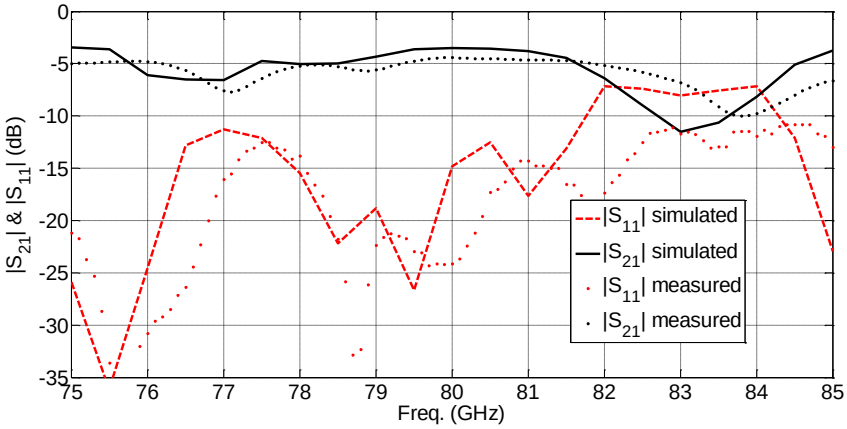


Figure 5.11: Simulated and measured S-parameters for the back-to-back test structure optating at the W-band.

Figure 5.12: Picture of the fabricated back-to-back test structure optating at the W-band.

connected to waveguide GSG probes (Cascade). Cascade 11K probing station has been used. The setup has been calibrated to the probes tips using standard impedance calibration kit. Additionally, different length CPW lines (fabricated on the same HRS substrate) have been used to verify the calibration.

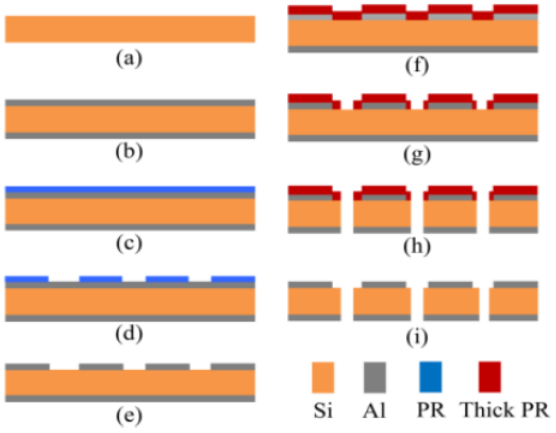


Figure 5.13: Two-mask fabrication process.

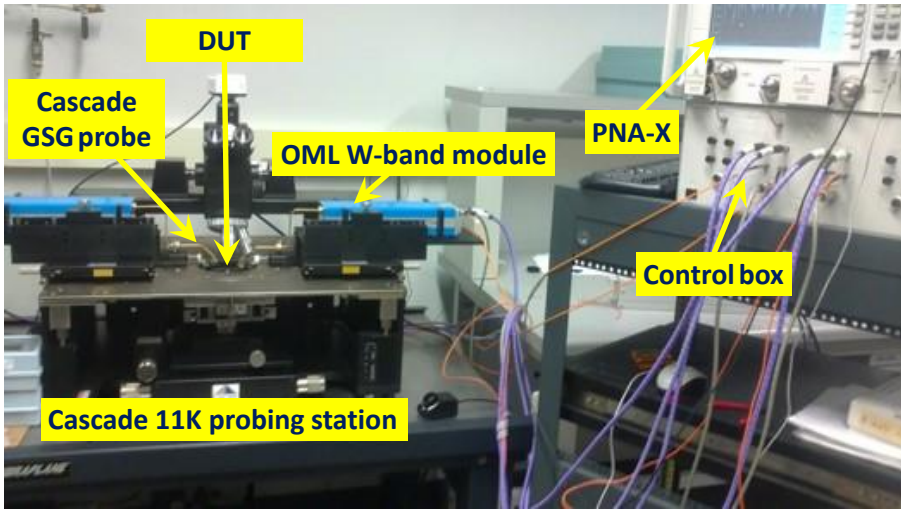


Figure 5.14: On-wafer W-band measurement setup used for testing the back-to-back CPW to DIG transition.

### 5.3.2 Test Structure: CPW-fed Dielectric Side Grating Antenna

We have proposed a CPW-fed dielectric side grating antenna for frequency scanning applications. This antenna can be considered as a test structure to verify the proposed CPW to DIG transition. Dielectric side grating antenna is essentially a travelling wave antenna[3]. The proposed antenna is operating in the V-band. The antenna model is shown in Fig. 5.15. The matching parameters $l_{t1}$ and $l_{t2}$ have been optimized with HFSS and their optimal values are 6.4mm and 5.7mm, respectively.


Figure 5.15: 3D model of the proposed CPW-fed side grating antenna.

The simulated gain versus frequency curve is shown in Fig. 5.16. As can be seen the antenna has a peak gain of 18dBi around 62.5GHz.

The proposed antenna has been fabricated and tested. Fig. 5.17 shows a picture of the proposed antenna fed by a CPW line. A GSG probe connected to a 67GHz network analyzer port is used to excite the antenna. The input matching has been measured and the results are in good match with simulation as shown in Fig. 5.18. As can be seen, the antenna is well matched from 50GHz to 67GHz which makes it ideal for wide band applications.

[3]More details about the proposed CPW-fed dielectric side grating antenna design are available in Section 3.4.

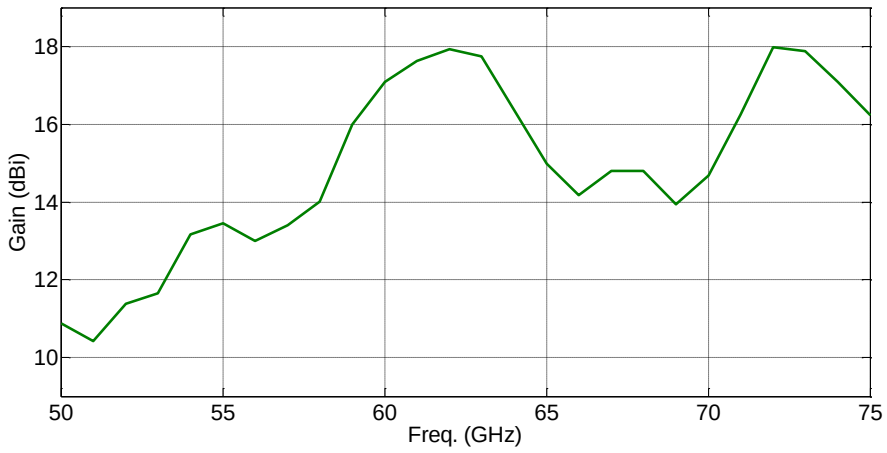


Figure 5.16: The gain frequency response of the proposed antenna.

Figure 5.17: A picture of the proposed CPW-fed side grating antenna.

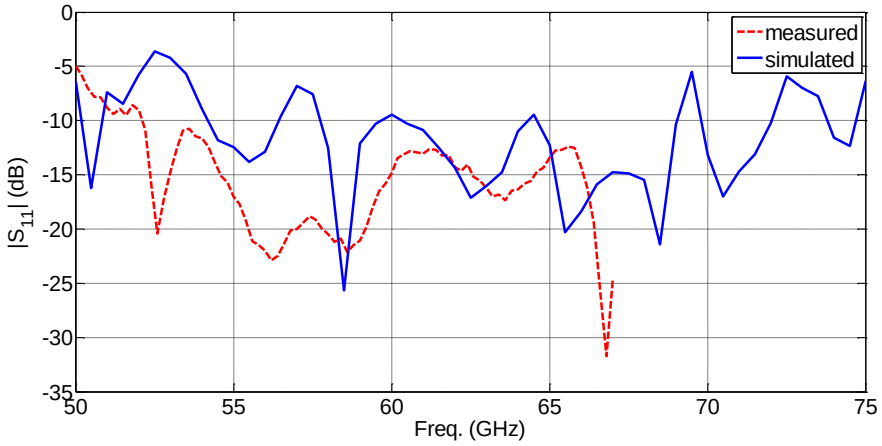


Figure 5.18: Simulated and measured input reflection coefficient of the proposed CPW-fed side grating DIG antenna.

## 5.4 WG to DIG to CPW Transitions (Steps 1 and 2)

As has been mentioned earlier, the input/output interface of the PNA-X is usually waveguide based at the mmWave range. Therefore, a WG to DIG transition is added to our DIG to CPW back-to-back test structure.

### 5.4.1 Test Structure: Back-to-Back transition

This test structure has been fabricated and measured to assess the performance of the proposed transition. A picture of the proposed test structure is shown in Fig. 5.19. The building blocks of both test structures are as follows;

1. A WG to DIG transition (15mm)
2. A DIG section (5mm)
3. A DIG to CPW line transition (8mm)
4. A 50Ω CPW section (4mm)
5. A CPW line to DIG transition (8mm)
6. A DIG section (5mm)
7. A DIG to WG transition (15mm)

The S-parameters results are shown in Fig. 5.20. After de-embedding, the measured loss per CPW to DIG transition is -2 dB.

Figure 5.19: Picture of the proposed test structure.

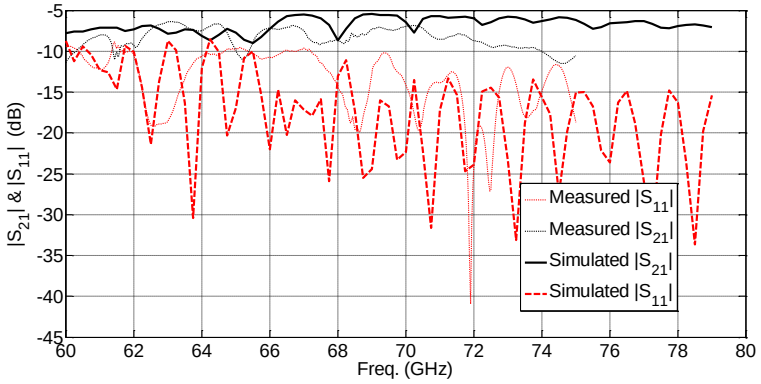


Figure 5.20: Measured and Simulated S-parameters for the proposed test structure.

## 5.5 WG to DIG to CPW to Flip-chip Transitions (Steps 1, 2 and 3)

After having the RF signal delivered to the CPW line, the last step is to carry the signal through the bumps and the RF pads to the on-chip circuit. Although the RF pads (padframe) design is not considered in this study, we will discuss some of the effects and good design practices which affect the transition performance. It is highly desired that the pads are organized in a coaxial like shape as shown in Fig.5.21; however, this arrangement could be practically challenging to achieve due to the on-chip circuit configuration. The pad diameter ($d_{pad}$) is also desired to be minimal to minimize the parasitic capacitance. In our analysis $d_{pad}$ has been chosen to be $80\mu m$.

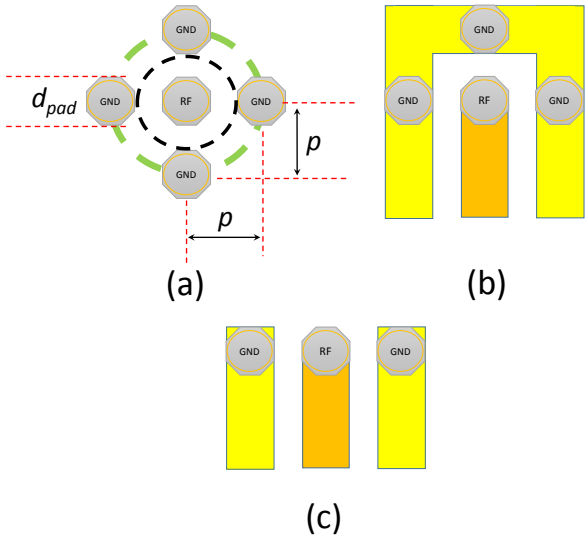


Figure 5.21: Diagram showing different pads assignments.

The pads pitch is critical in two aspects. The first is that if it is too small it can significantly increase the total packaging cost (as it requires advanced technology). This is more critical for substrate/PCB technology; but since we are using thin film/optical lithography technology, the small pads separation is not a significant issue. The second effect of the pads pitch is the bump size, usually the bump size is defined by the pads

diameter and the pads pitch. In our case, the pads pitch ($p$) has chosen to be $200\mu m$. The solder bump has a significant effect on the RF performance at high mmWave frequencies. To illustrate this effect, Fig. 5.22 shows the HFSS model for a dummy chip which has a $50\Omega$ CPW based on HRS substrate. As shown in Fig. 5.23, the solder balls can significantly affect the overall S-parameters of the structure through changing the impedance as well as introducing some radiation loss. Therefore, the transition should be optimized with the solder bumps in place.

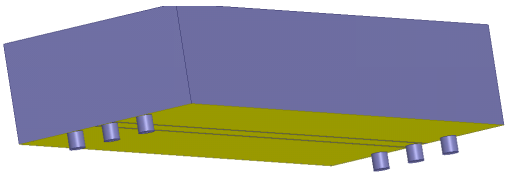

Figure 5.22: 3D model of the flip-chip die with solder bumps.

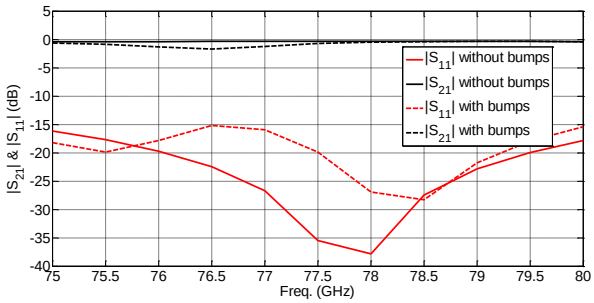


Figure 5.23: 3D model of the flip-chip die with solder bumps.

The DIG flip-chip integration is similar to the test structure proposed in Section 5.4 except for the CPW line, connecting the input section to the output section, which has to be replaced with a transition to the flip-chip die. The CPW ground traces is tapered before the flip-chip to ensure more confined signal and to allow routing other traces on the same layer. In addition, this shape of the ground traces forms a coaxial-like transition which isolates the RF signal from the bias traces and reduces the parallel plate coupling parasitics as this can significantly deteriorate the circuit's functionality (see Fig. 5.24).

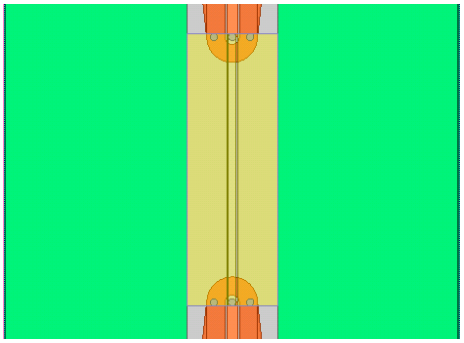

Figure 5.24: CPW to flip-chip transition.

The proposed test structure can be represented by a computational model shown in Fig. 5.25. Typically, the S-parameters model of the active circuit should be cascaded to the transition model while optimizing its performance; however, for simplicity, we have designed a flip-chip circuit with a 50Ω CPW line (dummy flip-chip). This procedure should provide a transition that is well matched for any circuit with a single ended input impedance of 50Ω. Although we have used DIG design here, both the horizontal ($E_x$ modes) and vertical polarizations ($E_y$ modes) can be easily coupled to the CPW line as they have a good projection on the CPW quasi-TEM mode.

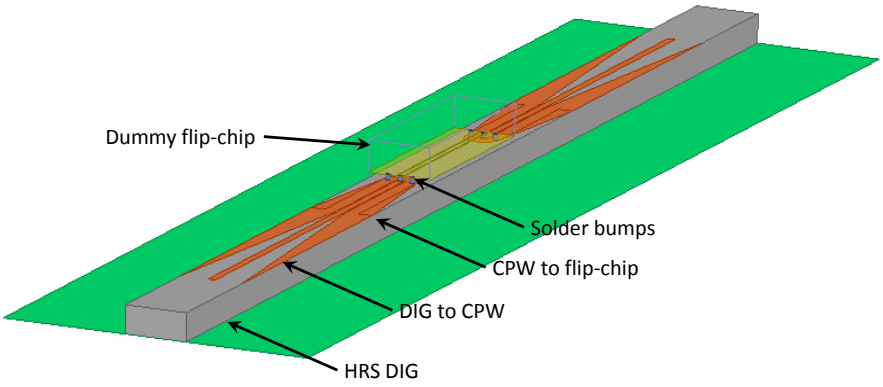


Figure 5.25: HFSS model for the DIG integrated flip-chip.

The transition dimensions have been optimized with the dummy flip-chip and the solder bumps in place. The optimization objective has been to simultaneously minimize the $|S_{11}|$ and maximize the overall $|S_{21}|$. The DIG and the flip-chip are considered fixed for the optimization problem while the rest of the structure geometry parameters have been subjected to optimization. The optimal design dimensions are shown in Fig. 5.26.

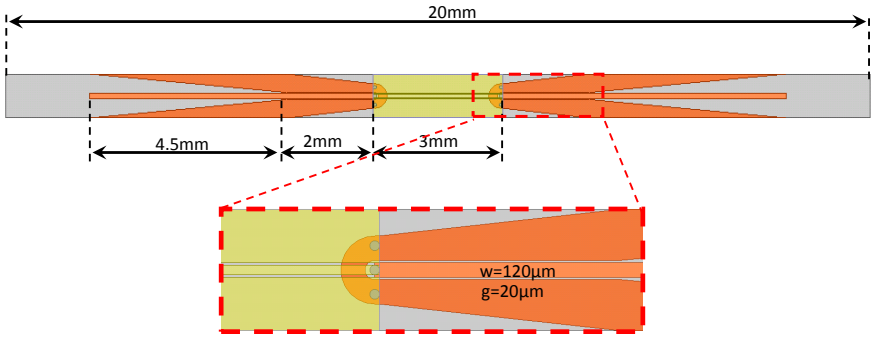


Figure 5.26: Dimensions of the proposed test structure.

Fig. 5.27 shows the E-field distribution across the test structure at 77GHz. The optimal design has the S-parameters shown in Fig. 5.28. The overall loss at 77GHz is $-3.18$dB. After de-embedding the dummy flip-chip loss, the loss per transition (DIG to flip-chip pads) is calculated to be $-1.45$dB.

### 5.5.1 Test Structure: DIG integrated LNA flip-chip with WR10 interface

Another 77GHz test structure at has been designed for a flip-chip amplifier. The new test structure has the same transitions (DIG to CPW and CPW to flip-chip GSG pads) and in addition it has a WR10 to DIG tapered transition (for the sake of testing). The model of this transition is shown in Fig. 5.1. As can be noticed, the LNA has input and output in the south and north directions while the bias pads are arranged in the east and west sides of the die [4]. Therefore, we have routed the DC traces in the middle of the DIG structure

[4]The amplifier has been designed and tested by another member of the group using 60nm CMOS technology [26].

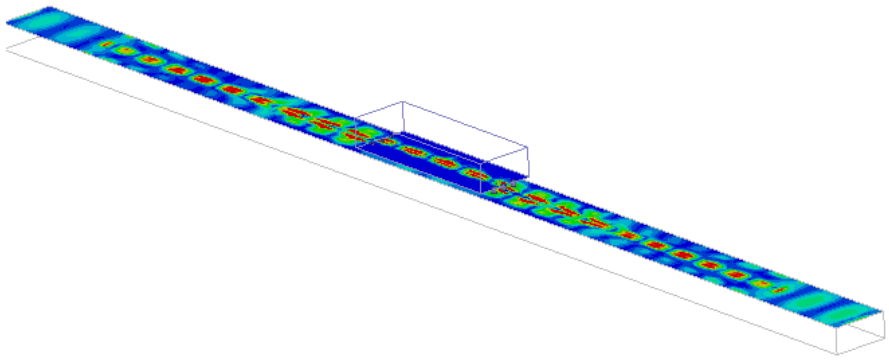

Figure 5.27: Simulated E-field for the DIG integrated flip-chip distribution at 77GHz.

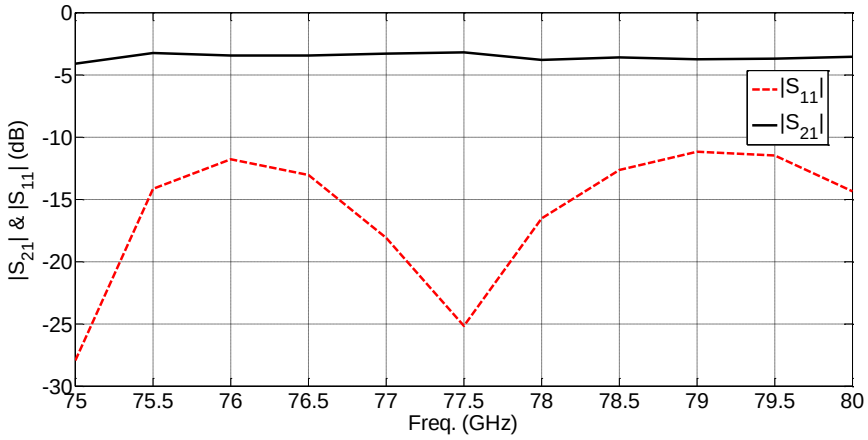


Figure 5.28: Simulated S-parameters for the DIG integrated flip-chip.

normal to the RF path as shown in the model.

The test structure has been designed and fabricated using the same two-mask process. A picture of the proposed test structure is shown in Fig. 5.29. The simulated overall loss per transition is −2.4dB. The overall simulated loss of the test structure is −4.8dB

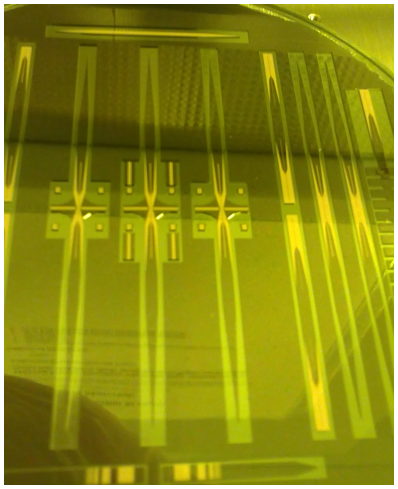

Figure 5.29: Picture of the proposed flip-chip integration structure.

at 77GHz. With a 20dB gain LNA, the expected overall $|S_{21}|$ is expected to be $\sim 15dB$. The structure assembly has been delayed. However, we plan to measure it and report the results as a future work of this thesis.

# Chapter 6

# Conclusion and Future Plan

The development of low cost and high performance mmWave beam-steering solutions drives the future of broadband wireless applications. These applications include, but are not limited to, high resolution automotive radar, imaging, 5G wireless communication, and 60GHz multi-gigabit wireless personal and local area network (WPAN/WLAN). In this work, design procedures and implementation details for novel high efficiency, low cost and easy to integrate mmWave beam-steering solutions have been proposed. In this Chapter, a summary of the topics that are presented. Also, future work and related ideas/designs are discussed.

## 6.1 Summary of Results

This study has introduced a new systematic design approach that uses a simple channel model which we have developed based on ray-tracing approximation to extract antenna and beam-steering related requirements starting from the system level specifications. The two main types of passive beam-steering at mmWave have been covered in this work; namely, the RF beam-switching and phased arrays. New HRS dielectric waveguide technology has been explored for the implementation of the presented high performance passive mmWave beam-steering solutions. The different aspects of the proposed technology have been presented highlighting the ones that make this technology a perfect candidate, compared to other the other existing technologies, for low cost and high performance mmWave applications. Since the cost is so critical to the emerging mmWave applications, various fabrication process considerations and details have been discussed along with the actual

implementations.

Novel passive beam-steering HRS DWG-based components for both beam-switching and phased arrays have been proposed. These components include phased array antenna elements, phase shifters and a switched-beam antenna. The proposed switched-beam antenna is fully made of dielectric and operates at the 77GHz vehicular radar band. The antenna has the advantages of the high efficiency and the ease of integration which are critical at mmWave.

Novel DWG-based antenna element (for phased array configurations) has been presented along with a new approach for designing fully dielectric mm-wave/sub-THz antennas for a given gain pattern specifications. The method has been used to design a 77 GHz high resistivity Silicon antenna. The proposed antenna has a size of 5mmX10mm and a gain of 13dB at 77GHz. The antenna has been fabricated and tested. The measured results are in good agreement with the simulations.

In addition, the thesis presented a new idea for phase shifting based on changing the physical length of the signal path by introducing planar displacements to some free blocks that constitute the dielectric waveguide. A complete design at $77GHz$ has been presented as well. The whole structure is planar and Silicon-based allowing the maximum level of integration. The Genetic Algorithm has been used to optimize the design. The proposed design was able to continuously cover the $360^{\circ}$ phase shifts with the IL ranging from $-2.4dB$ to $-4.4dB$ and a RL better than $-13.5dB$. Moreover, the performance is expected to be scaled up by increasing the number of movable blocks. To speed up the optimization process, a fairly approximate but very fast model based on path fitting and macro-modeling has been developed.

The thesis also presented a low cost and low loss piezoelectric transducer controlled phase shifter for mmWave/sub-THz applications. The proposed idea is based on reducing the propagation constant and modifying the modal distribution of the field in a high resistivity Silicon image guide by a high dielectric constant slab loading. The proposed phase shifter has a measured insertion loss less than -2dB across the range from 87GHz to 94GHz. A phase shift of $85^{o}$ at 90GHz is obtained by a device length of 4mm. The proposed phase shifter has an insertion loss variation less than 0.2dB for $85^{o}$ of phase shift at 90GHz. Measurement results are in good agreement with the simulations. In addition, three different BLT ceramic samples have been tested for the mechanically controlled (manual) version of

the phase shifter. The measured maximum phase shift variation reaches $150^o$ at 100GHz with an average insertion loss of 2.85dB and an insertion loss variation less than 0.7dB for a sample of a 5mm length. The proposed phase shifter has a bandwidth from 95GHz to 105GHz.

Finally, an efficient integration solution has been presented to interconnect the proposed beam-steering antenna systems/components with active components. This includes the development of new wide-band, low loss and low cost transitions.

## 6.2 Future Work

Following is a list of potential research activities can be considered in the future;

### 6.2.1 MEMS-based BLT phase shifter

Although, we have proposed an electrically controlled version of the BLT phase shifter using piezoelectric transducer, an integrated MEMS actuator is preferred from packaging and cost perspectives. A collaboration project with the UW-CIRFE lab is underway to implement a MEMS actuator on BLT. The initial test structures using BLT material have been made and successfully tested.

### 6.2.2 MEMS-based switched-beam antenna

A novel MEMS-based switched-beam antenna has been fabricated and successfully tested within a collaboration project with the UW-CIRFE lab. The antenna is based on Alumina substrate and operating at the Ka-band. The plan is is to extend this project and build a similar structure but using the proposed HRS-based annular grating antenna operating at the W-band.

### 6.2.3 DIG integrated flip-chip

The integration is one of the most critical aspects in mmWave applications. We plan to continue improving the DIG to flip-chip transition characteristics and to verify the simulated data with measured ones.

# References


[1] A. Abdellatif, S. Safavi-Naeini, and M. Mohajer. Novel low cost compact phased array antenna for millimeter-wave 3d beam scanning applications. In *2014 IEEE Antennas and Propagation Society International Symposium (APSURSI)*, pages 1145–1146, July 2014.

[2] A.S. Abdellatif, M. Basha, and S. Safavi-Naeini. Low-cost and high-efficiency multi-beam antenna for millimeter-wave applications. *IEEE Antennas and Wireless Propagation Letters*, 11:141–143, 2012.

[3] A.S. Abdellatif, A.B. El Rouby, M.B. Abdelhalim, and A.H. Khalil. Interconnects parasitic extraction using natural optimization techniques. In *2009 International Conference on Computer Engineering Systems*, pages 218–224, Dec 2009.

[4] A.S. Abdellatif, M. Faraji-Dana, N. Ranjkesh, A. Taeb, M. Fahimnia, S. Gigoyan, and S. Safavi-Naeini. Low loss, wideband, and compact cpw-based phase shifter for millimeter-wave applications. *IEEE Transactions on Microwave Theory and Techniques*, PP(99):1–11, 2014.

[5] A.S. Abdellatif, N. Ghassemi, M. Ghassemi, M. Nezhad-Ahmadi, and S. Safavi-Naeini. Low cost low loss waveguide-fed patch antenna array for automotive radar system. In *2015 Global Symposium On Millimeter-Waves*, May 2015.

[6] A.S. Abdellatif and S. Safavi-Naeini. Novel pixelated high efficiency planar millimeter-wave antennas. In *2012 15th International Symposium on Antenna Technology and Applied Electromagnetics (ANTEM)*, pages 1–2, June 2012.

[7] A.S. Abdellatif and S. Safavi-Naeini. Gpu accelerated channel modeling ray tracing tool. In *2014 IEEE Radio and Wireless Symposium (RWS)*, pages 238–240, Jan 2014.

[8] A.S. Abdellatif, A. Taeb, N. Ranjkesh, Nenasheva E. Gigoyan, S., and S. Safavi-Naeini. Low-insertion loss phase shifter for millimeter-wave phased array antennas. *International Journal of Microwave and Wireless Technologies*, pages 1–7.

[9] A.S. Abdellatif, A. Taeb, N. Ranjkesh, S. Gigoyan, and S. Safavi-Naeini. W-band piezoelectric transducer-controlled low insertion loss variable phase shifter. *Electronics Letters*, 50(21):1537–1538, October 2014.

[10] A.S. Abdellatif, A. Taeb, S. Safavi-Naeini, and K. Schmalz. A terahertz high-efficiency on-chip antenna. In *2014 IEEE Antennas and Propagation Society International Symposium (APSURSI)*, pages 1485–1486, July 2014.

[11] Y. Arai, M. Sato, H.T. Yamada, T. Hamada, K. Nagai, and H. Fujishiro. 60-ghz flip-chip assembled mic design considering chip-substrate effect. *IEEE Transactions on Microwave Theory and Techniques,*, 45(12):2261 –2266, dec 1997.

[12] I. Bahl and K. Gupta. A leaky-wave antenna using an artificial dielectric medium. *IEEE Transactions on Antennas and Propagation,*, 22(1):119 – 122, jan 1974.

[13] Constantine A. Balanis. *Advanced Engineering Electromagnetics*. Wiley, 1989.

[14] A. Basu and T. Itoh. Dielectric waveguide-based leaky-wave antenna at 212 ghz. *IEEE Transactions on Antennas and Propagation*, 46(11):1665–1673, Nov 1998.

[15] Behzad Biglarbegian, Mohamed Basha, Aidin Taeb, Suren Gigoyan, and Safieddin Safavi-Naeini. Silicon-based integrated millimeter-wave cpw-to-dielectric image-guide transition. *International Journal of RF and Microwave Computer-Aided Engineering*, 2014.

[16] A. Bisognin, D. Titz, F. Ferrero, G. Jacquemod, R. Pilard, F. Gianesello, D. Gloria, P. Brachat, C. Laporte, H. Ezzeddine, and C. Luxey. Pcb integration of a vivaldi antenna on ipd technology for 60-ghz communications. *IEEE Antennas and Wireless Propagation Letters*, 13:678–681, 2014.

[17] M. Boers, B. Afshar, I. Vassiliou, S. Sarkar, S.T. Nicolson, E. Adabi, B.G. Perumana, T. Chalvatzis, S. Kavvadias, P. Sen, W.L. Chan, A.H.-T. Yu, A. Parsa, M. Nariman, Seunghwan Yoon, A.G. Besoli, C.A. Kyriazidou, G. Zochios, J.A. Castaneda, T. Sowlati, M. Rofougaran, and A. Rofougaran. A 16tx/16rx 60 ghz 802.11ad chipset with single coaxial interface and polarization diversity. *IEEE Journal of Solid-State Circuits*, 49(12), Dec 2014.

[18] Baolin Cao, Hao Wang, Yong Huang, Jie Wang, and Hanyue Xu. A novel antenna-in-package with ltcc technology for w-band application. *IEEE Antennas and Wireless Propagation Letters*, 13:357–360, 2014.

[19] E. Cohen, M. Ruberto, M. Cohen, O. Degani, S. Ravid, and D. Ritter. A cmos bidirectional 32-element phased-array transceiver at 60 ghz with ltcc antenna. *IEEE Transactions on Microwave Theory and Techniques*, 61(3):1359–1375, March 2013.

[20] R. Collin. Analytical solution for a leaky-wave antenna. *IRE Transactions on Antennas and Propagation,*, 10(5):561 –565, september 1962.

[21] C. Dall'Omo, T. Monediere, B. Jecko, F. Lamour, I. Wolk, and M. Elkael. Design and realization of a $4 \times 4$ microstrip butler matrix without any crossing in millimeter waves. *Microwave and Optical Technology Letters*, 38(6):462–465, 2003.

[22] M. Dorigo, V. Maniezzo, and A. Colorni. Ant system: optimization by a colony of cooperating agents. *IEEE Transactions on Systems, Man, and Cybernetics, Part B: Cybernetics*, 26(1):29 –41, feb 1996.

[23] RS Elliott. Beamwidth and directivity of large scanning arrays. *Microwave Journal*, 7:74–82, 1964.

[24] A. Enayati, G.A.E. Vandenbosch, and W. Deraedt. Millimeter-wave horn-type antenna-in-package solution fabricated in a teflon-based multilayer pcb technology. *IEEE Transactions on Antennas and Propagation*, 61(4):1581–1590, April 2013.

[25] E.G. Erker, A.S. Nagra, Yu Liu, P. Periaswamy, Troy R. Taylor, James Speck, and R.A. York. Monolithic ka-band phase shifter using voltage tunable basrtio3 parallel plate capacitors. *IEEE Microwave and Guided Wave Letters*, 10(1):10–12, Jan 2000.

[26] M. Fahimnia, M. Mohammad-Taheri, Y. Wang, S. Safavi-Naeini, and M. Yu. Optimum millimetre-wave amplifier design using scalable models for circuit elements. *Electronics Letters*, 46(13):928 –930, 24 2010.

[27] M. Fakharzadeh, J. Ahmadi-Shokouh, B. Biglarbegian, M.R. Nezhad-Ahmadi, and S. Safavi-Naeini. The effect of human body on indoor radio wave propagation at 57-64 ghz. In *2009 IEEE Antennas and Propagation Society International Symposium*, pages 1–4, June 2009.

[28] David B. Fogel. Evolutionary algorithms in theory and practice. *Complexity*, 2(4):26–27, 1997.

[29] E.H. Fooks. Propagation in a dielectric-lined circular waveguide. *IEEE Journal on Microwaves, Optics and Acoustics,*, 2(4):117 –122, july 1978.

[30] A.-L. Franc, O.H. Karabey, G. Rehder, E. Pistono, R. Jakoby, and P. Ferrari. Compact and broadband millimeter-wave electrically tunable phase shifter combining slow-wave effect with liquid crystal technology. *IEEE Transactions on Microwave Theory and Techniques*, 61(11):3905–3915, Nov 2013.

[31] S. Franssila. *Introduction to Microfabrication*. Wiley, 2010.

[32] G. Gentile, R. Dekker, P. de Graaf, M. Spirito, L.C.N. de Vreede, and B. Rejaei. Millimeter-wave integrated waveguides on silicon. In *IEEE 11th Topical Meeting on Silicon Monolithic Integrated Circuits in RF Systems (SiRF),*, pages 37 –40, jan. 2011.

[33] Roger F. Harrington. *Time-Harmonic Electromagnetic Fields*. Wiley-IEEE Press, 2011.

[34] J. Hasch, U. Wostradowski, S. Gaier, and T. Hansen. 77 ghz radar transceiver with dual integrated antenna elements. In *2010 German Microwave Conference*, pages 280–283, March 2010.

[35] W. Heinrich. The flip-chip approach for millimeter wave packaging. *IEEE Microwave Magazine*, 6(3):36 – 45, sept. 2005.

[36] W. Heinrich, A. Jentzsch, and G. Baumann. Millimeter-wave characteristics of flip-chip interconnects for multichip modules. *IEEE Transactions on Microwave Theory and Techniques,*, 46(12):2264 –2268, dec 1998.

[37] T. Hirose, K. Makiyama, K. Ono, T.M. Shimura, S. Aoki, Y. Ohashi, S. Yokokawa, and Y. Watanabe. A flip-chip mmic design with coplanar waveguide transmission line in the w-band. *IEEE Transactions on Microwave Theory and Techniques,*, 46(12):2276 –2282, dec 1998.

[38] John H. Holland. *Adaptation in natural and artificial systems: An introductory analysis with applications to biology, control, and artificial intelligence*. Oxford, England: U Michigan Press., 1975.

[39] Changzhou Hua, Xidong Wu, Nan Yang, and Wen Wu. Air-filled parallel-plate cylindrical modified luneberg lens antenna for multiple-beam scanning at millimeter-wave frequencies. *IEEE Transactions on Microwave Theory and Techniques*, 61(1):436–443, Jan 2013.

[40] K. Huang and Z. Wang. *Millimeter Wave Communication Systems*. Wiley-IEEE Press, 2011.

[41] Juo-Jung Hung, L. Dussopt, and G.M. Rebeiz. Distributed 2- and 3-bit w-band mems phase shifters on glass substrates. *IEEE Transactions on Microwave Theory and Techniques*, 52(2):600 – 606, feb. 2004.

[42] S. Jafarlou, M. Bakri-Kassem, M. Fakharzadeh, Z. Sotoodeh, and S. Safavi-Naeini. A wideband cpw-fed planar dielectric tapered antenna with parasitic elements for 60-ghz integrated application. *IEEE Transactions on Antennas and Propagation*, 62(12):6010–6018, Dec 2014.

[43] Cheng Jin, V.N. Sekhar, Xiaoyue Bao, Bangtao Chen, Boyu Zheng, and Rui Li. Antenna-in-package design based on wafer-level packaging with through silicon via technology. *IEEE Transactions on Components, Packaging and Manufacturing Technology*, 3(9):1498–1505, Sept 2013.

[44] Rebecca H. Jordan and Dennis G. Hall. Radiation from an annular grating on a planar optical waveguide. *Applied Physics Letters*, 63(25):3423 –3425, dec 1993.

[45] E. Juntunen, A. Tomkins, A. Poon, J. Pham, A. El-Gabaly, M. Fakharzadeh, H. Tawfik, Yat-Loong To, M. Tazlauanu, B. Lynch, and R. Glibbery. A compact antenna-in-package 60-ghz sige bicmos radio. In *2014 IEEE Radio Frequency Integrated Circuits Symposium*, pages 287–288, June 2014.

[46] Dong Gun Kam, Duixian Liu, A. Natarajan, S. Reynolds, Ho-Chung Chen, and B.A. Floyd. Ltcc packages with embedded phased-array antennas for 60 ghz communications. *IEEE Microwave and Wireless Components Letters*, 21(3):142–144, March 2011.

[47] Dong Gun Kam, Duixian Liu, A. Natarajan, S.K. Reynolds, and B.A. Floyd. Organic packages with embedded phased-array antennas for 60-ghz wireless chipsets. *IEEE Transactions on Components, Packaging and Manufacturing Technology*, 1(11):1806–1814, Nov 2011.

[48] J. Kennedy and R. Eberhart. Particle swarm optimization. In *1995 IEEE International Conference on Neural Networks*, volume 4, pages 1942 –1948 vol.4, nov/dec 1995.

[49] N. Kingsley, P. Kirby, G. Ponchak, and J. Papapolymerou. 14 ghz mems 4-bit phase shifter on silicon. In *2004 Topical Meeting on Silicon Monolithic Integrated Circuits in RF Systems*, pages 326 – 328, sept. 2004.

[50] S. Kirkpatrick, C. D. Gelatt, and M. P. Vecchi. Optimization by simulated annealing. *Science*, 220(4598):671–680, 1983.

[51] R.M. Knox. Dielectric waveguide microwave integrated circuits - an overview. *IEEE Transactions on Microwave Theory and Techniques*, 24(11):806–814, Nov 1976.

[52] S. K. Koul and B. Bhat. *Microwave and millimeter wave phase shifters : dielectric and ferrite phase shifters*. Artech House, 1991.

[53] Woosung Lee, Jaeheung Kim, and Young Joong Yoon. Compact two-layer rotman lens-fed microstrip antenna array at 24 ghz. *IEEE Transactions on Antennas and Propagation,*, 59(2):460 –466, feb. 2011.

[54] D. Lioubtchenko, S. Tretyakov, and S. Dudorov. *Millimeter-Wave Waveguides*. Kluwer Academic Publishers, 2003.

[55] D. Liu, U. Pfeiffer, and J. Grzyb. *Advanced millimeter-wave technologies: antennas, packaging and circuits*. J. Wiley & Sons, 2009.

[56] Junwen Liu, Qing-An Huang, Jintang Shang, Jing Song, and Jieying Tang. Micromachining of pyrex7740 glass and their applications to wafer-level hermetic packaging of mems devices. In *IEEE 23rd International Conference on Micro Electro Mechanical Systems (MEMS),*, pages 496 –499, jan. 2010.

[57] A. Maltsev, E. Perahia, R. Maslennikov, A. Sevastyanov, A. Lomayev, and A. Khoryaev. Impact of polarization characteristics on 60-ghz indoor radio communication systems. *IEEE Antennas and Wireless Propagation Letters*, 9:413–416, 2010.

[58] E A J Marcatili. Dielectric rectangular waveguide and directional coupler for integrated optics. *Bell Systems Technical Journal*, 48(21):2071–2102, 1969.

[59] F. Marty, L. Rousseau, B. Saadany, B. Mercier, O. Franais, Y. Mita, and T. Bourouina. Advanced etching of silicon based on deep reactive ion etching for silicon high aspect ratio microstructures and three-dimensional micro- and nanostructures. *Microelectronics Journal*, 36(7):673 – 677, 2005. European Micro and Nano Systems - EMN 2004.

[60] Frédéric Marty, Lionel Rousseau, Bassam Saadany, Bruno Mercier, Olivier Français, Yoshio Mita, and Tarik Bourouina. Advanced etching of silicon based on deep reactive ion etching for silicon high aspect ratio microstructures and three-dimensional micro- and nanostructures. *Microelectronics journal*, 36(7):673–677, 2005.

[61] Melanie Mitchell. *An introduction to genetic algorithms*. MIT Press, 1998.

[62] M. Mohajer, Safieddin Safavi-Naeini, and S.K. Chaudhuri. Performance limitations of planar antennas. In *2010 IEEE Antennas and Propagation Society International Symposium (APSURSI)*, pages 1–4, July 2010.

[63] EA Nenasheva and NF Kartenko. High dielectric constant microwave ceramics. *Journal of the European Ceramic Society*, 21(15):2697–2701, 2001.

[64] M.-R. Nezhad-Ahmadi, M. Fakharzadeh, B. Biglarbegian, and Safieddin Safavi-Naeini. High-efficiency on-chip dielectric resonator antenna for mm-wave transceivers. *IEEE Transactions on Antennas and Propagation*, 58(10):3388–3392, Oct 2010.

[65] R.O. Ouedraogo, E.J. Rothwell, and B.J. Greetis. A reconfigurable microstrip leaky-wave antenna with a broadly steerable beam. *IEEE Transactions on Antennas and Propagation,*, 59(8):3080 –3083, aug. 2011.

[66] A. Patrovsky and Ke Wu. Substrate integrated image guide (siig)-a planar dielectric waveguide technology for millimeter-wave applications. *IEEE Transactions on Microwave Theory and Techniques*, 54(6):2872–2879, June 2006.

[67] David M. Pozar. *Microwave Engineering*. Wiley, 2004.

[68] C.T. Rodenbeck, Ming-Yi Li, and Kai Chang. A novel millimeter-wave beam-steering technique using a dielectric-image line-fed grating film. *IEEE Transactions on Antennas and Propagation,*, 51(9):2203 – 2209, sep 2003.

[69] P. Romano, O. Araromi, S. Rosset, H. Shea, and J. Perruisseau-Carrier. Tunable millimeter-wave phase shifter based on dielectric elastomer actuation. *Applied Physics Letters*, 104(2):024104–024104–5, Jan 2014.

[70] W. Rotman and R. Turner. Wide-angle microwave lens for line source applications. *IEEE Transactions on Antennas and Propagation*, 11(6):623 – 632, nov 1963.

[71] Woorim Shin, O. Inac, Yu-Chin Ou, Bonhyun Ku, and G.M. Rebeiz. A 108−112 ghz 4x4 wafer-scale phased array transmitter with high-efficiency on-chip antennas. In *2012 IEEE Radio Frequency Integrated Circuits Symposium (RFIC)*, pages 199–202, June 2012.

[72] Woorim Shin, Bon-Hyun Ku, O. Inac, Yu-Chin Ou, and G.M. Rebeiz. A 108-114 ghz 4 ×4 wafer-scale phased array transmitter with high-efficiency on-chip antennas. *IEEE Journal of Solid-State Circuits*, 48(9):2041–2055, Sept 2013.

[73] N. Somjit, G. Stemme, and J. Oberhammer. Deep-reactive-ion-etched wafer-scale-transferred all-silicon dielectric-block millimeter-wave mems phase shifters. *Journal of Microelectromechanical Systems*, 19(1):120 –128, feb. 2010.

[74] In Sang Song, Jaeheung Kim, Dong Yun Jung, Ki Chan Eun, Jae Jin Lee, Seong Jun Cho, Hong Yi Kim, Jai-Hoon Bang, Inn-Yeal Oh, and Chul-Soon Park. 60ghz rotman lens and new compact low loss delay line using ltcc technology. In *2009 IEEE Radio and Wireless Symposium*, pages 663–666, Jan 2009.

[75] Qi Song, Salvatore Campione, Ozdal Boyraz, and Filippo Capolino. Silicon-based optical leaky wave antenna with narrow beam radiation. *Opt. Express*, 19(9):8735–8749, Apr 2011.

[76] A. Stehle, G. Georgiev, V. Ziegler, B. Schoenlinner, U. Prechtel, H. Seidel, and U. Schmid. Rf-mems switch and phase shifter optimized for w-band. In *2008 European Microwave Conference*, pages 104–107, Oct 2008.

[77] A. Taeb, A.S. Abdellatif, G.Z. Rafi, S. Gigoyan, S. Safavi-Neini, and M. Basha. A low-cost silicon-based beam-steering grating antenna for g-band applications. In *2014 IEEE Antennas and Propagation Society International Symposium (APSURSI)*, pages 1282–1283, July 2014.

[78] T. Tajima, Ho-Jin Song, K. Ajito, M. Yaita, and N. Kukutsu. 300-ghz step-profiled corrugated horn antennas integrated in ltcc. *IEEE Transactions on Antennas and Propagation*, 62(11):5437–5444, Nov 2014.

[79] Y.M. Tao and G.Y. Delisle. Lens-fed multiple beam array for millimeter wave indoor communications. In *1997 IEEE Antennas and Propagation Society International Symposium*, volume 4, pages 2206 –2209 vol.4, jul 1997.

[80] D. Titz, R. Pilard, F. Ferrero, F. Gianesello, D. Gloria, C. Luxey, P. Brachat, and G. Jacquemod. 60ghz antenna integrated on high resistivity silicon technologies targeting whdmi applications. In *2011 IEEE Radio Frequency Integrated Circuits Symposium (RFIC)*, pages 1–4, June 2011.

[81] Y. Tokumitsu, M. Ishizaki, M. Iwakuni, and T. Saito. 50-ghz ic components using alumina substrates. *IEEE Transactions on Microwave Theory and Techniques*, 31(2):121 –128, feb. 1983.

[82] Robert E. Webster. Radiation patterns of a spherical luneberg lens with simple feeds. *IRE Transactions on Antennas and Propagation*, 6(3):301–302, July 1958.

[83] Jing Wu, Jing Lou, Ming Li, Guomin Yang, Xi Yang, J. Adams, and Nian X. Sun. Compact, low-loss, wideband, and high-power handling phase shifters with piezoelectric transducer-controlled metallic perturber. *IEEE Transactions on Microwave Theory and Techniques*, 60(6):1587–1594, June 2012.

[84] Hao Xu, V. Kukshya, and T.S. Rappaport. Spatial and temporal characteristics of 60-ghz indoor channels. *IEEE Journal on Selected Areas in Communications*, 20(3):620–630, Apr 2002.

[85] Junfeng Xu, Zhi Ning Chen, Xianming Qing, and Wei Hong. Bandwidth enhancement for a 60 ghz substrate integrated waveguide fed cavity array antenna on ltcc. *IEEE Transactions on Antennas and Propagation*, 59(3):826–832, March 2011.

[86] Junfeng Xu, Zhi Ning Chen, Xianming Qing, and Wei Hong. 140-ghz siw ltcc antenna array using a large via-fenced and slotted dielectric loading. In *2013 7th European Conference on Antennas and Propagation (EuCAP)*, pages 2861–2864, April 2013.

[87] Ming yi Li and Kai Chang. New tunable phase shifters using perturbed dielectric image lines. *IEEE Transactions on Microwave Theory and Techniques*, 46(9):1314–1317, Sep 1998.

[88] T. Yoneyama and Shigeo Nishida. Nonradiative dielectric waveguide for millimeter-wave integrated circuits. *IEEE Transactions on Microwave Theory and Techniques*, 29(11):1188–1192, Nov 1981.

[89] A. Zandieh, A.S. Abdellatif, A. Taeb, and S. Safavi-Naeini. Low-cost and high-efficiency antenna for millimeter-wave frequency-scanning applications. *IEEE Antennas and Wireless Propagation Letters*, 12:116–119, 2013.

[90] J. Zhang, W. Wu, and D.-G. Fang. 360 scanning multi-beam antenna based on homogeneous ellipsoidal lens fed by circular array. *Electronics Letters*, 47(5):298 –300, 3 2011.